IntechOpen

# Additive Manufacturing of High-performance Metals and Alloys

## Modeling and Optimization

*Edited by Igor V. Shishkovsky*

# ADDITIVE MANUFACTURING OF HIGH-PERFORMANCE METALS AND ALLOYS - MODELING AND OPTIMIZATION

Edited by **Igor V. Shishkovsky**

**Additive Manufacturing of High-performance Metals and Alloys - Modeling and Optimization**
http://dx.doi.org/10.5772/intechopen.69421
Edited by Igor V. Shishkovsky

**Contributors**

Wan Sharuzi Wan Harun, Nurul Kamariah Md Saiful Islam, Dayangku Noorfazidah Awang Shri, Saiful Anwar Che Ghani, Mohd Yuhyi Mohd Tadza, Ahmad Tarmizi Ahmad Haron, Jingwei Zhang, Lei Yan, Frank Liou, Wei Li, Klimova-Korsmik, Saniya LeBlanc, Haidong Zhang, Igor Shishkovsky, Pavel Kuznetcov, Artem Deev, Vitaliy Bobyr, Anton Zhukov, Mikhail Staritcyn, Dmitriy Trushnikov, Oleg Smetannikov, Anatoly Perminov, Shengyong Pang, Karuppasamy Poolan Karunakaran, Petr Maksimov, Mariia Bartolomey, Aleksei Kovyazin, Vladimir Belenkiy, Yurii Schitsyn



**Notice**



First published in London, United Kingdom, 2018 by IntechOpen
eBook (PDF) Published by IntechOpen, 2019
IntechOpen is the global imprint of INTECHOPEN LIMITED, registered in England and Wales, registration number: 11086078, The Shard, 25th floor, 32 London Bridge Street
London, SE19SG – United Kingdom
Printed in Croatia

British Library Cataloguing-in-Publication Data
A catalogue record for this book is available from the British Library

Additional hard and PDF copies can be obtained from orders@intechopen.com

Additive Manufacturing of High-performance Metals and Alloys - Modeling and Optimization
Edited by Igor V. Shishkovsky

p. cm.

Print ISBN 978-1-78923-388-9

Online ISBN 978-1-78923-389-6

eBook (PDF) ISBN 978-1-83881-390-1

# Meet the editor

Igor V. Shishkovsky, PhD and Doctor of Sciences, is a leading researcher at the PN Lebedev Physical Institute (LPI) of Russian Academy of Sciences (RAS). His teaching career started at the Samara State Technical University, where he went way from lecturer to professor and specialized in laser technologies and first developed rapid prototyping in Russian Federation (RF). In the middle of 2000, he was an invited professor at the Diagnostics and Imaging of Industrial Processes Laboratory, Ecole Nationale d'Ingenieurs de Saint Etienne, France. He was the one from the science leaders of Mega-Grant Laboratories by additive technologies, which were organized under the initiative of Department of Education and Science of RF at the Moscow State University of Technologies named STANKIN and Kazan State Technical University. He received Samara Region Administration Award twice and nominated for his diploma from LPI (Moscow) for the studies in powder bed fusion technology. He is a fellow of SPIE, an expert of international and domestic science foundations, and a certified expert of RAS.

# Contents

# Preface

Freedoms in material choice based on combinatorial design, different directions of process optimization, and computational tools are a significant advantage of additive manufacturing technology. The combination of additive and information technologies enables rapid prototyping and rapid manufacturing models on the design stage, thereby significantly accelerating the design cycle in mechanical engineering. Modern and high-demand powder bed fusion and directed energy deposition methods allow obtaining functional complex shapes and functionally graded structures. Specificity of the thermal cycle with a high-cooling rate under laser influence on powder materials is favorable for the creation of strengthened materials, potentially having improved mechanical properties. Unfortunately, this advantage is not always realized due to the residual porosity, partial delamination, cracking, uneven distribution of strengthening phases, and other possible defects.Until now, the experimental parametric analysis remains as the main method during AM optimization. Small spatial and temporal scales of the processes do not allow analyzing in detail how the separate powder particles are transformed into a solid state. Due to limited experimental data, which are often a mix of physical processes that cannot be examined separately, it is not always possible to assess trends properly and achieve optimal results quickly. Numerical modeling is able to recover the missing data from the experiment and give additional assessments that are required for optimization. An additional goal of this book is to introduce readers to new modeling and material's optimization approaches in the rapidly changing world of additive manufacturing of high-performance metals and alloys.

The book is outlined in six chapters. The introductory chapter is to designate for the readers of this monograph the vector of development of two important approaches—the material genome initiative and the methodology for rapid alloy prototyping (i.e., accelerated development and testing of new alloys) based on the combination of additive manufacturing technologies and methods of combinatorial design.

Chapter 1 devotes to a very interesting predictive multiscale model based on a cellular automaton—finite element method has been developed to simulate thermal history and microstructure evolution during metal solidification for direct metal deposition process. Chapter 2 introduces the readers to thermomechanical simulations of the process of 3D additive plasma deposition of wire materials. Chapter 3 presents the theory and technology optimization for manufacturing large-sized products, which is the additive technology of high-speed direct laser deposition. Chapter 4 covers the parameter-property relation during selective laser sintering or melting of promising oxide ceramics. Chapter 5 discusses the powder bed fusion optimization for proper item placement, structure, and properties of the bulk standard samples, including cellular energy absorbers.

I appreciate the contributions of all the authors and IntechOpen publishing managers and thank them for their great efforts and constructive discussions that helped to bring this edited manuscript to a successful completion.

**Prof. Igor V. Shishkovsky**
Leading Researcher
Laboratory of Laser Technologies
P.N. Lebedev Physical Institute of Russian Academy of Sciences
Samara Branch
Russian Federation

Chapter 1

# Introductory Chapter: Genome of Material for Combinatorial Design and Prototyping of Alloys

Igor Shishkovsky

Additional information is available at the end of the chapter

http://dx.doi.org/10.5772/intechopen.77360

## 1. Material genome: New paradigm of additive manufacturing

Materials present an integral part of the additive technology (AT). The key task in creation and processing of new materials for the AT is to expand the range of such materials (including through mixing/alloying/modeling of composites), to improve their quality, to increase the additive process stability, reproducibility and reliability, including by using multimaterial powdered systems, while maintaining a low cost of materials, the process of their manufacturing and pre- and/or post-processing.

However, the development of the AT components (i.e., technologies and equipment for the powdered material manufacturing, 3D part synthesis and subsequent post-processing) without a concurrent improvement of the accompanying directions does not allow obtaining the maximum effect. The conventional cycle of the development of new materials for the additive manufacturing (AM) transition needs a revision.

In 2011, the administration of President Obama presented two breakthrough initiatives, "*MGI—Material Genome Initiative for Global Competitiveness*" and "*AMP—Advanced Manufacturing Partnership*," prepared by the USA National Council for Science and Technology [1, 2]. In the AT literature, the second initiative is mostly mentioned. Indeed, the AMP allowed the launch of a number of projects in the USA: America Makes—National Additive Manufacturing Innovation Institute (NAMII); Lightweight and Modern Metals Manufacturing Innovation (LM3I) Institute; Digital Manufacturing and Design Innovation (DMDI) Institute [3–5]. Nevertheless, the MGI initiative is no less significant. In fact, it is a set of tools that implement the iterative concept of the new material development, which allows reducing of the resource intensity (time and cost) of the material science cycle by 50% [1]. The essence of the concept consists of a continuous exchange of information at different stages of the development of

new materials, not only within a single subject area (e.g., structural or functional materials), but for all the types of materials (**Figure 1**).

Along with the "America Makes" additive community [3], a self-regulating society has been formed in the United States that consolidates scientists engaged in the development and commercialization of new materials based on the MGI concept [1]. The accumulation of information (Big Data (BD)), presentation of tools for their use and creation of other tools provide a transition from quantity to quality. The principles of open architecture provide the concentration of new ideas in the MGI community. The use of block-chain technologies [6] allows ensuring of the MGI implementation under the BD using, provides the data management, guarantees their reliability and significantly improves quality due to the internal certification of future 3D AM parts.

The traditional cycle of the new material fabrication includes the following stages: (1) development of the material composition; (2) optimization of the material properties; (3) design of products from the material, including manufacturing techniques; (4) testing and certification of the material; (5) commercialization of the material.

The iterative cycle proposed within the framework of the MGI concept allows to combine separate stages in different directions so that to accelerate the achievement of the results (see **Figure 1**). In particular, the information about materials, about the AM processes and optimal regimes for the 3D parts fabrication is subject to association. On the other hand, the spatial and temporal scalability of modern methods of computational materials science should be combined with the experimental results under the searching of optimal AM regimes, that is, should find the experimental confirmation.

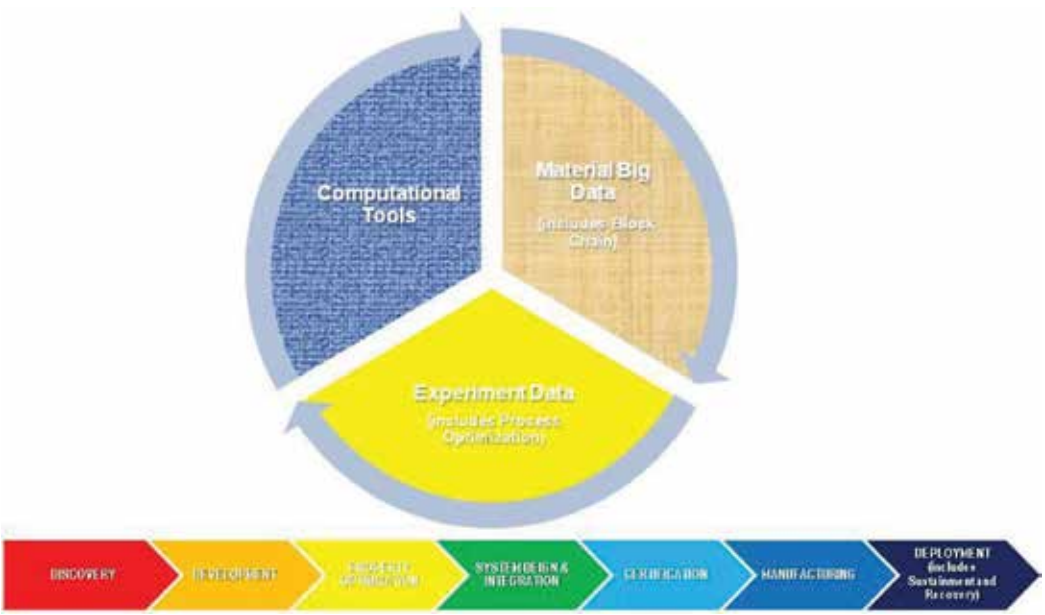


**Figure 1.** Additive manufacturing via material genome route.

http://dx.doi.org/10.5772/intechopen.77360

The MGI concept emergence became possible due to the advanced achievements in the information technologies (IT) over the past 10 years, namely, due to the cost reduction of the information transmission and storage, increase of the speed of transmission and processing of the information. Priority MGI trends in the AM applications are

- optimization of the development technologies for the complex high-dimensional phase spaces;
- effective methods for the experimental data analysis in order to determine the relationship between properties of different levels (e.g., between microstructure, chemical composition, processing and volume properties);
- fundamental properties of the materials behavior;
- tools for experimental data analyzing and the relationship between the experimental data and predictive modeling;
- revision of theories, modification and updating of the developed models and methods, realization of new experiments, caused by the discrepancy between the theory and new experimental data and modeling.

The MGI approaches erase boundaries between a wide range of materials both in the areas where numerical methods are already in use—structural materials, including composites, and also in the areas where they are still weakly used, for instance for soft materials (oligomers, polymers, 3D inks-jet, powders, wires, etc.).

The essence of the approaches used in MGI can be understood on the basis of the MGI Principal Investigator Meeting projects of the first and second wave conducted in the USA in 2015–2016 [7, 8].

## 2. MGI in high-performance metals and alloys

The MGI approaches are actively applied both in the development of structural materials and for manufacturing technologies. Depending on the property being modeled, object and process, the following levels are distinguished: atomic, micro, meso- and macrolevels, and the conditional size ranges are <A-nm, nm-μm, μm-mm, >mm, respectively. For each level, certain modeling methods are characteristic.

Atomic modeling is widely used in developing new materials and predicting their features. Here, the numerical molecular dynamics models as well as the density functional theory are used.

At the micro level, the data on the phase stability are determined as the input data for thermodynamic models used to calculate the phase diagrams and crystallization points.

The problems solved by meso-level modeling lie on the border of micro- and macrolevels. There is practically no commercial software for meso-level modeling, still a large number

of user subprograms have been developed that extend the resource of standard computing packages. For this, the computational methods are used such as the phase field model, discrete dislocation dynamics, physical plasticity theory, and so on.

At the macrolevel, the problems of mechanics of continua are solved by using the finite elements methods (FEM) and finite differences method (FDM). Recently, an actively developed approach is that involving the creation of structural and multi-physical models based on the FEM [9].

It is obvious that the possibilities for the MGI use should most clearly reveal themselves in the AT, since in fact these technologies are digital manufacturing. The technologies of direct and layerwise laser additive manufacturing (LAM) make it possible to obtain products with directional anisotropy due to their ability to control the laser beam trajectory during fusion and to determine technological parameters such as laser beam diameter, linear energy density and scanning geometry. The 3D part fabrication with the areas differing by their characteristics depending on the local loading conditions becomes possible through the use of technologies of a direct laser deposition (DLD). The ability to design the topology of the macrostructure of the synthesized material is one of the main advantages of the AT in the framework of the concept for generating of smart materials. At the same time, the fused particles arrangement and their size are largely stochastic, thus leading to the material structural heterogeneity and the emergence of defects in the form of residual porosity. In addition, despite the application of the technique of the repeated remelting of the surface layer, the resulting roughness does not meet the engineering requirements. In this connection, there exist the following widespread post-processing methods for the synthesized parts that are divided into two types of technologies—volume effect technologies (hot isostatic pressing (HIP) and surface effect technologies)—that include finishing mechanical (or abrasive) treatment, electrophysical and electrochemical techniques, methods for surface layer modification. A particular attention should be paid here to the methods for predicting of the finished parts properties, taking into account their heterogeneity, as well as to the methods for correction of these properties, for example, by modifying the surface layer of products.

The development and use of the MGI methods in the AT design will improve the predicting accuracy of the material properties and of the surface layer of the parts after modification. The influence on the texture and structure will allow to form the properties of finished parts, not only in the obvious area of the surface layer microhardness increase, but also in providing an enhanced corrosion and erosion resistance; and crack resistance owing to the formation of compression stresses.

The Material Genome Initiative (MGI) offers a paradigm that perfectly matches the AM needs. The MGI is built on the base of the search of specific materials that ensure the generation of different final properties via using different processes. It connects multiple scales, from quantum and atomistic to molecular mechanics and derived potentials, mesoscale (nanometer) methods and, finally, continuum methods. The characteristics and effects of the process play an integral role in the material genome (MG). A similar approach for combining the scales and methods is suitable for the AM. In the AM, the material microstructure can be adapted to the specific requirements and needs, thus providing wide possibilities for the material design.

For AT, the problems of certification and safety of the used powder materials and the received 3D products are especially relevant, since these products can work in the important mechanisms of perspective modern cars, aircrafts or missiles. Therefore, the developed approaches for the selection and storage of the data on materials and/or processes are of an extreme necessity. The monitoring of the storage conditions of all the data, codes, and discussions with graphically attached persistent identifiers, along with the low maintenance costs, is fundamental to the continuous and efficient complex operation of the whole platform.

The digital recording of code and data transformations that occur among users of the platform during their cooperative work provides new rich opportunities capable of improving the integration and operational process in all directions (including research, education, authentic knowledge transfer, manufacturing and product life cycle).

## 3. Combinatorial design of alloys for AM

A wide range of the AM materials and processes requires extensive researches and determination of the "process-structure-properties" relationships. For fabrication of unique structures that do not exist in nature or reproduce its best manifestations (e.g., the parts with a negative coefficient of thermal expansion or optical transmission), of metamaterials, biomimetic structures and surfaces, the problems of using the unique AT resource are of no less interest. Besides, one should also realize the AT applicability for the manufacturing of materials with multilevel hierarchical functionality on nano-, micro- and mesoscales, up to the development of the 3D-printing tools for fabrication of atom-by-atom structures and construction of additive nanofabricators [10].

The 3D combinatorial metallurgical method, called a "*Rapid Alloy Prototyping"* (*RAP*), has been recently proposed by Prof. D. Raabe with coworkers [11] and showed a successful testing on Twinning-Induced Plasticity (TWIP) steels with reduced density [12, 13], high-entropy alloys [14–16], intermetallic alloys [17, 18], high-strength martensitic [19, 20] and high-modulus steels [21]. It includes semicontinuous high-performance fabrication of the 3D parts, their heat treatment, preparation to testing, allowing to synthesize and test up to 45 material parameters within 35 h [11].

The ideas of the LAM use for fabrication of both functional and gradient alloys (FG) have been discussed for a long time [22–24]. However, in the combinatorial design of alloys by the RAP method, the LAM use provides a number of additional advantages.

First, a specific thermal regime is realized throughout the metallurgical process [25, 26]: the temperature-time profile for the samples obtained by LAM methods is rather different from those observed in a typical metallurgical manufacturing. Under layer-by-layer (3D) laser cladding, the powder material is quenched after the melting and crystallized at high speeds due to a rapid heat removal to the substrate. With the overlay of each following layer during the subsequent layers cladding, the consolidated material is repeatedly heated and even melted partially by a laser beam [25, 26]. This means that the materials produced by the LAM are subjected to a series of consecutive short-pulse temperature cycles of a decreasing intensity [25, 27]. Such cyclic heat treatment can also be used for controlling of solid-phase transformations in

the material after the cladding. This is favorable for structural steels and super-alloys where the strength, toughness and hardness are ensured by the dispersion hardening also [17].

The second advantage of the LAM use for combinatorial development of high-performance alloys is that a rapid melting and solidification occur locally, within a small volume [25, 26]. This allows working with the materials that are not melting or hardly melting in an ingot, for example, oxide-strengthened alloys, or materials containing components in the amount exceeding the solubility limit in the solid solution. Typical cooling rates for the LAM are from $10^3$ to $10^6$ K/s [25, 26]. These high cooling speeds lead to a rapid solidification of the melt, creation of a finely dispersed structure that increases plasticity, in contrast to the coarse-grained cast structure obtained by a continuous casting [25, 27]. This proves that the LAM can serve not only as an instrument for combinatorial alloy modeling, but also ensures a qualitative expansion of options for the additive manufacturing (AM).

Third, some LAM methods are "self-adapted" for the RAP, that is, they quickly outline suitable series of applicable compositions, which is explained by the peculiarities of powder metallurgy as a production process [10, 25, 26].

For the RAP purposes, from the whole scope of the AT variety, layer-by-layer selective laser melting (SLM) or laser metal deposition (LMD) techniques can be recommended [28]. The latter is sometimes also referred to as 3D-laser-cladding (or direct metal deposition—DMD) & Laser Engineered Net Shaping (LENS). Thus, all the above said characterizes the LAM as a highly effective technology for the fast study and development of new alloys and the 3D part manufacturing on their basis.

## 4. Conclusion

The aim of this introductory chapter is to designate for the readers of this monograph the vector of development of these two approaches—the MGI and the newest methodology for rapid alloy prototyping (i.e., accelerated development and testing of new alloys) based on the combination of LAM technologies and methods of combinatorial design. The presentation pursued three goals:

- the first goal was to represent the efficiency of the combination of these two approaches for accelerated manufacturing (i.e., RAP) and study of the alloy versions;
- the second goal was to determine the compositions of the selected composite alloys, providing improved properties in comparison with the existing analogues;
- the third goal was to determine and demonstrate the possibility (in-situ, i.e., on-site) of obtaining metal parts with a pre-specified heterogeneity of microstructure and properties.

The last goal is the most significant for high-performance structural alloys, since the products made of them often must combine a high hardness of the surface layer with a softer and viscous core. The LAM is obviously a technology that is most fitted for a systematic study of all these aspects and provides the possibility of creating complex parts based on digital models using the selected powder compositions. It was noted that:

1. The new concept, Material Genome, allows consolidating the efforts aimed to develop such directions as "new materials," "computer technologies for modeling and production of parts" and "additive manufacturing" by providing a single tool that helps to achieve breakthrough results by applying new methods and approaches.
2. The DMD and SLM are suitable for obtaining of 3D samples with a constant or variable composition of the material and can be used for combinatorial design and development of new alloys. The LAM allows the creation of compositionally piecewise-continuous gradient materials and obtainment in situ of new alloys that are not necessarily made from pre-prepared metal powders and is an effective tool for the rapid development of a new alloy. An additional advantage of the DMD in comparison with the SLM in the context of combinatorial metallurgical synthesis is high cladding rates and large dimensions of 3D parts, which are not limited by the dimensions of the synthesis chamber in the SLM installation.
3. Equally important is the possibility to obtain with the aid of the LAM, compositions and microstructures of alloys that are not available for traditional technologies. This principle feature can be used as a goal of combinatorial development of unique alloys for the LAM. It should also be noted that with the DMD, a gradient sample comprising parts from different alloys can be subjected to the HIP (post-treatment) and further research of the alloys that are changing in their composition from the viewpoint of their behavior during the thermo-mechanical treatment.

## Author details

Igor Shishkovsky

Address all correspondence to: shishkowsky@gmail.com

Lebedev Physics Institute of Russian Academy of Sciences, Samara, Russian Federation

## References

[1] Materials Genome Initiative for Global Competitiveness. Available from: https://www.mgi.gov/sites/default/files/documents/materials_genome_initiative-final.pdf [June 24, 2011]

[2] President Obama Launches Advanced Manufacturing Partnership. Available from: https://www.nist.gov/news-events/news/2011/06/president-obama-launches-advanced-manufacturing-partnership [June 24, 2011]

[3] America Makes—National Additive Manufacturing Innovation Institute (NAMII) Available from: https://www.americamakes.us/

[4] The Lightweight Modern Metals Manufacturing Institute—NIST. Available from: https://www.nist.gov/sites/default/files/documents/el/msid/18_lBrown.pdf

[5] Digital Manufacturing and Design Innovation Institute—UI Labs. Available from: http://www.uilabs.org/innovation-platforms/manufacturing/

[6] Industry 4.0 Challenges and solutions for the digital transformation and use of exponential technologies. Deloitte—Audit. Tax. Consulting. Corporate Finance. Available from: https://www2.deloitte.com/content/dam/Deloitte/ch/Documents/manufacturing/ch-en-manufacturing-industry-4-0-24102014.pdf

[7] 2nd Annual Principal Investigator Meeting. Accelerating Materials Research, Meeting Societal Needs, Building Infrastructure for Success. DOE/NSF Materials Genome Initiative. Bethesda, MD; 12-13 January 2015. Available from: https://www.mgi.gov/sites/default/files/documents/2015_MGI_PI_Meeting_Abstract_Book.pdf

[8] Third Principal Investigator Meeting. Accelerating Materials Research. Materials Genome Initiative. Available from: https://www.mgi.gov/sites/default/files/documents/2016_Abstract_Book_Final.pdf

[9] Modeling Across Scales: A Road mapping Study for Connecting Materials Models and Simulations Across Length and Time Scales. Available form: http://www.tms.org/portal/PUBLICATIONS/Studies/Modeling_Across_Scales/portal/Publications/Studies/Modeling_Across_Scales.aspx

[10] Shishkovsky Igor V, editor. New Trends in 3D Printing. Rijeka, Croatia: InThech Publsh.; 2016. 268 p. ISBN: 978-953-51-2480-1. (Open access)

[11] Knoll H, Ocylok S, Weisheit A, et al. Combinatorial alloy design by laser additive manufacturing. Steel Research International. 2017;**88**:1600416. DOI: 10.1002/srin.201600416

[12] Springer H, Raabe D. Rapid alloy prototyping: Compositional and thermo-mechanical high throughput bulk combinatorial design of structural materials based on the example of 30Mn-1.2C-xAl triplex steels. Acta Materialia. 2012;**60**:4950-4959

[13] Raabe D, Springer H, Gutierrez-Urrutia I, et al. Alloy design, combinatorial synthesis, and microstructure-property relations for low-density Fe-Mn-Al-C austenitic steels. JOM. 2014;**66**:1845-1856

[14] Pradeep KG, Tasan CC, Yao MJ, et al. Non-equiatomic high entropy alloys: Approach towards rapid alloy screening and property-oriented design. Materials Science and Engineering A. 2015;**648**:183-192

[15] Li Z, Pradeep KG, Deng Y, et al. Metastable high-entropy dual-phase alloys overcome the strength-ductility trade-off. Nature. 2016;**534**:227

[16] Tasan CC, Deng Y, Pradeep KG, et al. Composition dependence of phase stability, deformation mechanisms, and mechanical properties of the CoCrFeMnNi high-entropy alloy system. JOM. 2014;**66**:1993-2001

[17] Shishkovsky IV, Nazarov AP, Kotoban DV, Kakovkina NG. Comparison of additive technologies for gradient aerospace part fabrication from nickel based superalloys. In: Aliofkhazraei M, editor. Superalloys. Rijeka, Croatia: InTech Publ.; 2015. 344 p. DOI: 10.5772/61121

[18] Shishkovsky IV. Laser controlled intermetallics synthesis during surface cladding. In: Lawrence J et al., editors. Laser Surface Engineering. Processes and Applications. Woodhead Publishing. 2014. 718 p. DOI: 10.1016/B978-1-78242-074-3.00011-8

[19] Springer H, Beide M, Raabe D. Bulk combinatorial design of ductile martensitic stainless steels through confined martensite-to-austenite reversion. Materials Science and Engineering A. 2013;**582**:235-244

[20] Springer H, Belde M, Raabe D. Combinatorial design of transitory constitution steels: Coupling high strength with inherent formability and weldability through sequenced austenite stability. Materials & Design. 2016;**90**:1100-1109

[21] Aparicio-Fernandez R, Springer H, Szczepaniak A, et al. In-situ metal matrix composite steels: Effect of alloying and annealing on morphology, structure and mechanical properties of TiB2 particle containing high modulus steels. Acta Materialia. 2016;**107**:38-48

[22] Shishkovsky IV. Synthesis of functional gradient parts via RP methods. Rapid Prototyping Journal. 2001;**7**(4):207-211

[23] Collins PC, Banerjee R, Banerjee S, Fraser HL. Laser deposition of compositionally graded titanium-vanadium and titanium-molybdenum alloys. Materials Science and Engineering. 2003;**A352**:118-128

[24] Hofmann DC, Roberts S, Otis R, et al. Developing gradient metal alloys through radial deposition additive manufacturing. Scientific Reports. 2014;**4**:5357. DOI: 10.1038/srep05357

[25] Ian Gibson, David W. Rosen, Brent Stucker. Additive Manufacturing Technologies; Rapid Prototyping to Direct Digital Manufacturing; Verlag: Springer US; 2010. ISBN: 978-1-4419-1119-3. https://www.springerprofessional.de/additive-manufacturing-technologies/1719670

[26] Shishkovsky IV. Fundamentals of Additive Technologies of High Resolution. Saint-Petersburg: Piter Publ; 2016. 400 p. ISBN: 978-5-496-02049-7 (in Russian)

[27] Jagle EA, Choi PP, Humbeeck J, Raabe D. Precipitation and austenite reversion behavior of a maraging steel produced by selective laser melting. Journal of Materials Research. 2014;**29**(17):2072-2079

[28] Shishkovsky IV. Combinatorial design of alloys via laser additive technologies. Stankoinstrument. 2017;**3**:38-49. DOI: 10.22184/24999407.2017.8.3.38.49 (in Russian)

Chapter 2

# A Two-Dimensional Simulation of Grain Structure Growth within Substrate and Fusion Zone during Direct Metal Deposition

Jingwei Zhang, Lei Yan, Wei Li and Frank Liou

Additional information is available at the end of the chapter

http://dx.doi.org/10.5772/intechopen.73107

**Abstract**

In this chapter, a predictive multiscale model based on a cellular automaton (CA)-finite element (FE) method has been developed to simulate thermal history and microstructure evolution during metal solidification for direct metal deposition (DMD) process. The macroscopic FE calculation that is validated by the thermocouple experiment is developed to simulate the transient temperature field and cooling rate of single layer and multiple layers. In order to integrate the different scales, a CA-FE coupled model is developed to combine with thermal history and simulate grain growth. In the mesoscopic CA model, heterogeneous nucleation sites, grain growth orientation and rate, epitaxial growth, remelting of preexisting grains, metal addition, grain competitive growth and columnar to equiaxed phenomena are simulated. The CA model is able to show the entrapment of neighboring cells and the relationship between undercooling and the grain growth rate. The model predicts the grain size and morphological evolution during the solidification phase of the deposition process. The developed "decentered polygon" growth algorithm is appropriate for the nonuniform temperature field. Finally, the single- and multiple-layer DMD experiments are conducted to validate the characteristics of grain features in the simulation.

**Keywords:** finite element, cellular automata, grain morphology, direct metal deposition, thermal modeling

## 1. Introduction

Compared with the conventional subtractive manufacturing technologies, additive manufacturing (AM) has unique advantages including low heat input, small heat-affected zone, solid-free-form fabrication, near-net-shape and so on. Direct metal deposition (DMD), a rapid developing AM

technique, is able to manufacture a fully dense metal part without intermediate steps, which is especially appropriate for the heterogeneous components manufacturing. During the deposition process, solidification thermodynamics determined by a series of process parameters affect microstructure evolution, which directly affects materials' mechanical properties. The temperature field history and the cooling rate are the key factors to control the solidification microstructure after DMD process [1]. Several approaches, including stochastic and deterministic, have been taken to model solidification microstructure evolution. Anderson and Srolovitz et al. [2, 3] developed a Monte Carlo (MC) stochastic method to simulate the grain growth, grain size distribution, curvature and growth rate as well as their interrelationships. Saito and Enomoto [4] incorporated the anisotropy of the grain boundary energy, the pinning effect of precipitates on growth kinetics into the MC simulation. Another idea of modeling is the deterministic approach. Chen [5] investigated a phase field (PF) method to model and to predict the mesoscale morphological and microstructure evolution in materials. C.E. Krill III, Böttger B, and Moelans N et al. [6–8] developed PF to simulate 2D grain growth, 3D grain growth and equiaxed solidification. However, a phase field model usually carries a very high computational cost because of a requirement for a particularly fine computational grid.

In order to reduce the computational cost, Rappaz and Gandin [9] put forward a 2D cellular automaton approach to model the grain structure formation in the solidification process. The model includes the mechanisms of heterogeneous nucleation and grain growth during the casting process. Nucleation occurring at the solid/liquid interface and the liquid bulk is treated by using different nucleation sites preference. The crystallographic orientation and locations of the grains are randomly selected among a certain number of orientation classes and millions of CA cells, respectively. However, the model was only applied to uniform temperature field. In order to develop the nonuniform temperature prediction, Gandin and Rappaz [10] proposed a 2D cellular automaton (CA) technique for the simulation of grain formation during solidification. The nonuniform temperature situation was fully coupled to finite element (FE) heat flow calculation with enthalpy. This progress made it possible to combine the temperature field history with the microstructure evolution. The coupled CA-FE model is applied to A1-7 wt% Si alloy. A 3D CA-FE model was analyzed for the prediction of dendritic grain structures formed during solidification [11]. The potentiality of the CA-FE model is demonstrated through the predictions of typical grain structures formed during the investment casting and continuous casting processes. Based on the features of several developing approaches, Choudhury et al. [12] compared a CA model with a PF model for dendritic solidification of an Al-4 wt%Cu alloy, 2D and 3D at different undercooling conditions. In 2D case, there is a very good agreement of the simulated tip properties. At high undercooling, the CA model becomes more favorable, as its reproduction of the theoretical behavior is improved. Since the CA model can simulate at coarse scales during a relatively short time, its output can be employed as the input for a PF simulation in order to resolve finer details of microstructure formation within grains. This can be utilized to build a hybrid model to integrate CA high efficiency and PF accuracy. Dore [13] investigated quantitative prediction of microsegregation during solidification of the ternary alloy system, which is applied to solidification of Al–Mg–Si. Jarvis et al. [14] firstly compared 1D, 2D and 3D cellular automaton finite difference (CA-FD) simulations of nonequilibrium solidification in Al–3.95Cu–0.8Mg ternary alloy. It has been demonstrated that there is a good agreement between all the CA-FD models in terms of primary $\alpha$-Al phase. However, final dendrite arm spacings of 2D and 3D are slightly overestimated.

High cooling rate and nonequilibrium are typical characteristics of the DMD technique comparing conventional casting process and simulation. Grujicic et al. [15] proposed a modified CA-based method to investigate the evolution of solidification grain microstructure during the LENS rapid fabrication process. This research established the relationship between the process parameters (e.g., laser power, laser velocity) and solidification microstructure in binary metallic alloy. The finite difference analysis was also coupled with the modified CA to calculate the temperature field as the input of microstructure prediction. Kelly and Kampe [16, 17] developed the thermal history in DMD of Ti6Al4V and microstructural characterization. Nie et al. [18] developed a multiscale model to simulate microstructure evolution during laser additive manufacturing solidification. The study presented the relationship between the solidification conditions and the resultant microstructure, especially Laves phase particles in Ni-based superalloy. Rodgers et al. [19] proposed a 2D mesoscale model to simulate grain structure near a moving heat source with kinetic Monte Carlo simulator during electric beam melting (EBM) process. The method is capable of simulating both singlepass and multipass welds grain morphology. It also investigates the influence of initial substrate grain size on HAZ and FZ grain shape and size. Rai et al. [20] coupled a lattice Boltzmann (LB) and cellular automaton (CA) to simulate the microstructure evolution during electron beam melting. Initial grain selection at the base plate, grain boundary perturbation, grain nucleation due to unmolten powder particles in the bulk, grain penetration can all be simulated. The influence of process parameters on the final grain structure and texture evolution is analyzed. Keller et al. [21] investigated aspects of microstructure and microsegregation during rapid solidification in a laser powder bed fusion additive manufacturing process. Finite element analysis is employed to simulate the laser melt pool and temperature field. Microsegregation between dendritic arms is calculated by using the Scheil-Gulliver solidification model and DICTRA software. Phase field is developed to produce microstructures with primary cellular/dendritic arm spacing. However, there are few investigations on microstructure evolution prediction based on substrate and fusion zone during DMD process. Compared to other powder bed additive manufacturing process, there is different thermal cycle and the cooling rates for DMD process, which results in different microstructure. This part-level simulation on microstructure is critical because it provides the foundation for the prediction and control of mechanical properties.

CA simulation is appropriate for mesoscale modeling of grain structure because it does not consider much details inside a specific grain such as secondary dendritic arm spacing (SDAS) and microsegregation. Since it belongs to mesoscale model and does not cost as much computational resources as other microscale models, such as phase field and molecular dynamic, these characteristics of CA model make it appropriate for simulating the part-level grain structure instead of a very small region including less than a hundred grains. Thus, it can be used to predict and control the mechanical properties of the whole part based on the part-level grain structure under different parameters. Molecular dynamic (MD) simulation of microstructural evolution during additive manufacturing [22] is focused on a microscalability, which is between nanometer and micrometer. MD simulation can provide a method to investigate the crystallization process within the HAZ and clarify its crystallization mechanism because it is difficult to observe directly the crystallization process in the HAZ during the cyclic heating and cooling process. Even though MD can investigate microstructure evolution on a molecular level, it will cost too much resource to simulate the whole part structure and properties. PF model [21, 23], a microscopic one, can be used to simulate the solute concentration and phase transformation by solving the potential equation. The coefficients in the evolution equation

of phase-field variables are related to the material parameters so that it can quantitatively simulate grain growth within a finer scale compared to CA and MC. Lattice Boltzmann (LB) method is adopted to numerically simulate the solute transport within the melt pool domain because it is appropriate for the complex geometry shape and is built from the temporal and spatial discretized grid, avoiding solving macroscopic N-S equations. The computational domain is discretized into regular lattices with the same cell size as the CA model. The governing equation and boundary conditions for transport process are described in detail in Refs. [24–27]. The comparison of AM microstructure simulation methods is shown in **Table 1**. The current CAFÉ model can be used to consider multiple components if it considers the solute concentration and there is no chemical reaction and intermetallic phase formation during the solidification process. However, it is not capable of determining the mechanical properties directly if it is not incorporated with other models such as Hall-Petch model.

| Methods | Advantages | Limitations |
|---|---|---|
| Cellular automaton | • Coupled prediction of thermal history and grain structure<br>• Predicts microstructure with multiple heat source passes<br>• Including crystallographic orientation and texture<br>• Relatively low computational cost | • No HAZ grain evolution<br>• Unavailable open source code<br>• Lack of grain substructure |
| Monte Carlo | • Predicts 3D microstructures with hundreds of heat source passes<br>• Microstructure evolution within fusion zone and HAZ<br>• Included in the open source code | • Idealized molten zone<br>• No direct coupling of thermal and microstructural models<br>• Does not incorporate material texture or anisotropy. |
| Phase field | • Available subgrain features<br>• Including solute concentration and phase transformation<br>• Material parameters related to phase-field variables | • High computational cost<br>• Small computational domain<br>• Solving complex potential equations |
| Lattice Boltzmann | • Allows for coupled thermos-fluid and microstructure evolution on same lattice<br>• Including crystallographic orientation and texture<br>• Appropriate for the complex geometry shape<br>• No need to solve macroscopic N-S equations | • Unstable solutions for many regimes<br>• No solid-state grain evolution after solidification<br>• Unavailable open source code |
| Molecular dynamics | • Explain crystallization mechanism<br>• Simulating microstructure within HAZ | • Costs too much computational resource<br>• Very small computational region |
| Empirical microstructure models | • Estimates microstructural features over large parts<br>• Allows extension of preexisting thermal models. | • Does not provide microstructure for further analysis.<br>• Requires estimation of thermal condition. |

**Table 1.** Comparison of AM microstructure simulation methods.

http://dx.doi.org/10.5772/intechopen.73107

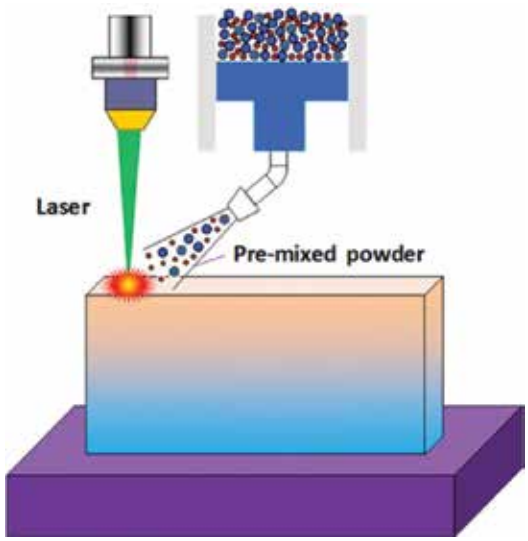


**Figure 1.** Laser powder deposition schematic.

In this study, a predictive multiscale model based on a cellular automaton (CA)-finite element (FE) method has been developed to simulate thermal history and microstructure evolution during metal solidification for a laser-based additive manufacturing process shown in **Figure 1**. ABAQUS was used to calculate the temperature field of the whole part, which offers the macroscopic FE nodes' temperature. In order to integrate the different scales, a coupled model is developed to combine with thermal history and simulate nucleation site, grain growth orientation and rate, epitaxial growth of new grains, remelting of preexisting grains, metal addition and grain competitive growth. Interpolation was utilized to obtain the finer nodes' temperature based on the FE nodes result. The temperature field was validated by the type K thermocouples. The CA model, which was able to show the entrapment of neighboring cells and the relationship between undercooling and the grain growth rate, was built to simulate the microstructure information such as the grain size and columnar grain orientation. The developed "decentered polygon" algorithm is more appropriate for grain structure development in the highly nonuniform temperature field. This simulation will lead to new knowledge that simulates the grain structure development of single- and multiple-layer deposition during DMD process. The microstructure simulation results were validated by the experiment. The model parameters for the simulations were based on Ti-6Al-4V material (**Figure 1**).

## 2. Mathematical model

### 2.1. Ti6Al4V transient temperature field during the deposition process

In the direct metal deposition (DMD) process, the temperature history of the whole domain directly influences the deposition microstructure, which is critical to mechanical properties [28]. In order to obtain the microstructure information during the solidification process, the temperature field must be known at each time step. The transient temperature field throughout

the domain was obtained by solving the 3D heat conduction Eq. (1), in the substrate, along with the appropriate initial and boundary conditions [29].

$$\rho(T)\cdot c_p(T)\cdot\frac{\partial T}{\partial t} = \frac{\partial}{\partial x}\left(k(T)\frac{\partial T}{\partial x}\right)+\frac{\partial}{\partial y}\left(k(T)\frac{\partial T}{\partial y}\right)+\frac{\partial}{\partial z}\left(k(T)\frac{\partial T}{\partial z}\right)+\dot{Q}, \tag{1}$$

where T is the temperature, $\rho(T)$ is the density, $c_p(T)$ is the specific heat, $k(T)$ is the heat conductivity and Q is the internal heat generation following certain energy distribution per unit volume.

The initial conditions applied to solve Eq. (1) were:

$$T(x, y, z, 0) = T_0 \text{ and } T(x, y, z, \infty) = T_0, \tag{2}$$

where $T_0$ is the ambient temperature. In this study, $T_0$ was set as room temperature, 298 K. The boundary conditions, including thermal convection and radiation, are described by Newton's law of cooling and the Stefan-Boltzmann law, respectively. The laser heating source term, $\dot{Q}$ in Eq. (1), was also considered in the boundary conditions as a surface heat source. The boundary conditions then could be expressed as [29]

$$K(\Delta T\cdot n)\big|_\Gamma = \begin{cases} \left[-h(T-T_0)-\varepsilon(T)\sigma\left(T^4-T_0^4\right)\right]\big|_\Gamma & \Gamma \notin \Lambda \\ \left[Q-h(T-T_0)-\varepsilon(T)\sigma\left(T^4-T_0^4\right)\right]\big|_\Gamma & \Gamma \in \Lambda' \end{cases} \tag{3}$$

where k, T, $T_0$ and Q bear their previous definitions, n is the normal vector of the surface, h is the heat convection coefficient, $\varepsilon(T)$ is the emissivity, $\sigma$ is the Stefan-Boltzmann constant, which is $5.6704\times10^{-8}\ W/m^2K^4$, $\Gamma$ represents the surfaces of the work piece and $\Lambda$ denotes the surface area irradiated by the Gaussian laser beam.

In order to simulate the thermal history during the direct metal deposition more efficiently and reduce the computational cost, some assumptions were taken into account. In the experiment, a Gaussian distributed laser beam was utilized to melt the substrate vertically with a nonuniform power density [30]. Thus, the transverse intensity variation is described as Eq. (4):

$$I(r, y) = \alpha\frac{P}{\pi w(y)^2/2}\exp\left(-2\frac{r^2}{w(y)^2}\right), \tag{4}$$

where $\alpha$ is the laser absorption coefficient, P is the power of the continuous laser and $w(y)$ is the distance from the beam axis where the optical intensity drops to $1/e^2(\approx 13.5\%)$ of the value on the beam axis. $\alpha$ was set as 0.4 based on numerical experiments in the LAMP laboratory and $w(y)$ is 1 mm in this simulation. The motion of laser beam was simulated by adjusting the position of beam center R with programming a user subroutine "DFLUX" in ABAQUS. The formula of R is as follows:

$$R = \left[\left(x-\int_{t_0}^{t} u\,dt\right)+\left(y-\int_{t_0}^{t} v\,dt\right)+\left(z-\int_{t_0}^{t} w\,dt\right)\right]^{1/2}, \tag{5}$$

where x, y and z are the spatial coordinates of the Gaussian laser beam center, and u, v and w are the laser moving velocities.

The Marangoni effect caused by the thermocapillary phenomena can directly influence the temperature field in the whole domain, so it is considered to obtain more accurate thermal history during DMD [31]. The artificial thermal conductivity was put forward to address the Marangoni effect in the finite element method [32]

$$k_m(T) = \begin{cases} k(T), & T \le T_{liq} \\ 2.5k(T), & T > T_{liq} \end{cases}, \tag{6}$$

where $k_m$ is the modified thermal conductivity and $T_{liq}$ is the liquidus temperature.

In the FEA model, the powder addition was simulated by activating elements in many small steps [33]. The width of the deposit area is assumed to be the same as the Gaussian laser beam. The thickness of each layer is calculated by transverse speed, powder feed rate and powder absorption efficiency. The deposit geometry, boundary condition and heat flux were updated after each step.

### 2.2. Ti6Al4V morphology prediction after solidification

Heterogeneous nucleation occurs nearly instantaneously at a characteristic undercooling. The locations and crystallographic orientation of the new nuclei are randomly chosen at the surface or in the liquid. As explained by Oldfield [34], the continuous nucleation distribution, $dn/d\Delta T'$, which characterizes the relationship between undercooling and the grain density, is described by a Gaussian distribution both at the mold wall and in the bulk liquid. The parameters of these two distributions, including maximum nucleation density $n_{max}$, the mean undercooling $\Delta T_N$ and the standard deviation of the grain density distribution $\Delta T_\sigma$, can be obtained from experiments and grain size measurements. The grain density, $n(\Delta T)$, is given by Eq. (7):

$$n(\Delta T) = \int_0^{\Delta T} \frac{dn}{d\Delta T'} d\Delta T' = \int_0^{\Delta T} \frac{n_{max}}{\Delta T_\sigma \sqrt{2\pi}} exp\left[-\frac{1}{2}\left(\frac{\Delta T' - \Delta T_N}{\Delta T_\sigma}\right)\right] d\Delta T', \tag{7}$$

where $n_{max}$ is the maximum nucleation density of nucleation grains, which is obtained by the integral of the nucleation distribution (from zero undercooling to infinite undercooling). $\Delta T_N$ and $\Delta T_\sigma$ are the mean undercooling and standard deviation of the grain density distribution, respectively. Here, all temperatures are in Kelvin.

Undercooling is the most important factor in the columnar and dendrite growth rate and grain size. The total undercooling of the dendritic tip consists of three parts such as solute undercooling, thermal undercooling and curvature undercooling. For most metallic alloys, the kinetic undercooling for atom attachment is small, so it is neglected [35]. The total undercooling can be calculated as follows:

$$\Delta T = m C_0 \left[1 - A(P_C)\right] + \theta_t I(P_t) + \frac{2\Gamma}{R}, \tag{8}$$

where m is the liquidus slope, Γ is the Gibbs-Thomson coefficient, $C_0$ is the solute concentration in the liquid far from the solid-liquid interface, $P_t$ and $P_c$ are the thermal and solutal Peclet numbers, respectively, k is the solute partition coefficient at the solid-liquid interface, $A(P_c)$ equals $[1-(1-k)I(P_c)]^{-1}$, $\theta_t$ is the unit thermal undercooling $\left(=\Delta h_f/c\right)$ and R is the radius of the dendritic tip.

For the laser deposition process, the rapid solidification condition corresponds to a high Peclet number at which the dendritic tip radius is given by Eq. (9)

$$R = \left[\frac{\Gamma}{\sigma^*(m G_c^* - G^*)}\right]^{1/2}, \tag{9}$$

where $\sigma^*$ is the marginal stability constant, approximately equals $1/4\pi^2$ [36], and $G^*$ and $G_c^*$ are the effective temperature gradient and concentration gradient, respectively.

### 2.3. Coupling macroscopic FE and mesoscopic CA models

The temperature field result can be used to calculate enthalpy increment, which is necessary to calculate enthalpy at each time step. A linearized implicit FE enthalpy formulation of the heat flow equation can be given [10]

$$\left[\frac{1}{\Delta t}\cdot[M] + [K]^t\left[\frac{\partial T}{\partial H}\right]^t\right]\cdot\{\delta H\} = -\{K\}^t\cdot\{T\}^t + \{b\}^t, \tag{10}$$

where {M} is the mass matrix, {K} is the conductivity matrix, {b} is the boundary condition vector and {T} and {H} are the temperature and enthalpy vectors at each node of the FE mesh, respectively. The Newton method and Euler implicit iteration are included in (10). This set of equations can be solved using the Gauss elimination method for {δH}.

$$\delta H = \rho\cdot c_p\cdot[T^{t+\delta t} - T^t] - \Delta H_f\cdot\delta f_s. \tag{11}$$

Thus, the next time-step enthalpy can be obtained by the relationship of $H_i^{t+1} = H_i^t + \delta H$. The new temperature field can be obtained from the coupling model using (11). $\Delta H_f$ is the latent heat of fusion per unit volume. $f_s$ represents the fraction of solid. $\delta f_s$ can be calculated as in [10].

In the FE macroscopic model, the temperature field was calculated on a relatively coarse mesh, but the solidification microstructure had to be developed on a finer regular CA mesh with a cell size in the order of the secondary dendrite arm spacing (SDAS). **Figure 2** indicates the interpolate relationship between coarse FE nodes and fine CA cells. The known temperature $T_n^t$ and the volumetric enthalpy variation $\delta H_n$ were interpolated into the CA network by the linear interpolation in Eqs. (12) and (13). $\phi_{vn}$ is the interpolation coefficient. Every CA cell temperature in the calculation domain can be obtained with this interpolation.

$$T_v^t = \sum_n \phi_{vn}\cdot T_n^t \tag{12}$$

$$H_v^t = \sum_n \phi_{vn}\cdot H_n^t \tag{13}$$

http://dx.doi.org/10.5772/intechopen.73107

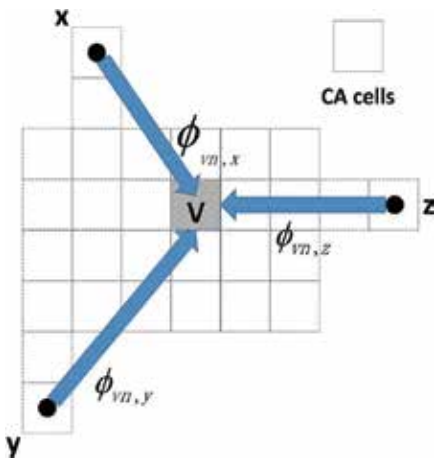


**Figure 2.** x, y and z represent the FE temperature nodes (coarse grids) and v represents the CA cells (fine grids). The three linear interpolation coefficients from FE nodes x, y and z to CA cells v are $\phi$ vn,x, $\phi_{vn,y}$ and $\phi_{vn,z}$.

The finer temperature, $T_v^t$, and enthalpy variations, $\delta H_v^t$, in regular CA cells were used in Eq. (13) to yield the temperature in the next microtime step. After a few microtime steps, the temperature field in the CA network could be substituted into the coarser nodes of the macroscopic model. The interpolated temperature field is employed as the model input. Heterogeneous nucleation, grain growth orientation and grain growth are solved in the CA-FE model in

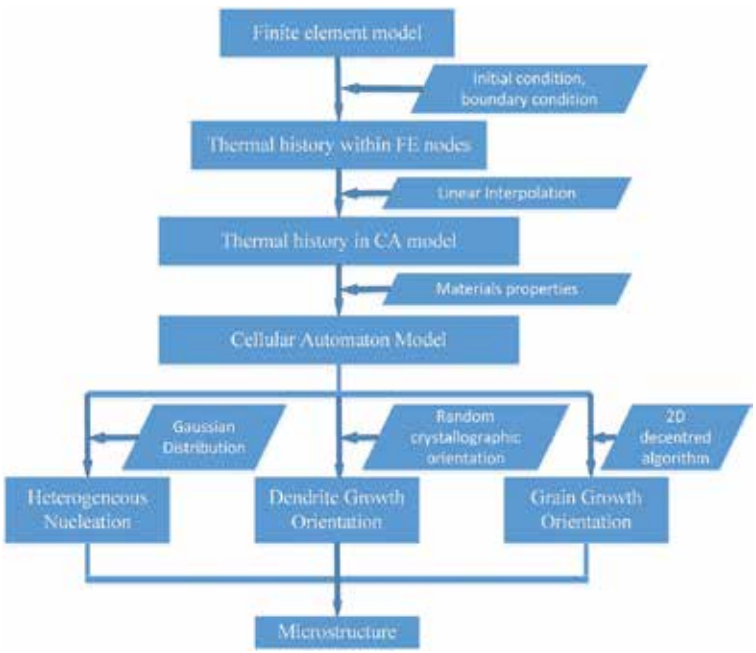


**Figure 3.** Flow chart of the coupling CA-FE model.

terms of nucleation location distribution, random crystallographic orientation and CA cells capture. **Figure 3** indicates the flow chart of coupling FE-CA model. The details of the CA growth algorithm are shown in **Figure 4**.

**Figure 5** illustrates the conventional and modified cell capture algorithm. For the conventional method, the vertices of the square envelope move along the diagonal, and the growth of the square envelope is determined by the center cell temperature, not local temperature, at each time step, which results in the same growth rate for the four vertices. The grain orientation will be along with the axis of computational domain after a few time steps, thus, losing its original orientation information. The modified "decentered polygon" algorithm is implemented to control the grain growth within the melt pool and at the sold/liquid interface. Compared to the traditional "decentered square" algorithm of cell capturing, the modified "decentered polygon" algorithm does not need to create square for each cell when it begins to grow. Only the decentered polygon of a starting nucleated cell is tracked during the grain growth process, which reduces the computational cost. Besides, the modified algorithm can prevent grain orientations from realigning with x axis after a few growing steps because each cell will stop growing when Von Neumann and Moore neighbors are both solid. The controlling point growth rate is determined by the local cell temperature. Therefore, the region with higher thermal gradient will solidify faster along the steepest thermal gradient.

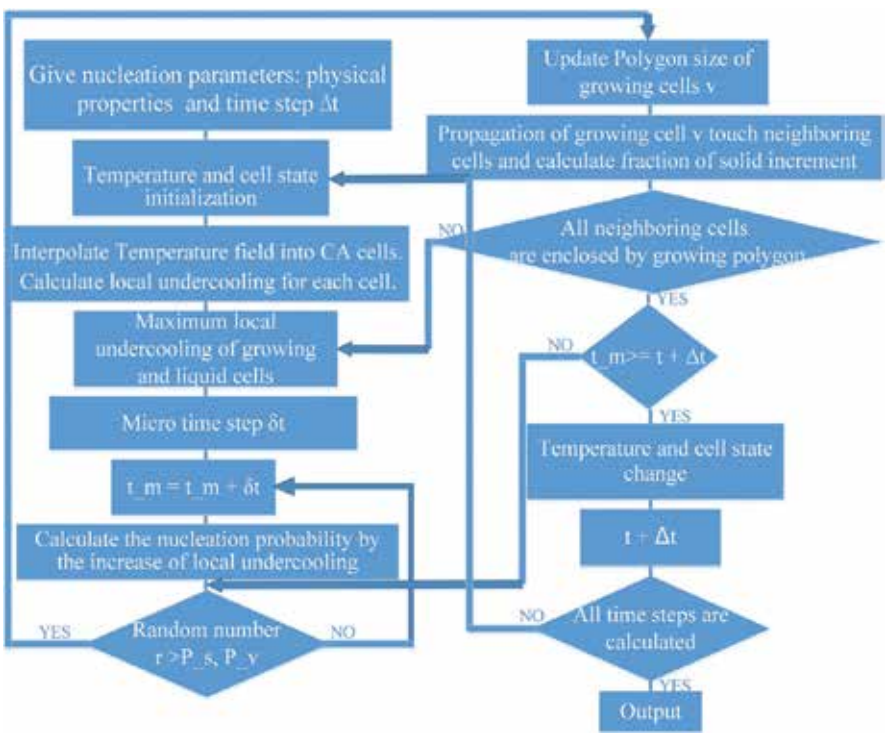


**Figure 4.** Flow chart of CA algorithm.

http://dx.doi.org/10.5772/intechopen.73107

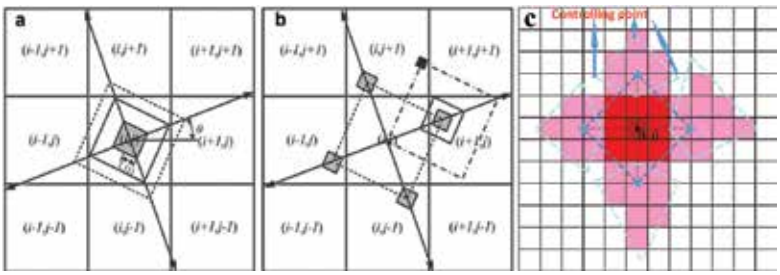


**Figure 5.** Illustration of the conventional and modified cell capture algorithm: (a) capturing rule of cell (i, j) within a decentered square, (b) capturing rule of eight neighboring cells before (i, j) growth termination [37] and (c) the modified cell capture and growth algorithm of "decentered polygon" with neighboring cells effect for cubic crystal alloys.

## 3. Results and discussion

### 3.1. Single-layer temperature and grain structure

The deposition temperature field and grain morphology were simulated first only in one layer. **Figure 6** shows thermal history of the whole block during the DMD process. **Figure 6(a)** indicates the temperature field of the whole block when laser beam is passing along the x direction at time = 1.0 s, while **Figure 6(b)** shows the temperature field when substrate cools down with laser off at time = 29.0 s. The total physical time of single-layer laser deposition is 2 s, while the cooling time is 28 s in the simulation. For each step, the step time is 0.1 s when the laser is shot on the surface of the deposited material. After 30 s of cooling down, the temperature distribution is more uniform. **Figure 7** indicates the thermal history of two nodes, which locate at the center point in the deposit and 1 mm away from the deposit. The result shows that the highest temperature in the deposit is approximately 2884 K, which occurred at the center of the Gaussian beam. The center node at 1 mm away from the deposit arrives at peak temperature of 1126 K that cannot melt the Ti6Al4V substrate. Based on every node's thermal history, the undercooling (discrepancy between liquidus temperature and current temperature) that is critical to resulting in grain nucleation and growth rate can be determined.

In order that the input of microstructure model is reliable, the temperature field is validated with four type-K thermocouples. The locations are shown in **Figure 8**. One is located at the starting of laser path, which distance to the laser is approximately 3–3.5 mm. Another three points are located by one side of laser path, which distance to the laser center is approximately 2 mm. Arduino device is used to sample the temperature data. A laser deposition experiment is conducted with the power of 750 W, scanning speed of 600 mm/min and 2 g/min for single-layer deposit. The difference between the experiment and the FEM modeling is less than 10°C shown in **Figure 9**. In **Figure 9(a)**, the delay between the simulated temperature and the thermocouple itself is more visible than **Figure 9(b)–(d)** because the distance of first thermocouple point is further than other three ones. In the real experiment, the substrate is fixed by the metal fixture, which resulting in the more heat conduction than the FEM model. Because of argon gas, forced convection occurred in the real experiment. This also causes lower cooling

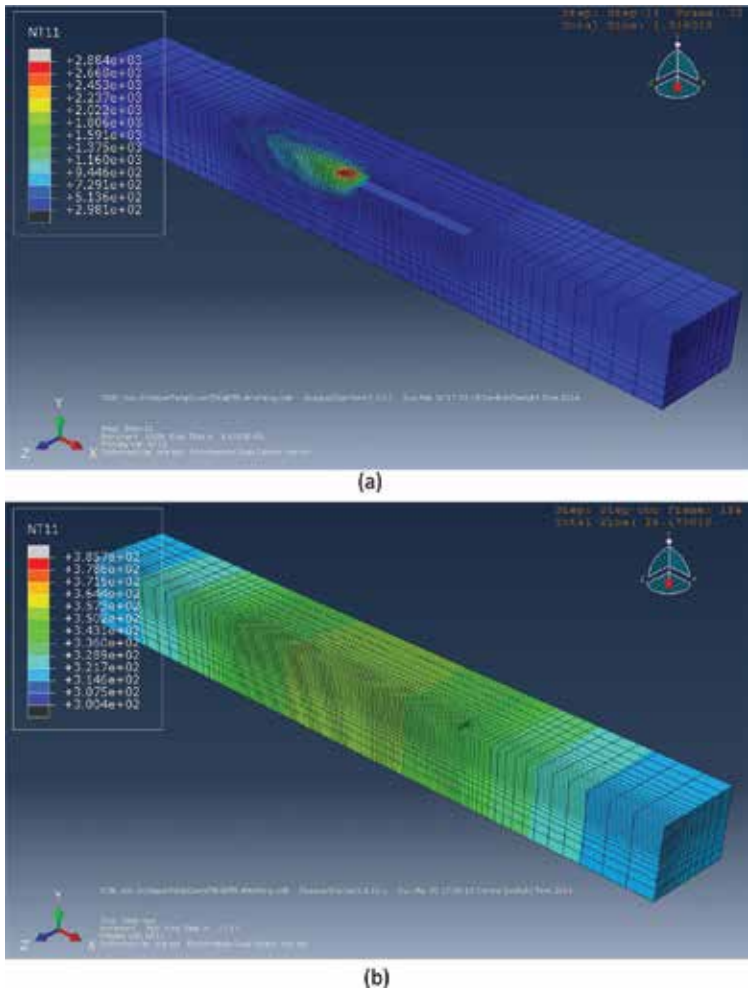


**Figure 6.** Cross-sectional simulated temperature distribution during single-layer laser deposition process. The deposition time is 2 s, while the cooling time is 28 s. (a) Temperature field at time = 1.0 s and (b) temperature field at time = 29.0 s.

rate in the temperature simulation. Because the difference between experiment and simulation is smaller than 10%, the current FEA modeling is still considered as a reasonable simulation of temperature field, which can provide the reliable thermal input for the CA model.

A laser deposition experiment is conducted with the power of 700 W, scanning speed of 600 mm/min and 2 g/min for single-layer deposit. For this case, the cross section shown in the figure is the computational domain. The cell size for this simulation is 6 × 6 μm. X and Y axes represent the number of cells. The simulation result from conventional method is shown in **Figure 10**. It can be observed that even though different grains own diverse orientation at the very beginning, the crystallographic orientation preference tends to be along with the axis after several time steps. Here, different colors represent various grain orientations. Finally, the equiaxed grains dominate the fusion zone. The original grain orientations are not kept during the solidification process. It does not agree well with the single-layer experimental result shown in **Figure 12**.

http://dx.doi.org/10.5772/intechopen.73107

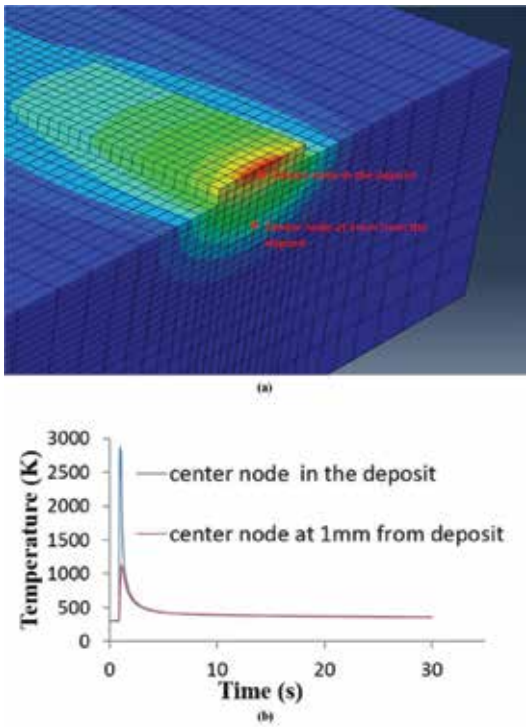


**Figure 7.** (a)Temperature field at t = 1s (b) Temperature history at the center node in the deposit and substrate.

The developed CA grain growth method is implemented under the same condition. According to the developed CAFÉ simulation, the single layer simulation result is shown in **Figure 11**. The grain keeps its original crystallization orientation when grain growth is modeled. The columnar grain can be identified from the solid/liquid interface. When grains continue to grow toward melt pool center, some grains overgrow other grains such that there are fewer grains further away from the solid/liquid interface.

Three samples of single-layer deposits are prepared with EDM cutting, grinding, polishing and etching. The optical microscope is shown in **Figure 12**. The comparison between simulation and experimental results is shown in **Figure 13**. An average of 20 measurements per sample is performed to determine the average grain size. It compares the experimental aver-

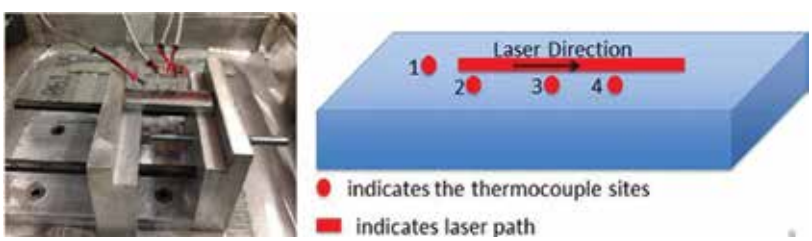


**Figure 8.** Thermocouples location and laser scan direction schematic diagram.

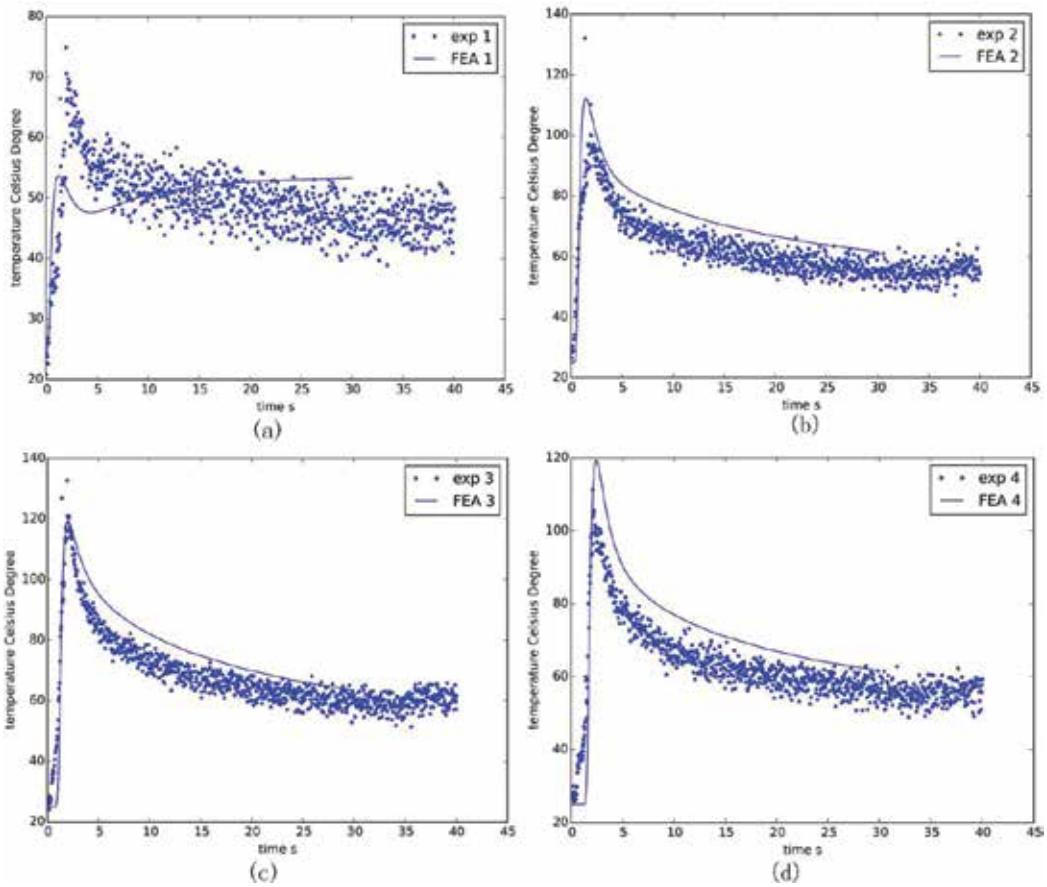


**Figure 9.** Temperature validation with four type-K thermocouples. (a), (b), (c) and (d) are measured at location 1, 2, 3 and 4, respectively.

age grain size with the predicted one. The shown data suggest that a 15% error between experimental measurements and predictions is present. This can be considered as a reasonable prediction of grain morphology and size.

### 3.2. Multilayer temperature and grain structure

**Figure 14** depicts the temperature field of the substrate and deposited material, including the 25-layer deposition materials added on the substrate when the laser is moved forward and backward. The laser deposition of multiple-layer Ti-6Al-4V was conducted with the power of 750 W, scanning speed of 200 mm/min and powder delivery of 2 g/min. The elemental size is nonuniform along the three directions because it is not necessary to apply fine elements to where the location is far from the molten pool. **Figure 15** shows that the thermal history and peak temperature of different layers are not identical. The higher layer performs higher thermal history because the higher layer accumulates more heat than the lower one, and it is closer to heat source.

http://dx.doi.org/10.5772/intechopen.73107

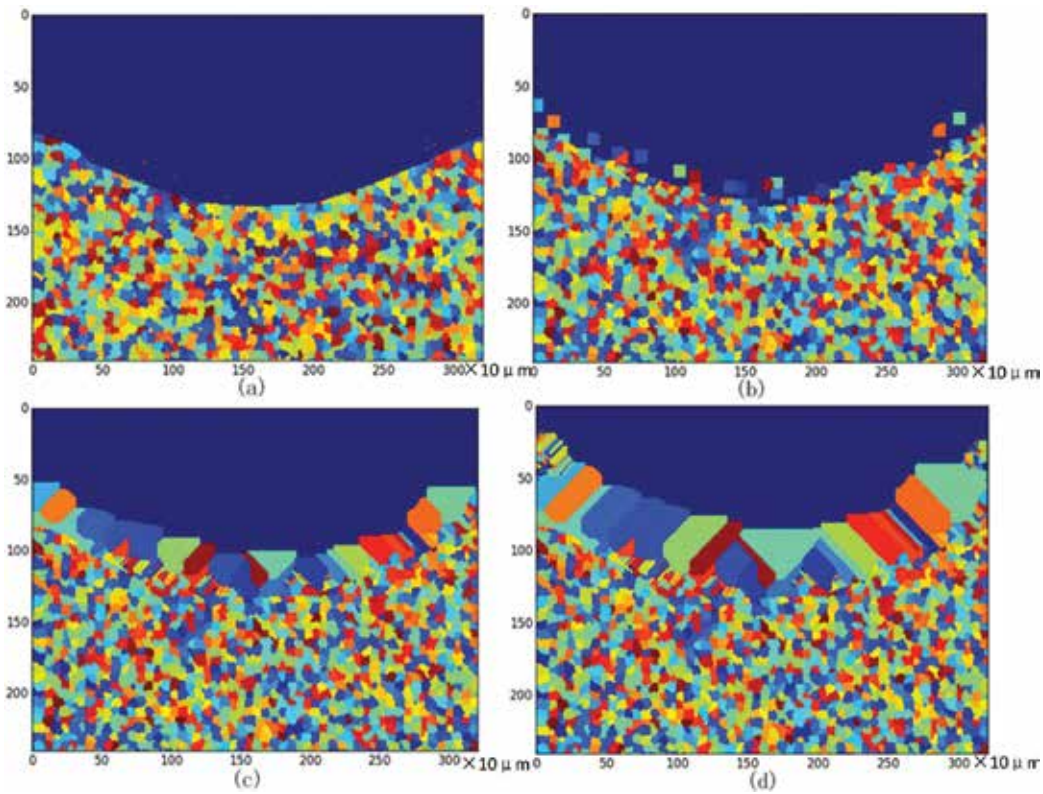


**Figure 10.** Grain structure of conventional growth method for single-layer Ti6Al4V deposition at (a) 5 ms, (b) 25 ms, (c) 45 ms and (d) 65 ms time step.

**Figure 16** shows Ti-6Al-4V deposition grain microstructure. The cross-sectional dimension of deposit region is 1.8 × 1.9 mm, which is close to 2 × 2 mm assumption in the simulation. In **Figure 16**, it can be observed that at the bottom deposition, crystallographic orientation is not only limited to the vertical direction. It can also be observed that columnar grains dominate in the laser deposition area. **Figure 16(a)** and **(b)** indicates the whole deposition region at different magnification and the locations of top and bottom region, while **Figure 16(c)** and **(d)** shows the grain size and shape with higher magnification. Under the same condition, the experiment is conducted, and the optical microscope images are taken. **Figure 16(e)** shows multiple layers of the Ti-6Al-4V grain morphology under the laser deposition process. Irregular grain shape and size can be obtained. When more layers were deposited, prior β columnar grains began to dominate, while equiaxed grains began disappearing. As the solidification process continues, competitive growth among different grains occurs. Therefore, the size of columnar grain increases, and the number of grains goes down. The orientations of the columnar grains were almost perpendicular to the laser motion's direction because the grains grew along the steepest thermal gradient direction. This phenomenon verifies the columnar grain orientation in the simulation result. The domain size in the CA model was 2 × 2mm. After measurement of grain size, it can be found in **Figure 17** that in the simulation, the grain size ranges from 113 to 346 μm. For the

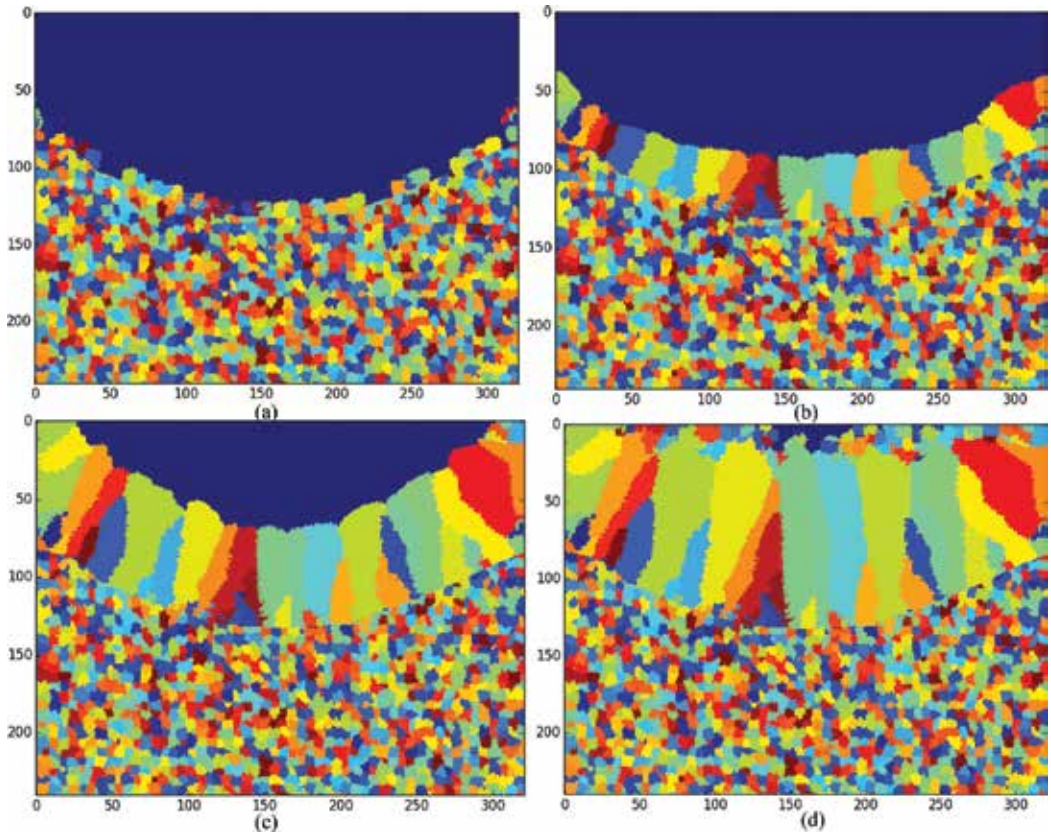


**Figure 11.** Grain structure of developed growth method for single-layer Ti6Al4V deposition at (a) 20 ms, (b) 40 ms, (c) 60 ms and (d) 80 ms time step.


**Figure 12.** Ti-6Al-4V single-layer deposition grain morphology at (a) 50x and (b) 200x.

http://dx.doi.org/10.5772/intechopen.73107

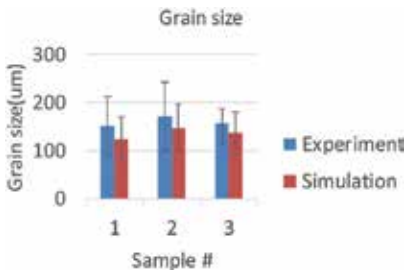


**Figure 13.** Grain size comparison between simulation and experiment.

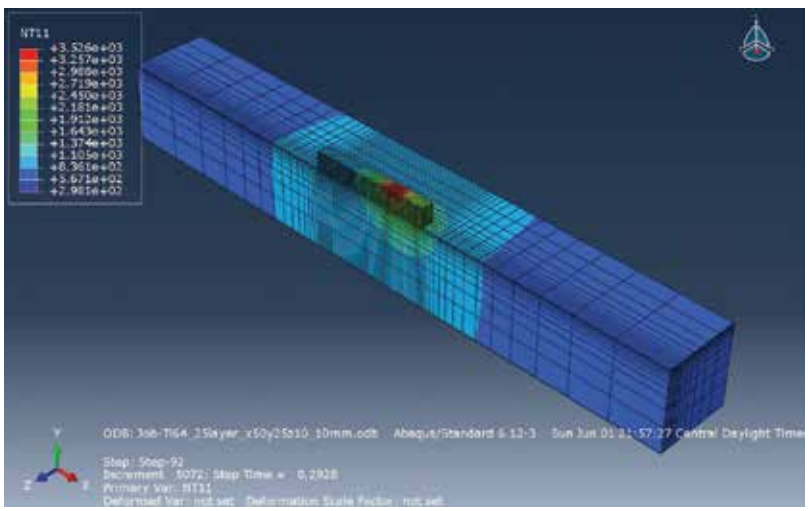


**Figure 14.** Thermal history for 25-layer Ti-6Al-4V laser deposition. This figure shows the 18th layer deposit temperature field.

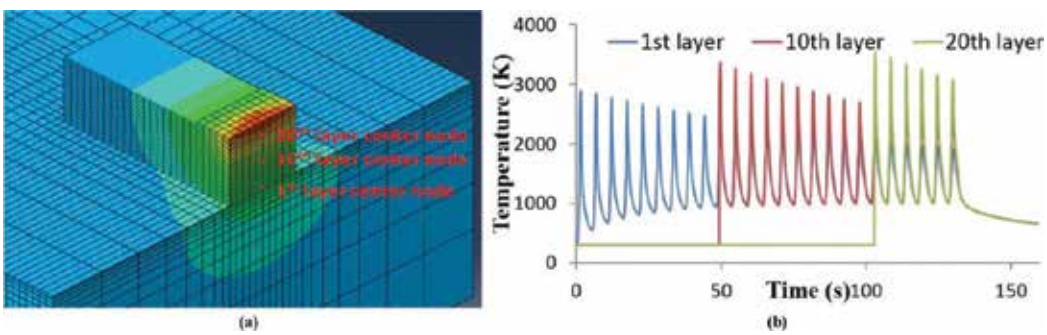


**Figure 15.** (a) Three nodes location cross section schematic and (b) thermal history of the center node at 1st, 10th and 20th layer.

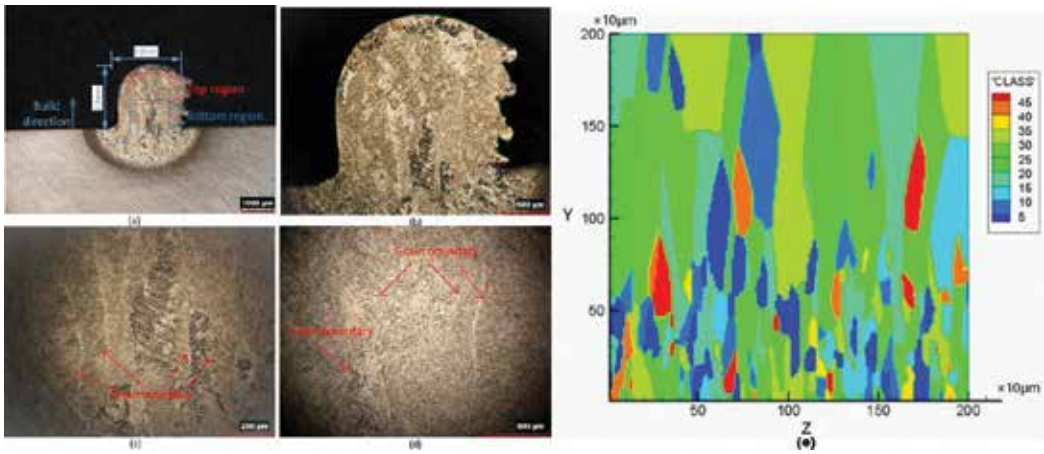


**Figure 16.** Ti-6Al-4V deposition grain morphologies. (a) and (b) The whole deposition, (c) the bottom region deposition and (d) the top region deposition. (e) Grain morphology modeling of 25-layer Ti-6Al-4V laser deposition. In the legend, "CLASS" represents orientations of different grains. Y and Z coordinates are in agreement with 25-layer thermal history result.

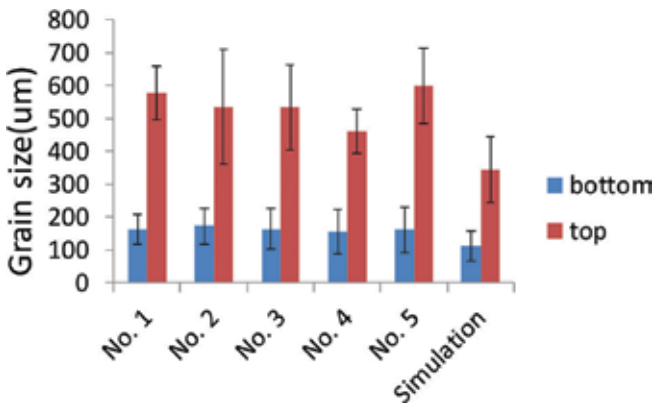


**Figure 17.** Grain size comparison of multiple layers between simulation and experiment.

experiment, the grain size ranges from 156 to 599 μm. The grain size at the bottom and top is larger than the simulation. This may be because it does not consider the cyclic heating and cooling process' effect on the solidified grain evolution. Usually, cyclic heating will coarsen the grain and make the grain become larger. This effect will be solved in the future research task.

**Figure 18** presents the simulated grain structure from Rai et al. [20] during powder bed additive manufacturing. It can be seen that some grains overgrow others at the top layers, and most surviving grains have negative misorientations indicating grain orientation is aligned well with the beam scanning direction. The detailed local grain boundary misorientation is determined by local thermal gradient and the neighboring grains' orientation. The rate of overgrowth process also has an effect on the grain boundary angle. Compared to multiple layer results in this investigation, it shows the similarity of grain overgrowth mechanism

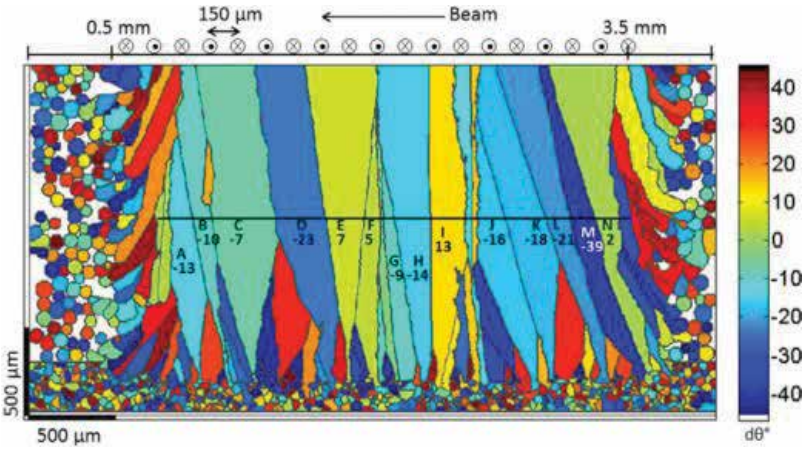


**Figure 18.** Simulated grain structure from Rai et al. [20]. The color bar maps grain misorientation with respect to the build direction.

and misorientation distribution. The grain size between two results is not similar because the thermal gradient and cooling rate are different between powder bed-based additive manufacturing and DMD process.

## 4. Conclusions

The transient temperature field of single-layer and multiple-layer deposition of Ti-6Al-4V was simulated with finite element method. The simulation result was validated by thermocouple experiment. The FE model provides the temperature at a relatively coarse scale (200 μm), and interpolation algorithm was used to scale the temperature field to match that of the CA model. The FE-CA model predicts grain morphology evolution as the deposition cools down. Hence, the instantaneous nucleation law, grain growth and crystallographic orientation were modeled in this study. It has been found that the developed "decentered polygon" growth method is more appropriate for the highly nonuniform temperature field, and the simulation result is closer to the real experimental measurement compared to the conventional growth method. For multilayer deposit, columnar grains dominated in the 25-layer deposition in the simulation. The grain size becomes larger when the position is closer to the top area of the deposition, which matches well with the optical microscopic result. The grain size of single and multiple layers between simulation and experiment is similar. It demonstrates that this FE-CA simulation can reasonably predict thermal history and grain morphology during this case of direct metal deposition.

## Acknowledgements

This work was funded through NASA's Fundamental Aeronautics Program, Fixed Wing Project, under NRA NNX11AI73A.

## Author details

Jingwei Zhang*, Lei Yan, Wei Li and Frank Liou

*Address all correspondence to: jnzzp5@mst.edu

Department of Mechanical Engineering, Missouri University of Science and Technology, Rolla, MO, United States

## References

[1] Rappaz M. Modelling of microstructure formation in solidification processes. International Materials Reviews. 1989;**34**(3):93-124

[2] Anderson M, Srolovitz D, Grest G, Sahni P. Computer simulation of grain growth—I. Kinetics. Acta Metallurgica. 1984;**32**(5):783-791

[3] Srolovitz DJ, Anderson MP, Sahni PS, Grest GS. Computer simulation of grain growth—II. Grain size distribution, topology, and local dynamics. Acta Metallurgica. 1984;**32**(5):793-802

[4] Saito Y, Enomoto M. Monte Carlo simulation of grain growth. ISIJ International. 1992; **32**(3):267-274

[5] Chen L-Q. Phase-field models for microstructure evolution. Annual Review of Materials Research. 2002;**32**:113-140

[6] Krill CE III, Chen L-Q. Computer simulation of 3-D grain growth using a phase-field model. Acta Materialia. 2002;**50**(12):3059-3075

[7] Böttger B, Eiken J, Steinbach I. Phase field simulation of equiaxed solidification in technical alloys. Acta Materialia. 2006;**54**(10):2697-2704

[8] Moelans N, Blanpain B, Wollants P. An introduction to phase-field modeling of microstructure evolution. Calphad. 2008;**32**(2):268-294

[9] Rappaz M, Gandin C-A. Probabilistic modelling of microstructure formation in solidification processes. Acta Metallurgica et Materialia. 1993;**41**(2):345-360

[10] Gandin C-A, Rappaz M. A coupled finite element-cellular automaton model for the prediction of dendritic grain structures in solidification processes. Acta Metallurgica et Materialia. 1994;**42**(7):2233-2246

[11] Gandin C-A, Desbiolles J-L, Rappaz M, Thevoz P. A three-dimensional cellular automation-finite element model for the prediction of solidification grain structures. Metallurgical and Materials Transactions A: Physical Metallurgy and Materials Science. 1999;**30**(12):3153-3165

[12] Choudhury A, Reuther K, Wesner E, August A, Nestler B, Rettenmayr M. Comparison of phase-field and cellular automaton models for dendritic solidification in Al–Cu alloy. Computational Materials Science. 2012;**55**:263-268

[13] Dore X. Modelling of microsegregation in ternary alloys: Application to the solidification of Al–Mg–Si. Acta Materialia. 2000;**48**:3951-3962

[14] Jarvis DJ, Brown SGR, Spittle JA. Modelling of non-equilibrium solidification in ternary alloys: Comparison of 1D, 2D, and 3D cellular automaton finite difference simulations. Materials Science and Technology. 2000;**16**(December):2-6

[15] Grujicic M, Cao G, Figliola RS. Computer simulations of the evolution of solidification microstructure in the LENS TM rapid fabrication process. Applied Surface Science. 2001;**183**:43-57

[16] Kelly SM, Kampe SL. Microstructural evolution in laser-deposited multilayer Ti-6Al-4V builds: Part II. Thermal modeling. Metallurgical and Materials Transactions A: Physical Metallurgy and Materials Science. 2004;**35**(6):1869-1879

[17] Kelly SM, Kampe SL. Microstructural evolution in laser-deposited multilayer Ti-6Al-4V builds: Part I. Microstructural characterization. Metallurgical and Materials Transactions A: Physical Metallurgy and Materials Science. 2004;**35**(6):1861-1867

[18] Nie P, Ojo OA, Li Z. Numerical modeling of microstructure evolution during laser additive manufacturing of a nickel-based superalloy. Acta Materialia. 2014;**77**(Supplement C): 85-95

[19] Rodgers TM, Madison JD, Tikare V, Maguire MC. Predicting mesoscale microstructural evolution in electron beam welding. JOM. 2016;**68**(5):1419-1426

[20] Rai A, Helmer H, Körner C. Simulation of grain structure evolution during powder bed based additive manufacturing. Additive Manufacturing. 2017;**13**(Supplement C):124-134

[21] Keller T, Lindwall G, Ghosh S, Ma L, Lane BM, Zhang F, Kattner UR, Lass EA, Heigel JC, Idell Y, Williams ME, Allen AJ, Guyer JE, Levine LE. Application of finite element, phase-field, and CALPHAD-based methods to additive manufacturing of Ni-based superalloys. Acta Materialia. 2017;**139**(Supplement C):244-253

[22] Guo S, Wang M, Zhao Z, Zhang YY, Lin X, Huang WD. Molecular dynamics simulation on the micro-structural evolution in heat-affected zone during the preparation of bulk metallic glasses with selective laser melting. Journal of Alloys and Compounds. 2017;**697**:443-449

[23] Militzer M. Phase field modeling of microstructure evolution in steels. Current Opinion in Solid State & Materials Science. 2011;**15**(3):106-115

[24] Wolf-Gladrow DA. Lattice-Gas Cellular Automata and Lattice Boltzmann Models. Springer Berlin Heidelberg; 2000

[25] Zhou JG. A lattice Boltzmann method for solute transport. International Journal for Numerical Methods in Fluids. 2009;**61**(8):848-863

[26] Rai A, Markl M, Körner C. A coupled Cellular Automaton–Lattice Boltzmann model for grain structure simulation during additive manufacturing. Computational Materials Science. 2016;**124**:37-48

[27] Yin H, Felicelli SD, Wang L. Simulation of a dendritic microstructure with the lattice Boltzmann and cellular automaton methods. Acta Materialia. 2011;**59**(8):3124-3136

[28] Lütjering G. Influence of processing on microstructure and mechanical properties of ($\alpha$+$\beta$) titanium alloys. Materials Science and Engineering A. 1998;**243**(1-2):32-45

[29] Reddy JN, Gartling DK. The Finite Element Method in Heat Transfer and Fluid Dynamics. New York: CRC Press; 2010. p. 39

[30] Andrews LC, Phillips RL. Laser Beam Propagation through Random Media. London: SPIE Publications; 2005. pp. 121-123

[31] Alimardani M, Toyserkani E, Huissoon JP. A 3D dynamic numerical approach for temperature and thermal stress distributions in multilayer laser solid freeform fabrication process. Optics and Lasers in Engineering. 2007;**45**(12):1115-1130

[32] Lampa C, Kaplan AFH, Powell J, Magnusson C. An analytical thermodynamic model of laser welding. Journal of Physics D: Applied Physics. 1997;**30**(9):1293

[33] Liu H, Sparks T. Modeling and verification of temperature distribution and residual stress in laser aided metal deposition process. Proceedings of the 6th Annual ISC Graduate Research Symposium. 2012;(1):1-7

[34] Oldfield W. A quantitative approach to casting solidification: Freezing of cast iron. Transactions of American Society for Metals. 1966;**59**:945

[35] Fisher DJ, Kurz W. Appendix 7 and 8, Fundamentals of Solidification. Aedermannsdorf: Trans Tech Publication Ltd; 1992. pp. 226-246

[36] Fisher DJ, Kurz W. Appendix 9, Fundamentals of Solidification. Aedermannsdorf: Trans Tech Publication; 1992. pp. 247-260

[37] Chen R, Xu Q, Liu B. A modified cellular automaton model for the quantitative prediction of equiaxed and columnar dendritic growth. Journal of Materials Science and Technology. 2014;**30**(12):1311-1320

Chapter 3

# Modeling of the Plasma 3D Deposition of Wire Materials

Dmitriy Trushnikov, Oleg Smetannikov,
Anatoly Perminov, Shengyong Pang,
Karuppasamy Poolan Karunakaran, Petr Maksimov,
Mariia Bartolomey, Aleksei Kovyazin,
Vladimir Belenkiy and Yurii Schitsyn

Additional information is available at the end of the chapter

http://dx.doi.org/10.5772/intechopen.77153

**Abstract**

The numerical modeling of the physical process of manufacturing parts using additive technologies is complex and needs to consider a variety of thermomechanical behavior. This is connected with the extensive use of the finite element computer simulation by means of specialized software packages that implement mathematical models of the processes. The algorithm of calculation of nonstationary temperature fields and stress-strain state of the structure during the process of 3D deposition of wire materials developed and implemented in ANSYS is considered in the paper. The verification of the developed numerical algorithm for solving three-dimensional problem of the production of metal products using arc 3D deposition of wire materials with the results of the experiment is carried out. The data obtained from calculations on the developed numerical model are in good agreement with the experiment.

**Keywords:** wire deposition, thermomechanical behavior, additive technologies

## 1. Introduction

Additive technologies are a breakthrough solution of this century. At the same time, when we speak about additive technologies, we generally mean the manufacturing of products of small sizes and irregular shapes. Large-sized products are still characterized by the use of traditional casting and forging shops. If mass production, such as the motor vehicle industry, is generally

satisfied with traditional solutions, then small-scale manufacturing, such as the aircraft industry, requires a more advanced approach. A manufacturing cycle of relatively simple and large-sized products, such as longerons, frame elements, etc., may in certain cases take 2 years at a cost of 1.2 million dollars. The situation at hand is one of those reasons which result in unreasonably long terms and high costs of creation and introduction of new products to the market.

The use of powder additive technologies sometimes gives rise to problems associated with low productivity of existing methods, high costs of equipment being used, limited types of materials, which is caused by the fact that powder systems melted by a powerful thermal source [1–3] are traditionally used as initial materials for additive formation of products. The formation of products from many aluminum alloys and active metal alloys, such as titanic and magnesium alloys, leads to increased porosity of materials of resulted products with considerably decreased mechanical properties [4–7]. The productivity of formation of components from powder materials in traditional additive technologies is extremely low, which practically excludes any prospects of the use of these technologies for the purpose of manufacturing large-sized products.

Hybrid manufacturing technologies combine the best characteristics of additive formation of workpieces and those of subsequent mechanical removal of materials in the course of creation of metal products [8, 9]. This process can be implemented on one platform with the hybrid layer-by-layer application of wire materials and the processing by CNC machines and is an optimum solution for the manufacturing of large-sized components of molds of low and average complexity.

One of the first companies that is engaged in promoting wire material-related technologies is Sciaky (USA) [1, 2] that specializes in the development of electron-beam welding technologies and equipment. Additive manufacturing machines made by Sciaky produce components with the use of the layer-by-layer build-up welding method for materials in melts created by an electronic beam. This technology is known as EBDM (Electron Beam Direct Manufacturing). High performance levels (3–9 kg/h) demonstrated by the EBDM technology allow us to prepare components whose sizes are expressed in meters, which is impossible or extremely expensive when using any other additive technologies. This component formation principle is responsible for a low-quality surface of a synthesized component. However, the EBDM technology combined with traditional machining technologies allows us to obtain results with acceptable costs. Model materials used in this technology are additions (metal bars or wires), which is also an advantage as there are many available materials of this kind: nickel alloys, stainless and instrument steels, Co-Cr alloys and many others whose prices are considerably lower than those of these materials in their powdered condition [1]. Today, the company does not make standard machines and is generally involved in producing basic Sciaky's DM models with the sizes of a formation zone of 5700 × 1200 × 1200 mm, and all modifications are created according to customer requirements. Machines allow to consistently form up to 10 various components in automatic mode and during one vacuumization cycle of a working chamber. The price of one machine is more than $2.0 million.

The use of arc and plasma sources for the purpose of melting metal wire materials in the course of implementation of hybrid additive manufacturing technologies has been actively developed

in recent years. In 2016, Norsk Titanium, a Norwegian start-up, attracted additional investments of 25 million dollars in order to certify materials resulted from the plasma layer-by-layer deposition with titanium wire and used to produce components for Boeing and Airbus aircrafts. It is also necessary to mention a company called WAAM (at Cranfield University) that is engaged in developing large-sized product formation technologies with the use of plasma technologies or consumable electrode surface welding processes with impulsive wire feeds and cold metal transfers (CMT) developed by Fronius. In the middle of 2016, Europe witnessed a 3-year LASSIM project with a budget of about 5 million euros that united 16 companies. The purpose of this project is to create a stand in order to implement several processes within a single space in the course of hybrid manufacturing of large-sized workpieces: additive manufacturing; multi-coordinate machining; layer-by-layer work hardening, measurement; non-destructive testing.

When modeling heat and mass transfer processes, it is necessary to consider that additive technologies are technologically closest to multi-layer deposition that also makes an initial material (filler wire) interact with a heat source, gradually builds up layers and superposes thermal cycles as and when new layers are added and transitional changes occur in the geometry. Temperature fields in a product to be processed are in most cases difficult to determine with the use of experimental methods. The most frequently used temperature measurement method consists in placing thermocouples directly next to the area of influence by a thermal source [10–13]. Thermocouples can measure temperatures only in places where they are installed, and it is difficult to have a general picture of temperature distribution even when several thermocouples are used. Infrared thermography [14–17] can measure only surface temperatures and cannot ensure the distribution of transient temperature processes in volume. The volume distribution of temperatures in a workpiece can be determined by mathematical modeling. However, the modeling of three-dimensional temperature fields is a rather demanding and complex problem due to accompanying difficult physical processes, their velocities, and many previously made calculations are connected with simplifications [18–21].

In order to model heat and mass transfer processes, we usually use the following equation system: mass, momentum and energy conservation equations [22–25]. Solutions of these equations allow us to obtain temperature fields in all projections of a sample to be formed, melt flow rates, cooling rates and crystallization parameters that specify structures and properties of components. At the same time, information on computational temperature fields obtained by using adequate models allows us to predict microstructures and properties of workpieces resulted from different additive manufacturing methods.

The process of manufacturing of components with the use of the additive manufacturing method is followed by complex thermo-mechanical phenomena resulting in the formation of technological residual stresses and possible contraction of components [26–33]. The appearance of internal stresses in an object to be produced is connected with the essential spatiotemporal heterogeneous distribution of temperature and conversion fields.

A standard approach to the numerical solution of temperature deformations and residual stresses in additive manufacturing is to systematically and consistently analyze thermal conductivity in a transient mode and elastoplastic deformations [34]. Further, a transient heat

conduction problem is firstly solved in a numerical manner; then, a temperature field is imported to a mechanical model as "thermal loads" in order to calculate stresses and deformations.

In case of additive technologies with a rather small number of deposition passes, it is acceptable to thoroughly model each pass in the course of production of components [35, 36]. With this modeling method, the supply of heat brought by a thermal source is generally used as a volume thermal flow whose center moves along a deposition trajectory, thereby representing a moving source of heat. However, the additive formation of products usually has a large number of layers, which makes it unreasonable to model each separate pass in the course of creation of components. In order to make calculations more effective, we use a principle where successive melting steps and even layers are grouped together for subsequent simultaneous activation [37, 38]. This method provides that a stationary thermal flow is assigned to a discrete area for a period of time specified by users. It is obvious that the way of building-up of materials and of application of thermal loads in an individual manner is more correct, but requires higher computational efforts.

Therefore, the possibility of modeling of technological processes related to the layer-by-layer synthesis of products by multi-layer deposition of wire materials is a considerable reserve for the purposes of optimizing technological modes of production of components, developing control programs, minimizing defects and increasing manufacturing quality. At the same time, a lot of works are aimed at modeling selective laser melting or laser gas powder deposition welding processes. The modeling of arc methods of deposition welding of wire materials has specific features connected with a large volume of materials to be deposited and, as a result, with great possible deformations of products, as well as with specific aspects of the description of a thermal source [39].

General variable parameters for mathematical models of heat and mass transfer processes with deposition welding with wire materials are as follows:

1. distribution of density of an energy flow of a heat source;
2. initial temperature of a sample;
3. distribution of an additional volume source (in case of additional induction heating);
4. dependence of thermophysical characteristics of materials on temperature;
5. characteristics of phase transitions;
6. velocity of a heat source;
7. orientation and feed rate of wire and its diameter.

As a part of the mathematical models described below, the following assumptions have been accepted:

1. In the process in question, the strength of a plasma arc, the feed rates of a support material $V_H$ and wire $V_П$ are constant or time intervals of their change considerably exceed a typical time of relaxation of temperature, velocity and concentration fields.

2. The ambient temperature is constant.
3. An energy source is characterized by Gaussian distribution of a thermal flow onto surfaces of a support material and a bed to be deposited.
4. Support and wire materials have the same chemical composition.
5. Molten metal is considered to be an incompressible Newtonian liquid whose physical parameters (density, viscosity, thermal conductivity, etc.) do not depend on temperature.
6. When describing thermal effects in the course of melting and hardening of materials, effective thermal capacity within a quasi-equilibrium model is used.
7. In order to describe the influence of a two-phase zone on the motion of a melt, Darcy term, representing the damping force when fluid passes through a porous media dendrite structures, is introduced to the motion equation [41].
8. An impact on the motion of a melt of electric and magnetic fields generated by a plasma flow is not considered.

Filler wires are fed into the zone of influence of a plasma arc, thereby causing a mass inflow. A plasma arc causes melting and evaporation of a filler material and a base material. The surface of a melt can be somehow deformed under the influence of the arc pressure, of falling droplets (when melting a wire) or of a local increase in metal vapors pressure.

Technological process parameters affect the nature of a metal transfer to a melt. We can distinguish three typical modes:

1. Continuous metal transfer (**Figure 1a**). This mode is carried out at a low strength of a thermal source and is rather low-temperature. This mode slightly changes sizes and a

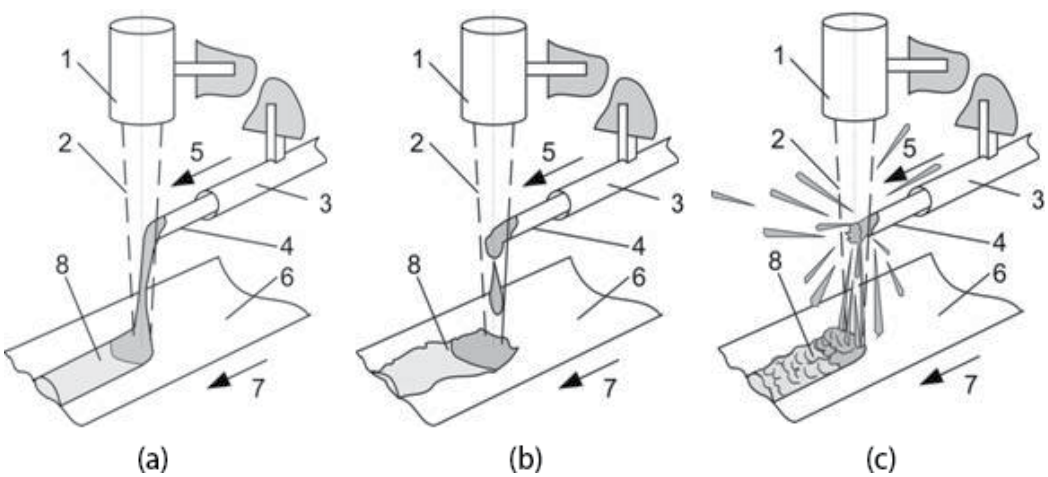


**Figure 1.** Schematically illustrated modes of a mass transfer of a filler material to a melt [40]. *a*—Continuous metal transfer, *b*—coarse-droplet transfer and *c*—spray transfer. *1*—Plasmotron; *2*—plasma arc; *3*—feeder; *4*—wire; *5*—wire feed direction; *6*—product; *7*—product motion direction; *8*—weld bed being formed.

form of cross section of a weld bed, as well as a structure and physical and mechanical properties of a metal to be deposited. This regime is optimal for the additive process. But their change may be caused only by disturbing factors (instable strength and position of a thermal source, deviation of a wire feed rate or displacement of a product, as well as influence of reheating zones). These factors are not considered at the current stage of works. A further decrease in energy to be delivered results in the fact that wires are melted only partially. This gives rise to formation defects and, therefore, this mode is not satisfactory.

2. A coarse-droplet transfer (**Figure 1b**) takes place when strength is increased above some critical value. The form of a weld bed and its cross dimensions range in length, metal splashes are present, and a crystallization process cannot be considered as a stationary one. This transfer mode may be acceptable for the consumable electrode welding technology. However, its use in most cases results in decreased quality when additive shape-forming processes are implemented.

3. A spray transfer (**Figure 1c**) is carried out in a mode with a higher energy of a thermal source. Metals being constantly fed experience a thermal influence sufficient for strong boiling. This mode is characterized by high spraying and uneven surfaces of weld beds to be formed.

## 2. Mathematical statements of problems (models) of a heat and mass transfer in the course of additive formation of products by melting of wire materials with a plasma arc

The geometry of a computational domain of the model in question is presented in a three-dimensional arrangement (**Figure 2**) and in the X-Z section (**Figure 3**). A surface source of a mass to be deposited onto a solid support material is fed to an interface at the velocity of $V_П$ with some distribution in the X, Y plane (in case of a droplet transfer approximation is possible by Gaussian distribution). A thermal flow from an energy source is determined by Gaussian normal distribution. A minimum temperature in a source is supposed to be higher than the solidus temperature (TS). A mass source moves along a solid support material at the velocity of $V_Н$ (deposition welding velocity). There is the air above a solid support material.

This problem is supposed to be tackled by the shock-capturing method where motion and temperature distribution equations are solved within the whole domain presented in **Figure 2**. In order to describe the motion of a material interface, the level set method is used. The position of an interface and values of material parameters of media (density, viscosity, thermal conductivity, thermal capacity) are determined according to a value of a special remote function $\phi$, to which a separate equation is assigned. The level set method helps to determine an interface position between a metal (a molten metal) and the air. The position of a boundary of a phase transition between a solid metal and a melt is established according to a position of an isotherm corresponding to a melting temperature.

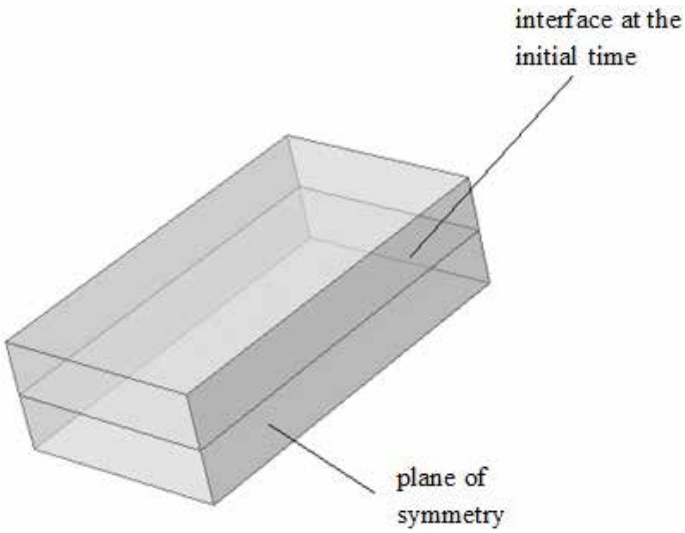


**Figure 2.** Geometry of the computational domain.

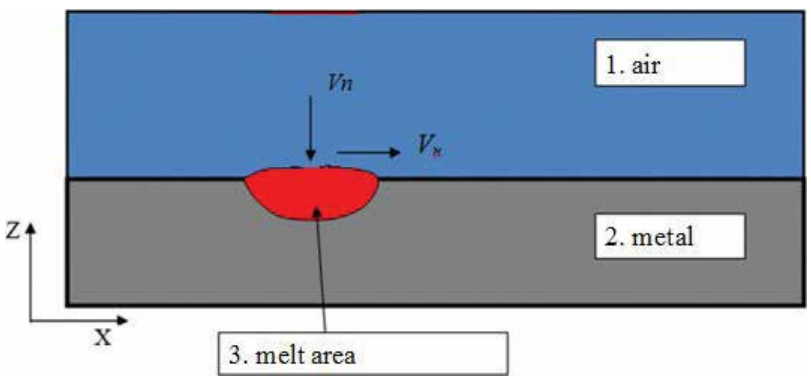


**Figure 3.** Symmetric longitudinal section of the computational domain.

Courses in metal and in air are described by free thermal convection equations for incompressible media in Boussinesq approximation [42]:

$$\frac{\partial}{\partial t}\left(\rho\,\vec{u}\right)+\left(\vec{u}\,\nabla\right)\left(\rho\,\vec{u}\right)=-\nabla P+\mathrm{Div}\overline{\overline{\tau}}+\vec{F}$$

$$\mathrm{div}\,\vec{u}=0$$

$$\tau_{ij}=\mu\left(\frac{\partial u_i}{\partial x_j}+\frac{\partial u_j}{\partial x_i}\right). \tag{1}$$

where $\rho$—density, $\vec{u}$—melt flow velocity vector, $\mu$—dynamic viscosity, $P$—pressure, $\vec{F}$—total volume force being as follows:

$$\vec{F} = \rho\,\vec{g}\,\beta(T - T_{ref}) - C\left(\frac{1-f_L}{f_L^3 + B}\right)\vec{u} + \vec{F}_{sv}, \tag{2}$$

where $g$—gravitational acceleration, $\beta$—thermal-expansion coefficient, $T$—absolute temperature, $T_{ref}$—initial temperature taken as the solidus temperature ($T_S$).

The first equation member (2) represents thermo-gravitational convection, the second one does energy dissipation of in a two-phase zone (in the zone of a phase transition from a melt to a solid metal), according to the Kozeny-Carman equation where $B$—a small computational constant used to avoid division by zero, C—a constant reflecting the morphology of a two-phase zone (in these studies it is possible to use values around $10^4$ … $10^6$), $f_L$—a function determining the position of a boundary between a liquid phase and a solid one in a metal (fusion zone boundary) [39]:

$$f_L = \begin{cases} 1 & T > T_L \\ (T - T_S)/(T_L - T_S) & T_S \le T \le T_L \\ 0 & T < T_S \end{cases} \tag{3}$$

where $T_L$ and $T_S$—liquidus temperature and solidus temperature.

The third equation member (2) $\vec{F}_{sv}$ is a volume approximation of forces acting at the boundary of a phase interface.

The thermal energy distribution in the computational domain is described by means of the differential energy transfer equation:

$$\frac{\partial T}{\partial t} + \left(\vec{u}\,\nabla\right)T = a \cdot \left(\frac{\partial^2 T}{\partial x^2} + \frac{\partial^2 T}{\partial y^2} + \frac{\partial^2 T}{\partial z^2}\right) + \frac{Q}{c\rho} \tag{4}$$

where $T$—absolute temperature, $a = \lambda / C_{eff} \cdot \rho$—thermal diffusivity coefficient, $u$—melt flow rate, $c$—thermal capacity, $\rho$—density.

The approach in question provides that the location of a welding source of heat and a source of mass at the "metal-gas environment" interface are arbitrary functions of time. Besides, it is necessary to consider that a wire material is fed to the "metal-gas environment" interface in an already melted state, which also requires some part of energy [43]. In an approximation that the temperature of a melted wire material to be fed is equal to the temperature of a melt at the interface, thermal capacity Q to be brought in the Eq. (4) is expressed as follows:

$$Q = \left(q_r - q_p - q_h(T - T_0) - \sigma_{c\delta}\varepsilon_{ч}\left(T^4 - T_0^4\right)\right)\delta(\phi)n_z,$$

$$q_r = \eta_0 \frac{2Q_0}{\pi r^2} \exp\left(\frac{-2\left((x - V_{и}t)^2 + y^2\right)}{r^2}\right) \tag{5}$$

$$q_p = \begin{cases} F_p\rho_L\left[C_{pS}(T_L - T_0) + L_m + C_{pL}(T - T_L)\right], & T > T_L \\ F_p\rho_L\left[C_{pS}(T_L - T_0) + L_m f_L - (1 - f_L)L_m\right], & T_S \le T \le T_L \\ F_p\rho_S\left[C_{pS}(T - T_0) - L_m - C_{pS}(T_S - T)\right], & T < T_S \end{cases}$$

$$F_p = N_S(r)V_n$$

where $Q_0$—maximum thermal power in a source, $r$—radius of a thermal spot from a source, $\eta_0$—efficiency of a heat source, $q_h$—thermal flow coefficient determined by a convective current, $\sigma_{c\delta}$—Stefan-Boltzmann constant, $\varepsilon_ч$—metal blackness degree, $\rho_L$ and $\rho_S$—densities of a liquid phase and a solid one of a metal, $C_{pL}$ and $C_{pS}$—specific thermal capacities at a constant pressure of a liquid phase and a solid one of a metal, $L_m$—specific metal melting heat, $N_S(r)$—function determining the distribution of a material to be delivered to a deposition zone, to be determined by deposition conditions (see **Figure 3**), $\delta(\phi)$ and $n_z$—delta function and normal projection to the boundary of the metal-air interface in the direction of the Z axis setting the distribution of heat along the boundary of the metal-air interface, will be determined below as a part of the description of the level set method.

The latent melting and crystallization heat was taken into consideration by introducing the effective thermal capacity:

$$C_{eff} = C_0 + \frac{\exp\left[-((T - T_{melt})/(T_L - T_S))^2\right]}{\sqrt{\pi}(T_L - T_S)}H_f, \tag{6}$$

where $C_0$—thermal capacity depending on temperature, $H_f$—latent melting heat, $T_{melt}$—melting temperature that is taken as an average one within a range from the solidus temperature to the liquidus one.

When in transition across the boundary of the interface of a liquid phase and a solid one in a metal, viscosity, first of all, suddenly changes from some final value $\mu_L$ in a melt to an actually infinite value in a solid metal $\mu_S$. The value of viscosity in (2) was determined by means of function (4) as [44]:

$$\mu = \mu_L f_L + \mu_S(1 - f_L) \tag{7}$$

In calculations, $\mu_S$ will be final, but it will be such as $\mu_S >> \mu_L$, which will ensure the "freezing" of a liquid in a solid phase. Sudden changes in density, thermal diffusivity and thermal metal capacity when in transition across the boundary of a phase transition may be described in a similar way.

Surface forces are approximated as volume ones so that:

- volume force $F_{sv}$ is concentrated in a narrow transitional layer where density and viscosity gradients markedly differ from zero;
- direction $F_{sv}$ coincides with the direction of remote function gradient $\phi$;
- value $F_{sv}$ is proportional to the gradient of a remote function and the curvature of a surface;

- in a limiting case, when a transitional layer turns into a jump in typical parameters of a liquid, the consideration of this volume force leads to an ordinary dynamic condition on the surface of an interface.

Based on the mentioned assumptions, an expression for the volume force is written as:

$$\vec{F}_{sv} = -\left(\sigma k(\phi)\nabla\phi - \frac{\partial\sigma}{\partial T}\nabla_s T - p_\partial \vec{n}\right)\delta(\phi) \tag{8}$$

where $\phi$—marker function, $k(\phi)$—interface surface curvature,

$$k(\phi) = \text{div}\ \vec{n}, \quad \vec{n} = \frac{\nabla\phi}{|\nabla\phi|}, \qquad n_z = \frac{1}{|\nabla\phi|}\frac{\partial\phi}{\partial z} \tag{9}$$

$\delta(\phi)$—Dirac delta function, $\sigma$—melt surface tension coefficient.

The first addend in (8) describes capillary forces acting normally to the surface of the metal-air interface, the second addend describes thermo-capillary Marangoni forces acting tangentially to the surface where $\nabla_s T$—temperature gradient component tangential to a curved surface. The third addend specifies the pressure force of plasma arc [44]:

$$p_\partial = 2k_I I_a \exp\left(\frac{-2\left((x - V_u t)^2 + y^2\right)}{r^2}\right) \tag{10}$$

where $I_a$—arc current, $k_I$—electrodynamic constant.

In the level set method, the position of an interface boundary is determined by a zero value of a level set or remote function $\phi$. As for the remote function, we solve a transfer equation that will be as follows:

$$\frac{\partial\phi}{\partial t} + \left(F_p + \vec{n}\cdot\vec{u}\right)\cdot|\nabla\phi| = 0 \tag{11}$$

Density, viscosity or concentration values are restored according to the remote function. For example, in case of density we have:

$$\rho(\phi) = \rho_1 + (\rho_2 - \rho_1)H(\phi) \tag{12}$$

where $\rho_1$ и $\rho_2$—media density, $H(\phi)$—Heaviside function set by the following expression:

$$H(\phi) = \begin{cases} 0 & \text{if } \phi < 0, \quad air \\ \frac{1}{2} & \text{if } \phi = 0 \\ 1 & \text{if } \phi > 0, \quad \text{metall} \end{cases} \tag{13}$$

For numerical implementation, expression (13) is written as

$$H_\varepsilon(\phi) = \begin{cases} 0 & \text{if } \phi < -\varepsilon \\ \frac{1}{2}\left[1 + \frac{\phi}{\pi} - \frac{1}{\pi}\sin\left(\pi\phi/\varepsilon\right)\right] & \text{if } |\phi| \le \varepsilon \\ 1 & \text{if } \phi > \varepsilon \end{cases} \tag{14}$$

The delta function in expressions (5) and (8) is equal to

$$\delta(\phi) = H'_\varepsilon(\phi) = \frac{\partial}{\partial\phi} H_\varepsilon(\phi) \tag{15}$$

$$\delta(\phi) = \begin{cases} \frac{1}{2\varepsilon}\left[1 + \cos\left(\frac{\pi\phi}{\varepsilon}\right)\right] & \text{if} \quad |\phi| \le \varepsilon \\ 0 & \text{otherwise} \end{cases} \tag{16}$$

The thickness of a transitional layer between the phases is equal to $2\varepsilon$. It is usually supposed that $\varepsilon = \alpha\Delta x$ where $\Delta x$ is a distance between nodes of a spatial grid or a grid cell size around a boundary, $\alpha$ is an integer.

Far from a fusion zone, at all boundaries of the computational domain, except for an upper boundary, a media velocity is supposed to be equal to zero. At the upper boundary, pressure is supposed to be set. For the remote function, at all boundaries the normal derivative is supposed to be equal to zero. Thermal conditions at the boundaries of the computational domain are determined by external technological conditions, but for model calculations all boundaries may be considered to be thermally insulated.

## 3. Description of a thermal source when using a plasma arc at various polarity

When modeling heat and mass transfer processes with the use of a plasma arc as a thermal source, there is a factor concerning the description of a thermal source, especially when using a plasma arc with current reverse polarity. A heat transfer to a product, under the influence of a plasma direct arc, is carried out by two mechanisms: convection from a plasma spray (a plasma flow) and heat emission in discharge (electrode) spots. Work [45] establishes that at an identical current and under all other conditions being equal a heat input to a product, during the operation of a plasmatron with current reverse polarity, is 1.3… 1.6 times higher than with current direct polarity, which is explained by a higher arc voltage. Unlike a constricted arc of direct polarity, a constricted arc of reverse polarity is characterized by a thermal power distributed more uniformly along the surface of a product (**Figure 4**).

It should be noted that at plasma processing with a current of direct polarity values $d_{pf}$ and $d_{as}$ are proportional, and it is impossible to control their size separately. The diameter of a plasma flow $d_{pf}$ is actually determined by the diameter of a nozzle $d_{pf} \approx d_{\text{n}}$ [46]. The distribution of density of a full thermal flow at direct polarity deposition welding is described by Gaussian distribution.

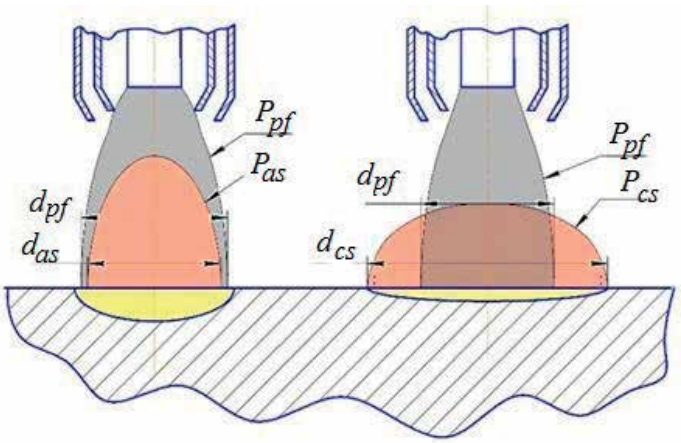


**Figure 4.** Chart of a heat transfer to a product at plasma processing. a—Current direct polarity, b—current reverse polarity. $P_{pf}$—Power delivered by convection by a plasma flow, $P_{as}$—power emitted at an anode spot, $P_{cs}$—power emitted in a cathode region, $d_{pf}$—diameter of a plasma flow, $d_{as}$—diameter of an anode spot, $d_{cs}$—diameter of a cathode region.

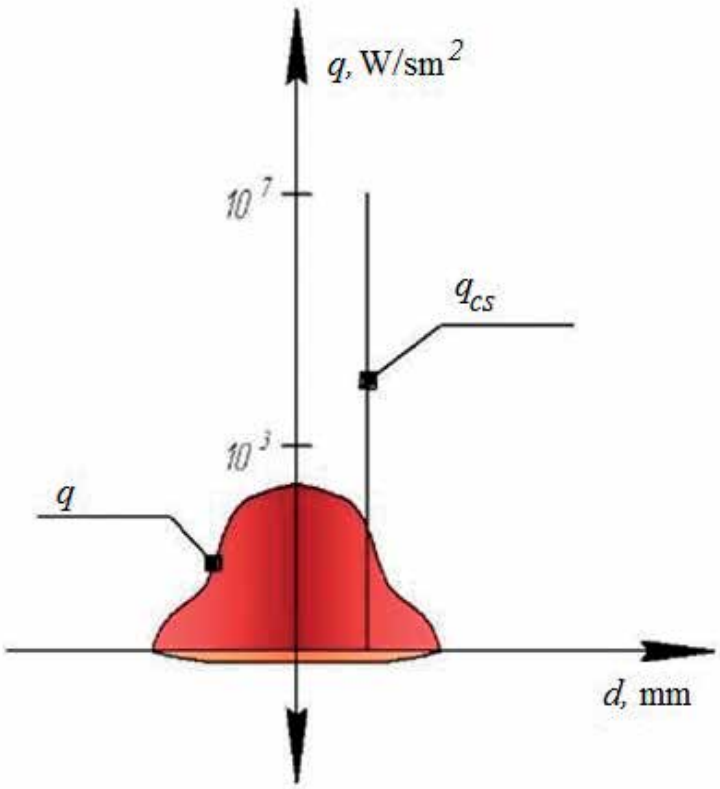


**Figure 5.** Aspects of a heat transfer to a product during the operation of a plasmotron with a current of reverse polarity. $q_{cs}$—Density of a thermal flow from a non-stationary cathode spot, $q$—density of a resulting thermal flow, $d$—diameter of the influence of a thermal flow, $h$—fusion depth of a base.

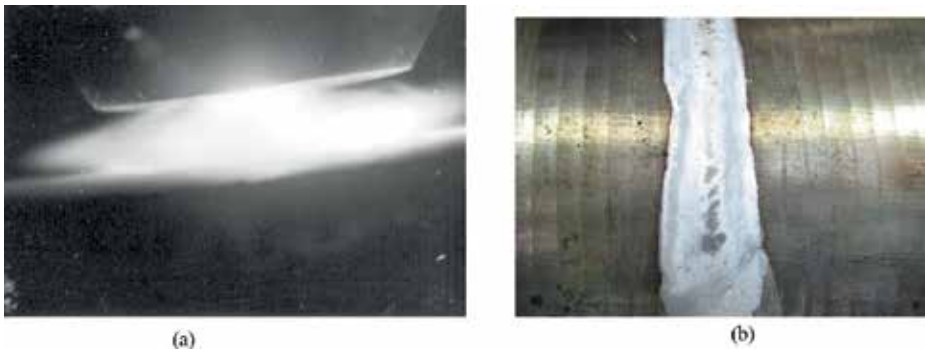


**Figure 6.** Traveling of cathode spots along a product surface during the operation of a reverse polarity plasmotron.

With current reverse polarity, a plasma arc belongs to a type of arcs with non-stationary cathode spots traveling along the surface of a cathode. A travel width depends on the design of a plasmatron and the material of a product. One of distinctive features of non-stationary spots is their short-term existence and high current density ($j \sim 10^5$–$10^6$ A/m$^2$), and local specific thermal flows in the area of short-term influence at a spot reach values ($q \sim 10^6$–$10^7$ W/cm$^2$) (**Figure 5**). The time-averaged thermal influence of cathode spots can be approximated evenly by a thermal source distributed along the area restricted to $d_{cs.}$ The distribution of density of a thermal flow delivered by a plasma flow at reverse polarity deposition welding is described by Gaussian distribution. The diameter of a plasma flow $d_{pf}$ is supposed to be the diameter of a nozzle $d_{cs} \approx d_{\text{n}}$ [46]. For the deposition of metal during the layer-wise formation, the following equipment which has been developed at Perm National Research Polytechnic University was used: the plasma welding unit BPS-350; universal plasmatron PM1-15.

A value $d_{cs}$ under the influence of an arc with current reverse polarity, can be actively controlled.

The size of a cathode region depends on parameters of a technological mode and requires determination. The travel of cathode spots leads to a known phenomenon of cathode cleaning under the influence of an electric arc of reverse polarity [47] on the surface of metals. It is generally believed [48] that the destruction and removal of an oxide film from a product surface in the area of influence of a reverse polarity arc result from attacking the surface of a metal by positive ions.

When a plasmatron operates with a reverse polarity current on a surface subjected to cathode cleaning, there is a visible mark [49] that allows us to visually estimate the area of traveling of cathode spots (**Figure 6**).

A phenomenon of cathode cleaning can be used to create a statistical dependence of the influence of technological parameters of reverse polarity plasma arcs on the diameter of a cathode region. At the first stage, it is possible to use an empirical model [48].

$$d_{cs} = 7,918 + 0,108I_a + 1,235Q_p + 1,235Q_{pg} - 0,238V - 0,599H, \tag{17}$$

where $I_a$—arc current, $Q_{pg}$—protective gas consumption (l/min), $Q_p$—plasma-forming gas consumption (l/min), $V$—plasmatron displacement speed, m/h, $H$—plasmatron nozzle height above a product (mm).

**Figure 7.** Geometry of the computational domain.

Therefore, a plasma source at reverse polarity deposition welding is represented by a combination of a source of heat delivered by a plasma flow with Gaussian distribution, of diameter $d_{pf}$, and an evenly distributed source of diameter $d_{cs}$. An energy ratio between these sources is determined experimentally according to the method suggested in the work [50].

In order to analyze the applicability of selected approaches, the preliminary numerical implementation in the two-dimensional statement of a problem of melting of wire materials with concentrated and arc energy sources was carried out. A Comsol 4.4 application software package (Heat Transfer, Level Set and Laminar Flow modules) was used. The geometry of the computational domain is presented in **Figure 7**.

The sizes of the computational domain are 50 mm (length) and 10 mm (height). A process simulation area was covered with a two-dimensional grid included in the computational domain. The grid had an even pitch. The size of a cell was 0.3 mm.

A 304-L stainless steel was accepted as a model material. The stainless steel workpiece had a composition of 18.2% Cr, 8.16% Ni, 1.71% Mn, 0.02% C, 0.082% N, 0.47% Mo, 0.44% Si, 0.14% Co, 0.35% Cu, 0.0004% S, 0.03% P, and balance Fe. Many thermophysical characteristics of materials are functions of temperature [51–54]. At this stage, these nonlinearities were not taken into consideration. **Table 1** specifies accepted values that were used in calculations. Parameters of the deposition welding mode presented in **Table 2**. As boundary conditions for a model example all boundaries, except for a lower one, were taken as thermally insulated. At the lower boundary, a constant temperature of 273 K was maintained.

**Figure 8** shows the distribution of temperature in a sample to be deposited 2 s later after the beginning of a process. A melt area is marked by a line.

| Attribute | Designation | Size | Value |
|---|---|---|---|
| Liquidus temperature | $T_S$ | [K] | 1723 |
| Solidus temperature | $T_L$ | [K] | 1673 |
| Specific heat capacity | $C$ | $[J \cdot kg^{-1} \cdot K^{-1}]$ | 500 |
| Density | $\rho$ | $[kg \cdot m^{-3}]$ | 7000 |
| Thermal conductivity | $\lambda$ | $[W \cdot m^{-1} \cdot K^{-1}]$ | 28.9 |
| Specific melting heat | $H_f$ | kJ/kg | 84 |

**Table 1.** Thermophysical characteristics of materials used in calculations [51–54].

| Source strength, W | Source displacement velocity, mm/s | Wire feed rate, mm/s |
|---|---|---|
| 800 | 5 | 15 |

**Table 2.** Deposition mode parameters.

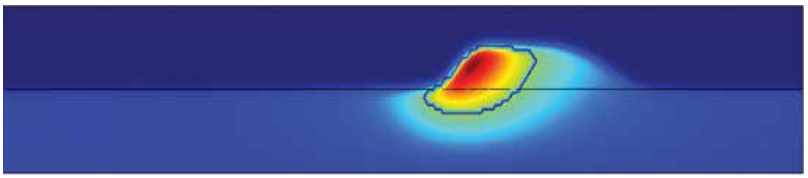

**Figure 8.** Distribution of temperature in the course of deposition welding.

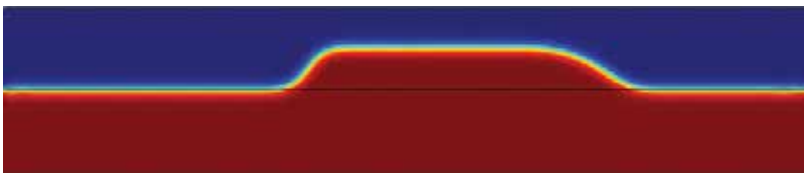

**Figure 9.** Weld bed formation results.

The deposition welding results obtained upon completion of a 4-s process are given in **Figure 9**. This model appropriately helps to determine distributions of temperatures, melt flow rates, pressures, components of heat flow densities, forms and sizes of weld beds to be deposited.

## 4. Development of the models intended to form fields of residual stresses and deformations in products resulted in the course of additive formation by melting wire materials with a plasma arc

The process of manufacturing of components with the use of the additive manufacturing method is followed by complex thermo-mechanical phenomena resulting in the formation of technological residual stresses and possible contraction of components [28, 30–32, 55–58]. The appearance of internal stresses in an object to be produced is connected with the essential spatiotemporal heterogeneous distribution of temperature and conversion fields. The appearance of residual stresses is caused due to the fact that inelastic deformations [33] are not consistent, first of all, temperature shrinkage deformations at cooling, structural shrinkage due to the course of phase transformations (melt crystallization) that is notable for a deformation history of various material points because of heterogeneous temperatures, temperature gradients and temperature velocities.

In most cases, such measures as preliminary natural validations of technologies, selection of certain locations of components, selection of technological modes, are taken in order to

eliminate and minimize any geometrical defects arising in the course of manufacturing of modern components, which is a serious obstacle to organizing comprehensive digital manufacturing processes.

An approach associated with creating and using mathematical and computer models of thermomechanical behaviors of components in the course of additive manufacturing allows us not to carry out natural experiments at a stage of design of technological process parameters and structural parameters and to predict qualitative and quantitative characteristics of stress conditions and contractions of future components, as well as study the effectiveness of possible measures aimed at decreasing residual stresses and deformations (heat treatment).

Calculation of residual stresses and warpage for the wire fusion process remains the most difficult aspect in numerical simulation. Often, the addition of material is modeled by adding and (or) activating new elements to previously placed ones. The growth of new elements adds additional rigidity to the existing structure and requires the gradual addition of more and more new elements to the solution area. There are three most commonly used methods of modeling material deposition—the so-called birth element (1), a quiet element (2) and hybrid activation (3) [59, 60]. In the method of the birth element, the elements for the material that has not yet been created are deactivated (and thus not included in the solution area), and then gradually regenerated and included in the solution area. In the method of sleeping elements, all elements are present in the calculation model from the very beginning and have artificial properties with very low rigidity. As the details grow, the properties of these elements gradually switch to real physical properties. Finally, the hybrid activation method combines the methods of emerging and sleeping elements, where only the current deposition layer is activated and set to a sleeping state, and all subsequent layers are deactivated [60].

For products with a relatively small number of surfacing passages, detailed modeling of each passage in the construction of a part is permissible [35, 36]. With this method of modeling, the heat input from the beam energy is usually applied as a volumetric heat flux whose center moves along the trajectory of surfacing, thus representing a moving heat source. Such a method with a moving heat source was used to model both Directed Energy Deposition (DED) [36] and Powder Bed Fusion (PBF) [35] additive production processes. Nevertheless, usually the product has a large number of layers, which makes it impractical to simulate each individual passage when creating a part. To ensure greater efficiency of calculations, the principle is used, in which the successive melting steps and even the layers are grouped together for subsequent simultaneous activation [37, 38].

We know studies aimed at modeling additive manufacturing processes, optimizing thermal cycles, estimating the influence of process parameters on changes in forms of finished products [59–80].

A large volume of research has been published for PBF from various materials, ranging from stainless steel [19, 63–65], carbon steels [78–80], nickel alloys [69–75] and titanium alloy Ti-6Al-4V [34, 69–72, 75, 76]. By modeling residual stresses and deformations for additive technologies using wire, much less work has been published than for powder systems. The normalized maximum residual stress is presented in [19, 64] as a function of the power, scanning speed,

and preheating of the substrate in the construction of a thin-walled structure. In [64] 3D sequential temperature and elastic calculations were performed using the COMSOL and MATLAB packages. In [65], a 3D sequential temperature and elastic-plastic analysis was performed in the SYSWELD package. In works [66, 67] the ABAQUS is used for sequential temperature and elastic-plastic 3D analysis, deformation due to a phase transition is taken into account. In [62, 73], the COMET program and element activation technology are used, a thermo-elasto-viscoplastic material model is used. Additive technology Wire Arc Additive Manufacturing (WAAM) is suitable for manufacturing parts that require a large amount of surfacing [69, 72, 77]. In [69–72] for WAAM technology in ABAQUS software, 3D analysis is performed, assuming the elastic-plastic behavior of the material.

To improve the efficiency of the calculations, Li et al. [78] proposed a method that displays the local residual stress field calculated at the mesoscale level for the rapid prediction of warping of a part. Another approach to efficient modeling warping is to use the inherent-strain method, developed by Yuan and Ueda to calculate the deformation in welding large-sized parts [79]. The method directly applies a known proper (initial) deformation to calculate buckling and does not require a numerical solution of non-stationary temperature and elastoplastic problems in a step-by-step formulation. Finally, Mukherjee et al. [71, 75] constructed an analytical expression for the special deformation parameter for estimating the maximum residual strains as a function of the linear heat release, substrate stiffness, maximum temperature, the thermal expansion coefficient of the fusion alloy and the Fourier number, which expresses the ratio between the speed changes in the thermal conditions in the environment and the speed of the adjustment of the temperature field inside the system under consideration.

The numerical modeling of residual stresses and thermoshrinkable deformations at additive formation of products with the use of wire materials melted by a plasma arc is considered below.

In view of small deformations and negligibly small dissipative heat emission, it is possible to divide a boundary problem of non-stationary thermal conductivity and a boundary problem of thermomechanics with regard to a stressed-deformed state that are unrelated in such statement. Death and birth technologies (Elements Birth and Death in ANSYS) with regard to material parts (originally absent in a model and then added in the course of deposition) can be used in order to solve them. At the same time, an area occupied by an already finished product is considered as a computational one. The continuous building-up of a material is carried out discretely, at each substage of calculation corresponding to the "birth" of a next subarea from "dead" elements, a boundary problem of heat conductivity and thermomechanics is solved, and a result of solution of a previous substage serves as initial conditions for a subsequent one.

At substage $k$, the statement of a boundary problem of non-stationary heat conductivity according to temperatures fields $T(\mathbf{x}, t)$ in area $V_k$ with boundary $S_k$, with accepted hypotheses taken into consideration, includes [81]:

Thermal conductivity equation:

$$\rho(\mathbf{x})c(\mathbf{x}, T)\frac{\partial T}{\partial t} = \mathrm{div}(\lambda(\mathbf{x}, T)\mathrm{grad}(T)) + \rho(\mathbf{x})\dot{q}(\mathbf{x}, t), \mathbf{x} \in V_k \tag{18}$$

where $c(\mathbf{x}, T)$, $\lambda(\mathbf{x}, T)$, $\rho(\mathbf{x})$—thermal capacity, thermal conductivity and density of an unevenly alloyed material, $\dot{q}(\mathbf{x}, t)$—specific strength of an external heat source.

Boundary conditions:

$$-\lambda(\mathbf{x}, \mathrm{T}) grad(T) \cdot \mathbf{n} = h(T) \cdot (T - T_c(t)) + \varepsilon\sigma_0(T)^4 + \int_{S_k} \frac{I_e}{r^2} \cos\theta dS_k, \quad \mathbf{x} \in S_k \tag{19}$$

where the first addend of a right part describes a convective heat transfer, and the second one —radiation (the Stefan-Boltzmann law); the third one—radiation from a plasmatron nozzle, $\varepsilon$—blackness coefficient, $\sigma_0$—Stefan-Boltzmann constant, $I_e$—source radiation capacity, $r$—distance between a surface point and a source, and $\theta$—angle that is formed by a surface normal directed to a source, $h(T)$—heat transfer coefficient, $T_c(t)$—ambient temperature, $\mathbf{n}$—external single normal to the boundary $S$ of a body being cooled.

Initial conditions:

$$T(\mathbf{x}, t_{0,k}) = T_{k-1}(\mathbf{x}), \mathbf{x} \in V_k \tag{20}$$

where $T(\mathbf{x}, t_{0,k})$—initial temperature distribution for substage $k$, $T_{k-1}(\mathbf{x})$—temperature determined at the end of a previous one.

These relations consider that an area of study $V_k = V_k^{liv} \cup V_k^{kil}$ remains invariable throughout a substage. Here $V_k^{liv}$ and $V_k^{kil}$ are used to mark zones occupied by "live" and "dead" elements respectively. At the same time, thermophysical properties of the material in the area of "dead" elements are subject to degradation:

$$c(\mathbf{x}), \mathbf{x} \in V_k^{kil} << c(\mathbf{x}, T), \mathbf{x} \in V_k^{liv}, \qquad \rho(\mathbf{x}), \mathbf{x} \in V_k^{kil} << \rho(\mathbf{x}, T), \mathbf{x} \in V_k^{liv},$$
$$\lambda(\mathbf{x}), \mathbf{x} \in V_k^{kil} >> \lambda(\mathbf{x}, T), \mathbf{x} \in V_k^{liv}.$$

An unrelated quasistatic boundary problem of mechanics of a deformable solid body, taking into account the insignificance of a contribution of mass forces at substage $k$, includes [82, 83]:

Equilibrium equations:

$$\mathrm{div}\, \widehat{\sigma} = 0, \mathbf{x} \in V_k \tag{21}$$

where $\widehat{\sigma}(\mathbf{x}, t)$—stress tensor;

Cauchy geometrical relations:

$$\widehat{\varepsilon} = \frac{1}{2}\left(\nabla\mathbf{u} + (\nabla\mathbf{u})^T\right), \mathbf{x} \in V_k \tag{22}$$

where $\mathbf{u}(\mathbf{x}, t)$—displacement vector, $\widehat{\varepsilon}(\mathbf{x}, t)$—total deformation tensor.

Displacement boundary conditions:

$$\mathbf{u} = \mathbf{U}, \mathbf{x} \in S_{u,k} \tag{23}$$

Stress boundary conditions:

$$\widehat{\sigma} \cdot \mathbf{n} = \mathbf{P}, \mathbf{x} \in S_{\sigma,k} \tag{24}$$

where $S_u$, $S_\sigma$—parts of a boundary border with set displacements and loads respectively.

Thermomechanical properties of the material in the area of "dead" elements exclude physical nonlinearity and are perfectly elastic with degraded values:

$$^4\widehat{C}(\mathbf{x}), \mathbf{x} \in V_k^{kil} << {}^4\widehat{C}(\mathbf{x}, T), \mathbf{x} \in V_k^{liv},$$

where $^4\widehat{C}$—the fourth-rank tensor of elastic constants of the material.

The general equation system of the deformable solid body mechanics boundary value problem includes constitutive relations as well. To describe the viscoelastoplastic behavior of the alloy under study, we used the Anand [84] model included to the list of ANSYS physical models. The model has the following form:

$$\widehat{\sigma} = {}^4\widehat{C} \cdot\cdot (\widehat{\varepsilon} - \widehat{\varepsilon}_T - \widehat{\varepsilon}_B) \tag{25}$$

$$\widehat{\varepsilon}_T(\mathbf{x}, t) = \widehat{E} \int_{T_0}^{T} \alpha(\mathbf{x}, T(\mathbf{x}, t)) dT \tag{26}$$

where $^4\widehat{C}$—the fourth-rank tensor of elastic constants of the material; $\widehat{\varepsilon}_e(\mathbf{x}, t) = \widehat{\varepsilon}(\mathbf{x}, t) - \widehat{\varepsilon}_T(\mathbf{x}, t) - \widehat{\varepsilon}_B(\mathbf{x}, t)$—the tensor of elastic deformations, $\widehat{\varepsilon}(\mathbf{x}, t)$—the tensor of total deformations; $\widehat{\varepsilon}_T(\mathbf{x}, t)$—the tensor of temperature deformations; $\widehat{\varepsilon}_B(\mathbf{x}, t)$—the tensor of viscous deformations; $\alpha(\mathbf{x}, T)$—the coefficient of temperature expansion of the material; $T_0$—the onset temperature of temperature deformation; $\widehat{E}$—the second-rank identity tensor. The viscous deformation rate is calculated according to the formula:

$$\dot{\widehat{\varepsilon}}_B(\mathbf{x}, t) = \dot{\varepsilon}_B(\mathbf{x}, t) \left( \frac{3}{2} \frac{\widehat{s}}{q} \right),$$

where $\widehat{s}(\mathbf{x}, t) = \widehat{\sigma}(\mathbf{x}, t) - \sigma(\mathbf{x}, t)\widehat{E}$—the stress deviator; $\sigma(\mathbf{x}, t) = \sigma_{kk}/3$—the average stress; $q$—the equivalent stress $q = \sqrt{\frac{3}{2}\widehat{s} : \widehat{s}}$ (the following symbol ":" means a scalar product, the symbol "··", set in earlier, means a tensorial product); $\dot{\varepsilon}_B = \sqrt{\frac{2}{3}\dot{\widehat{\varepsilon}}_B : \dot{\widehat{\varepsilon}}_B}$—the equivalent viscous deformation rate connected to the other parameters by the following formula:

$$\dot{\varepsilon}_B = A e^{-\frac{U}{RT}} \left[ \sinh\left( \xi \frac{\sigma}{S} \right) \right]^{\frac{1}{m}} \tag{27}$$

The model also includes the evolutionary equation:

$$\dot{S} = \left\{ h_0 (|B|)^a \frac{B}{|B|} \right\} \dot{\varepsilon}_B \tag{28}$$

The equation involves a possibility of work hardening and work softening. The designations are as follows:

$B = 1 - \frac{S}{S^*}$; $S^* = S_1 \left[\frac{\dot{\varepsilon}_B}{A} e^{\frac{U}{RT}}\right]^n$; $\sigma$—the stress intensity; $S$—the resistance to deformation (scalar function of hardening); $S^*$—the saturation value of the hardening function; $R$—the absolute gas constant; $U$—the activation energy; $T$—the absolute temperature; $A$, $a$, $m$, $n$, $h_0$, $\xi$, $S_1$—the empirical coefficients.

Taking into account behavior characteristics of the elements activated according to the technology used at ANSYS, the formulas (25) are transposed to the following form:

$$\widehat{\sigma} = {}^4\widehat{C} \cdot \cdot (\widehat{\varepsilon} - \widehat{\varepsilon}_T - \widehat{\varepsilon}_B - \widehat{\varepsilon}_{k-1}) \tag{29}$$

where $\widehat{\varepsilon}_{k-1}$—the total deformation calculated up to the end of $k-1$-th sub-step (the current status at the moment of activation of the element is its natural state).

As the setup of the mechanical problem (Eqs. (21)–(28)) imply, the ANSYS system of hypotheses does not include separation of the stress tensor into any components. The input of separate factors to the stress field generation is covered by the corresponding deformation types (see the formula (25)). At that, shrinkage due to phase transformation is covered by temperature deformation with the help of corresponding adjustment of the thermal coefficient of linear expansion within the solidus-liquidus interval.

The algorithm of calculations of temperature fields in numerical simulation of the plasma deposition process in the finite element ANSYS package stipulates performance of the following computational procedures:

1. To create the finite element model including volumes to be occupied by the product divided to separate horizontal layers as well as the platform—the basis with suitable thermal and physical properties.
2. To "kill" (the EKILL command) a part of the elements that are not involved in the real process of building up before its beginning.
3. In the cycle of layer building up beginning from the bottom layer:

   To define conditions of convective heat exchange at the upper boundary of the layer according to the formula (19).

   In the cycle of sub-steps of passing the deposition areas of the successive computational layer:

   To remove a part of the layer at its bottom boundary under the area of previously defined conditions of convective heat exchange where available.

   To activate (the EALIVE command) all elements of the $k$-th area.

   To heat a part of the area's elements distributed around the volume using a thermal energy source (see the formula (18)) for a time of plasma arc impact. $t_a$.

   To remove the heat source and wait for the holding time $t_{wi}$.

4. To wait until the system cools down completely (partially). Solution of a non-stationary problem with known boundary conditions for a thermo-mechanical model, all of whose elements are active.

The impact time of the plasma arc $t_a$, taking into account possible overlapping of plasmatron motion paths, is calculated according to the formula

$$t_a = \frac{S_s}{v_s \cdot ds} \tag{30}$$

where $S_s = \pi D_S^2/4$—the size of the spot, $v_s$—the movement speed of the plasmatron, $ds$—the distance between adjacent tracks.

The holding time $t_{w,k}$ for the $k$-th building up area is defined by the following expression:

$$t_{wi} = \frac{S_k}{ds \cdot v_s} \tag{31}$$

where $S_k$—the size of the area.

The specific capacity of heat emission on the surface of the heated spot of the deposited material is defined according to the following formula:

$$\tilde{W}_T = K \cdot W/S_s \tag{32}$$

where $W$—the capacity of the plasma arc, $K$—the heating fraction of the capacity.

The specific volumetric capacity of the heat source used in the Eq. (18) has the following form:

$$\dot{q} = \dot{q}_S \cdot S_k/V_k = \frac{W \cdot K}{S_s \cdot h_k} \tag{33}$$

where $V_k$—the volume of the deposited area, $h_k$—the thickness of the layer. Thickness of the deposited layer $h_k$ is defined on the basis of experimentally observed total height of the deposited part of the product and actual number of layers.

The discrete model of the computational domain is similar to the model of the heat conductivity problem above. Before calculation, the Solid279 heat element is replaced with Solid286, which uses displacements as the degrees of freedom, and thermomechanical properties are added. The algorithm is similar to that of Item 4.1.:

1. To "kill" (the EKILL command) a part of the elements that are not involved in the real process of building up before its beginning. To define boundary conditions in displacement (e.g. fixation along the cutting plane, vertical fixation in entrapment zones etc.).
2. In the cycle of layer building up beginning from the bottom layer:

   In the cycle of sub-steps of passing the deposition areas of the successive computational layer:

   To activate (the EALIVE command) all elements of the $k$-th area.

To implement temperatures, previously calculated for that moment of time, to the units of the model for the impact time of the ray $t_a$.

To implement temperatures, previously calculated for the end moment of the holding time, and hold for $t_{wi}$ seconds.

3. To read the temperature field for the period of partially cooldown of the system, to calculate SSS.

4. To implement the ambient temperature, to release the entrapment, to calculate SSS.

After that we performed preliminary verification of the mathematical model and numerical algorithm for solution of the three-dimensional problem of metal products manufacturing using plasma deposition of wire materials. For the reference we took the results of the experiment for wire deposition on a metal base using arc surfacing in shielding gases with a tungsten (nonconsumable) electrode as described in the Article [85]. **Figure 10a** shows the plate in question with the dimensions of 275 x 100 x 12 mm. We build up a metal rib with the length of 165 mm and the cross section showed in **Figure 10b** on the upper surface of the object.

The arc deposition process is performed in 2 steps. The first step involves preliminary heating of the base plate that is performed by torch back and forth movement with the speed of $v_s = 5$ mm/s and the impacted area that is 1.5 times larger than the base area of the deposited rib. Power consumption of the torch is $W = 2.7$ kW, diameter of the spot is $D_s = 6$ mm. Subsequent deposition is performed in 10 layers along a continuous path (the process continues backward).

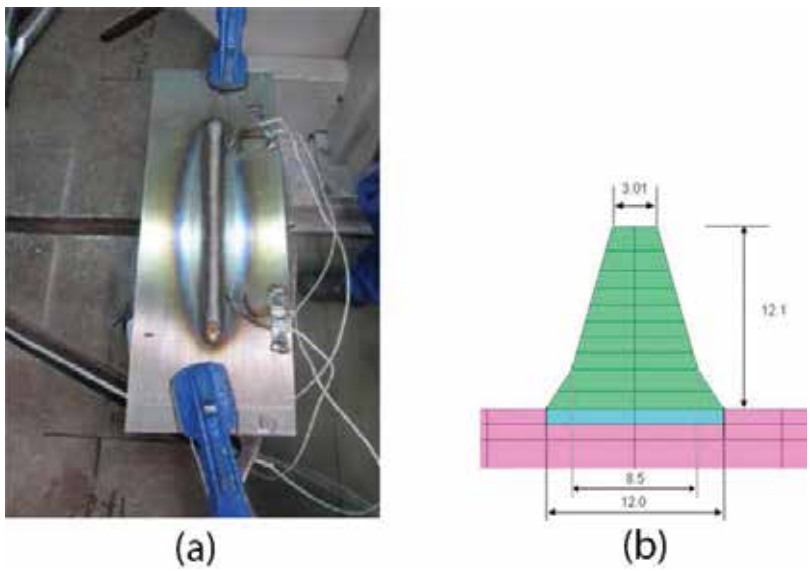


**Figure 10.** Product view illustration after the experiment with fixation and sensor systems (a), dimensions of the deposited area at the cross section, mm (b) [85].

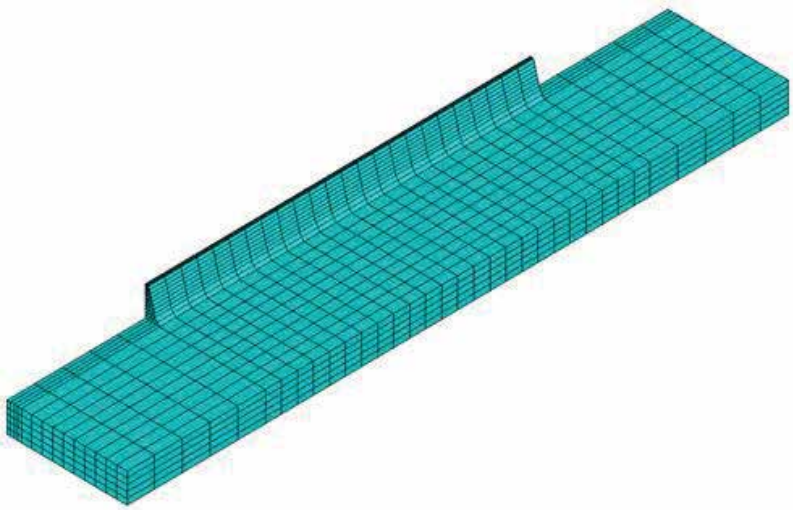

**Figure 11.** The discrete model of the building up problem.

**Figure 11** shows the finite element model of the problem. 20-unit isoparametric Solid 279 elements were used for solution.

The Inconel 718 nickel alloy was used as the material for calculation [86].

Thermal and physical properties of the material were taken from the Article [87]. In addition to the above, according to the data, represented in the Article, the density $\rho = 8170$ kg/m$^3$ and thermal conductivity $\lambda = 30$ W/(m K) were deemed as constants. Temperature dependence of the enthalpy $H(T)$ is presented in **Figure 12**. Heat capacity of the material, included in the thermal conductivity equation, was calculated according to the formula $c(T) = dH(T)/dT$. It should be noted that variations at the arc $H(T)$ in the range of 1500–1600 K in **Figure 12** arise from heat emission during solidification of the alloy. Heating fraction of the plasma arc capacity $K$ was set to 0.2 for calculation.

Identification of the chosen Anand model (25)–(28) for the material under study was performed according to the data of the stretch experiment with the defined speed at different temperatures represented in the Article [87].

The required constants of the model were defined in several steps by the downhill simplex method in the Matlab package. At that, relative disparity of computational and experimental values of voltage in Diagram $\sigma - \varepsilon$ (**Figure 13**) was minimized.

As the result, the following values of material constants were obtained by the authors of this publication:

$S_0$ = 2.0447e + 05 Pa, $U/R$ = 2.0864e + 03, $\xi$ = 0.3335, $A$ = 2.5008e + 04, $m$ = 0.4363, $h_0$ = 4.0352e + 06, $S_1$ = 3.2148e + 07 Pa, $n$ = 0.2273, $a$ = 0.4461.

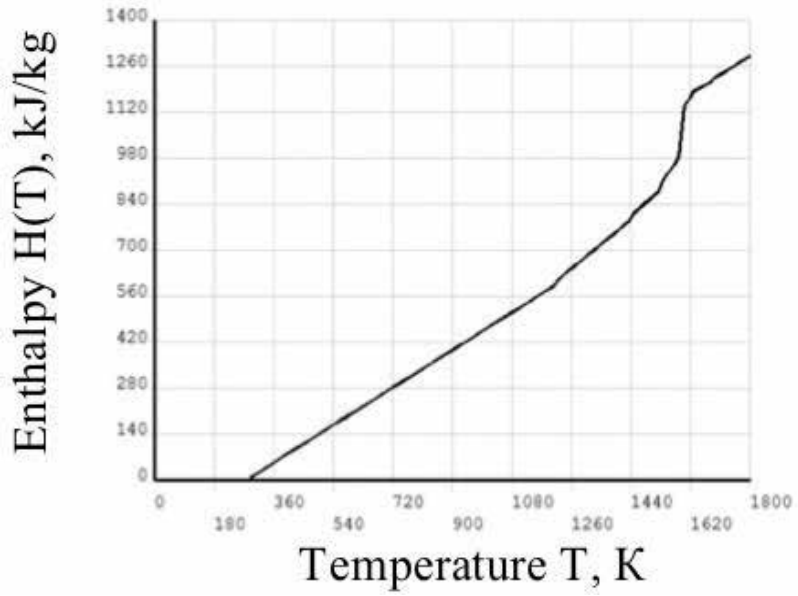


**Figure 12.** Dependence of the enthalpy H(T), kJ/kg, from the temperature T, K, for the alloy Inconel 718.

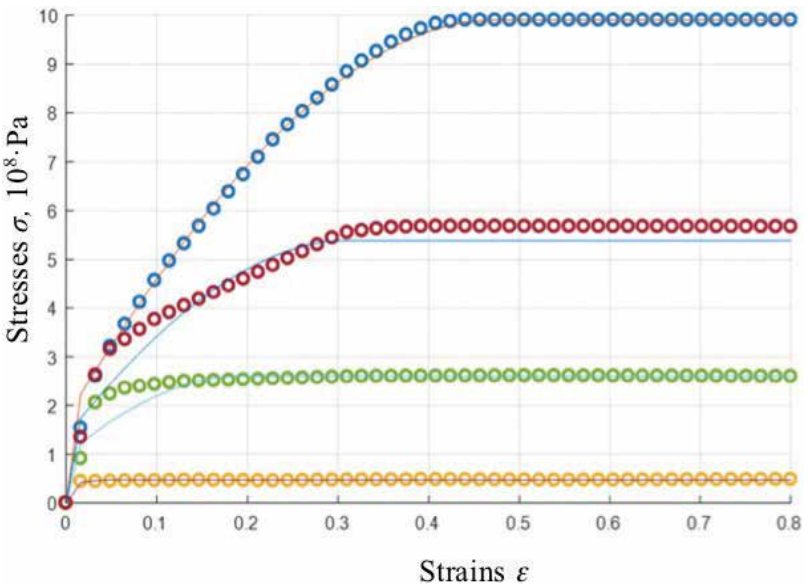


**Figure 13.** Comparison of experimental (dots) and computational values of voltage in unconfined stretch tests at the temperatures of 720, 850, 900, 1150°C (top-down).

Figure 13 shows that relative error of the calculation does not exceed 10%. The material was considered as isotropic. The Young's modulus of elasticity and the Poisson ratio were equal to 153 GPa and 0.32 respectively and not dependent on temperature [80]. The average value of

CLTE at the temperature range up to the solidus temperature $\alpha$ is $6.5 \times 10^{-6}$ $K^{-1}$. The lineal shrinkage on the interval between solidus and liquidus temperatures is 0.3% and included in the temperature dependence $\alpha(T)$. Hardening and softening effects, accompanying the building up process, are included into the Anand model.

The main results of the calculations were given in [88]. Verification was performed using the experimental results obtained in the paper [86, 87]. **Figure 14** shows the layout of temperature sensors in the investigational studies mentioned above.

In this case sensors No. 2, 3, 5, 6 were placed on the upper surface of the base plate, and No. 1 and 4 were placed on its bottom surface. Initial direction of the torch movement is from right to left. **Figures 15–17** show graphs of temperature evolution at the given points.

The figures show that the qualitatively retrieved data comply with the experiment. The worst quantitative match is observed at points on the down plane of the base close to the heating area (points 1 and 4, **Figure 15**). In addition, the curves have oscillations and the temperature is below the ambient temperature at some points. All in all, the experimental graphs are below the computational graphs. The oscillations can be explained by proximity of the heating area and, consequently, heavy temperature gradients substantially altering the result at a fairly coarse mesh. Higher heating level in the experiment may be also caused by failure to take account of the torch heat radiation expanded far beyond the computational size of the spot.

Precision of the computational data is substantially higher at other measurement points (**Figures 16** and **17**). The maximum absolute disparity does not exceed 25°C.

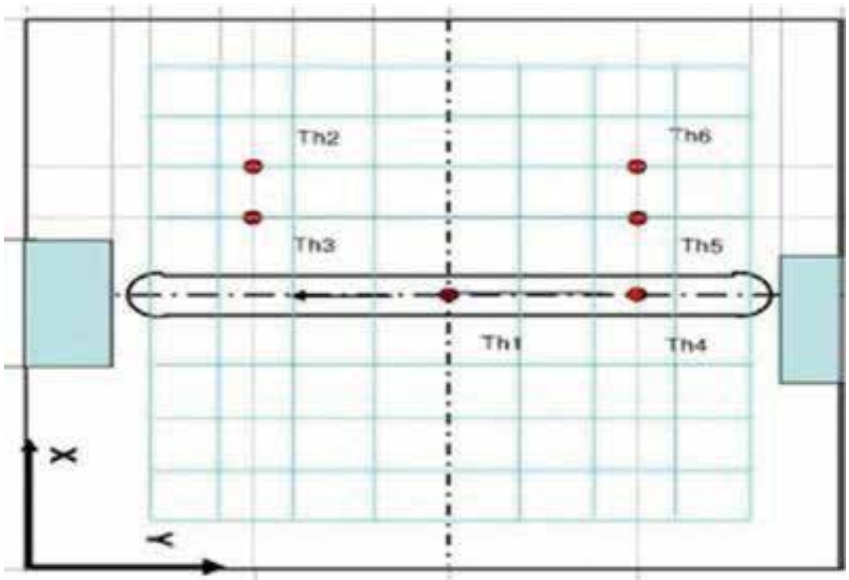


**Figure 14.** The layout of temperature sensors.

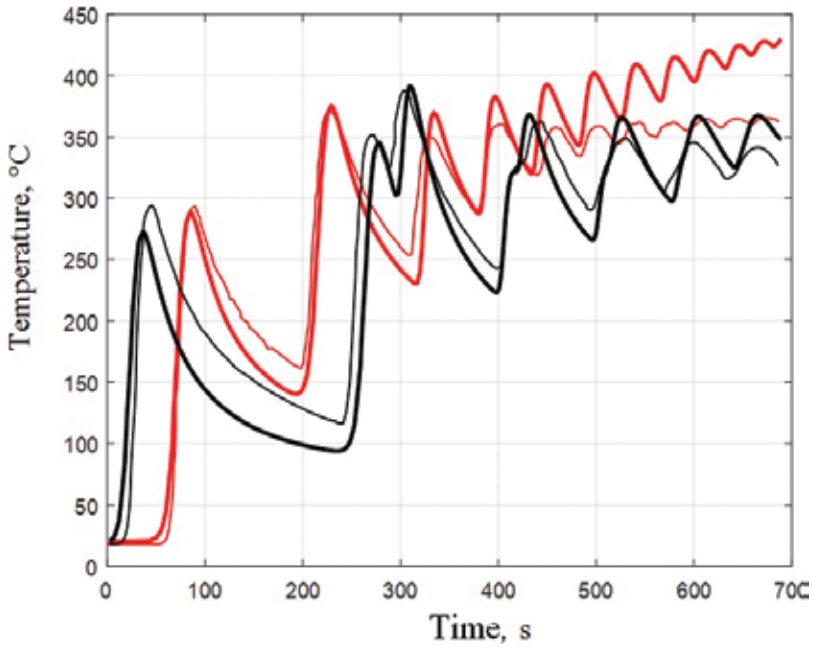


**Figure 15.** The temperature, °C in points 1 (red lined) and 4 (black lines). Thin curves show the experiment, thick curves show the calculation.

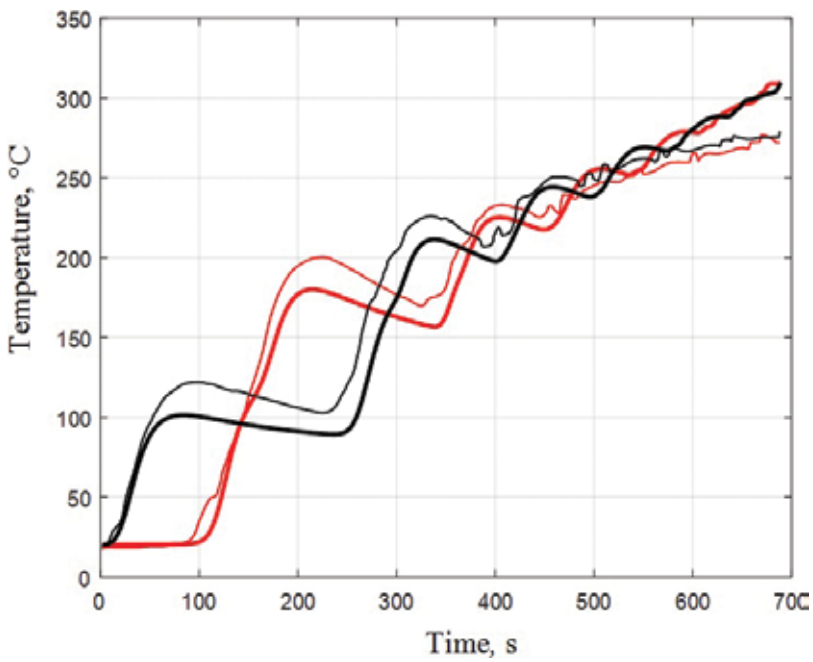


**Figure 16.** The temperature, °C in points 2 (red lined) and 6 (black lines). Thin curves—the experiment, thick curves—the calculation.

http://dx.doi.org/10.5772/intechopen.77153

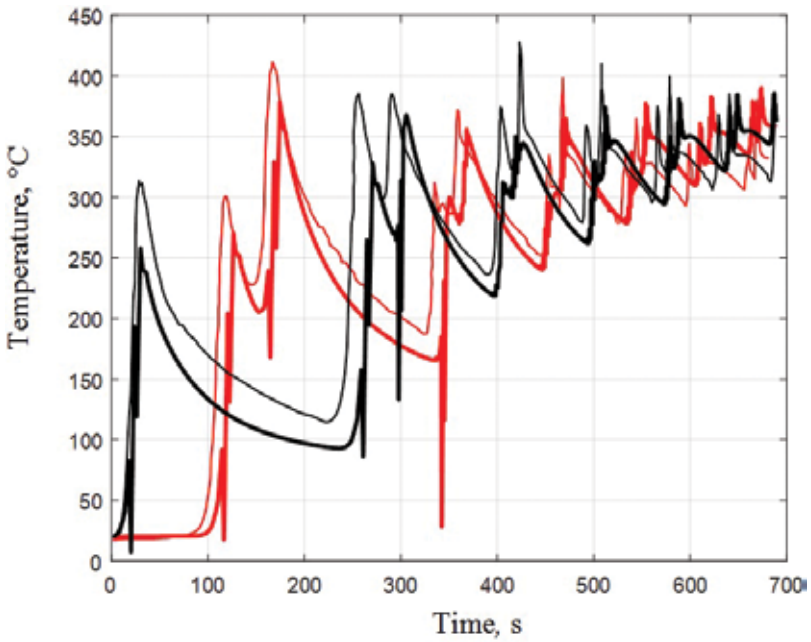


**Figure 17.** The temperature, °C in points 3 (red lined) and 5 (black lines). Thin curves—the experiment, thick curves—the calculation.

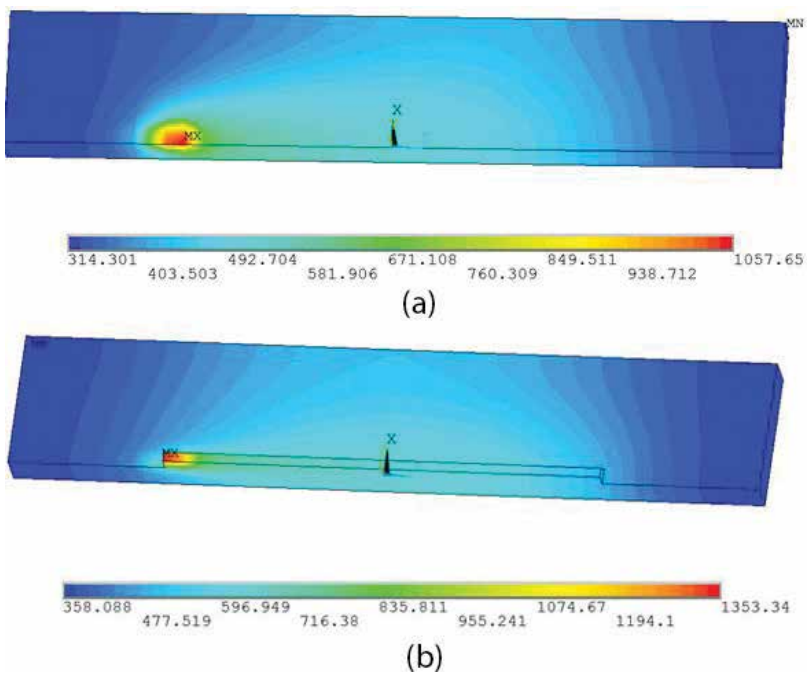


**Figure 18.** Temperature distribution, K (a) $t = 291$ s, (b) $t = 506$ s.

**Figure 18** shows by way of illustration the temperature fields at the moment of the end of preliminary heating of the base plate (**Figure 18a**) and of the end of the fourth layer (**Figure 18b**).

**Figure 19** shows the results of solution of the deformable body mechanics problem and residual displacement at central cross sections of the plate. The figure shows that the residual contraction of the structure can be estimated with acceptable accuracy. It was predicted that the plate will be bowl-shaped with the height of the ribs about 1 mm. The minimum computational accuracy is at the cross section where the relative disparity of the height runs up to 20%.

**Figure 20** represents the distribution pattern of residual characteristics in the structure.

**Figure 20a** shows that the longitudinal bend dominates. The transverse bend is almost 10 times lower. The maximum intensity of residual stresses is observed at the contact area of the deposited material and the base.

The stresses are calculated at every step of solution of the quasipermanent boundary deformable solid body problem (Eqs. (21)–(28)). **Figure 20b** represents distribution of residual stresses, i.e. the stresses observed in the structure at the end of the production process and complete cooldown to the ambient temperature.

The model of thermomechanical behavior of the sample, created by the additive fabrication method, is designed for evaluation of strain-stress state of the sample and its contraction as well as for definition of parameters of the production process ensuring low contraction and residual stress. The model can be combined with other mathematical and numerical models

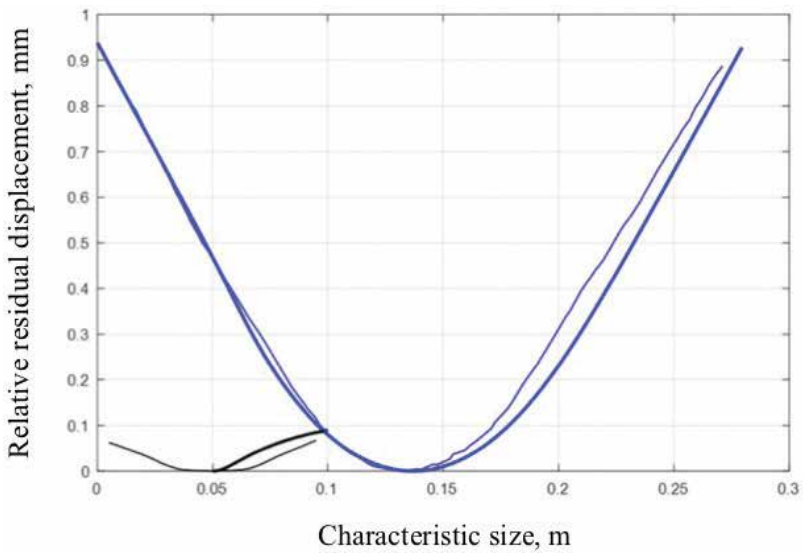


**Figure 19.** Relative residual displacement, mm, at longitudinal (blue lines) and cross (black lines) sections of the plate on its bottom surface. Thin curves show the experiment, thick curves show the calculation.

http://dx.doi.org/10.5772/intechopen.77153

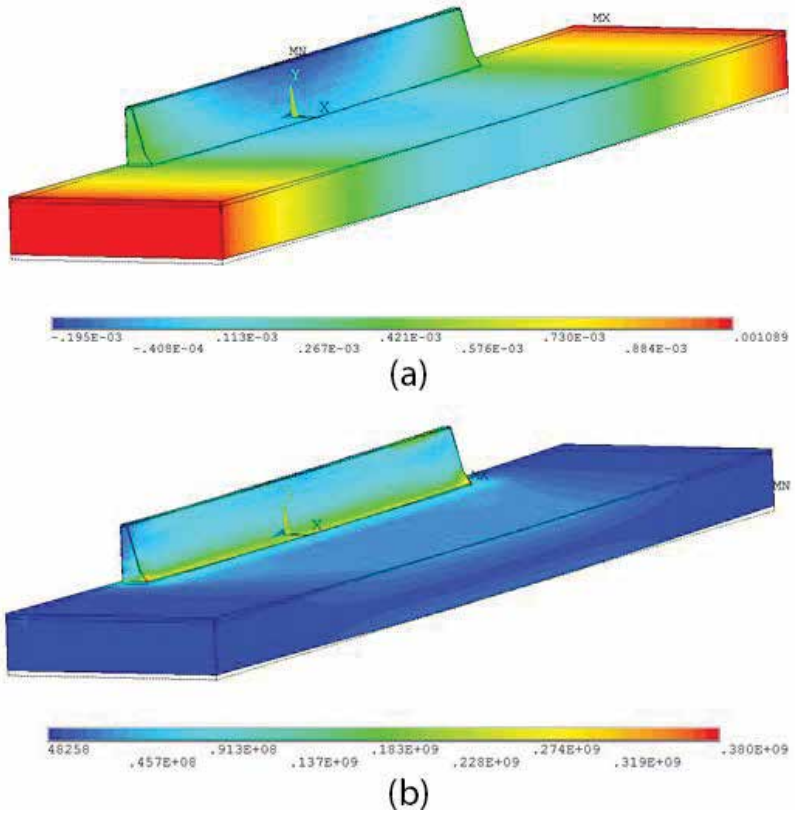


**Figure 20.** Vertical displacement in the structure after its cooldown and release, m (a), residual stress intensity, Pa (b).

including the temperature and conversion model specifying distribution of the variable temperature field inside the sample.

The model may be included into a computer-aided expert system to forecast the results of additive fabrication of large-sized components.

## 5. Conclusions

1. We defined the mathematical problem (model) of heat and mass transfer in the process of additive fabrication of products by fusion of wire material using plasma (electric) arc and concentrated energy sources with asymmetrical wire feed. The model describes transient nonequilibrium adjoint heat and mass transfer processes in molten metal with free surface, includes differential equation of viscous fluid movement (Navier-Stokes equations) with

convective terms in laminar current, takes into account the Marangoni effect on the surface of melt, and allows to calculate volume distribution of temperatures, melt flow speed, pressure, shape and dimensions of the molten pool, shape of the molten metal free surface, shape and dimensions of the deposited bead. We also defined potential uses of the models.

2. We suggested approximation of the wire feed process by mass inflow on the metal-gas edge. To describe movement of the molten-solid metal interface, one can use any of the two following methods: the Level-Set method or the Arbitrary Lagrangian-Eulerian method (ALE).

3. We described the heat source when using a plasma arc of various electrical polarity. In the process of deposition with reverse polarity, the plasma source is represented by a combination of the source of the heat, transferred by the plasma flow, with Gaussian distribution and a uniformly distributed source in the area of cathode spots impact. The energy relation between the sources is defined by experiment. We preselected the approximating formulas which describe influence of technological parameters of plasma arcs on distribution of heat flow density in the source.

4. We suggested the mathematical 3D-model of the additive product fabrication process by deposition of wire material.

5. We developed and implemented in the form of an APDL program in the ANSYS package the algorithm for estimation of unsteady temperature fields and strain-stress state of the structure in the process of its generation by arc 3D-deposition of wire materials.

6. The experimental information of other authors was used to identify the thermal-physical and thermomechanical properties of the material—the Inconel 718 nickel alloy.

7. Verification of the model showed required accuracy of the results.

8. The represented example of application of the model and its numerical implementation in the ANSYS package shows that the chosen approach is reasonable and allows to obtain acceptable numerical results properly describing real effects and processes in the objects created by the method of additive volume generation. More accurate verification procedure for the suggested mathematical model showing its accuracy and limits of applicability on the basis of experimental studies of residual stresses and thermoshrinkable deformations of model products manufacturing using the method of additive part fabrication by fusion of wire material with an electric arc and concentrated energy sources will be represented in future studies.

## Acknowledgements

The work was supported by the Ministry of Education and Science of the Russian Federation (RFMEFI58317X0062) and MOST (No. 2017YFE0100100) under the BRICS project.

## Author details

Dmitriy Trushnikov[1]*, Oleg Smetannikov[2], Anatoly Perminov[3], Shengyong Pang[4], Karuppasamy Poolan Karunakaran[5], Petr Maksimov[2], Mariia Bartolomey[2], Aleksei Kovyazin[2], Vladimir Belenkiy[6] and Yurii Schitsyn[1]

*Address all correspondence to: trdimitr@yandex.ru

1 Department of Welding Production, Metrology and Technology of Material, Mechanical Engineering Faculty, Perm National Research Polytechnic University, Perm, Russia

2 Department of Computational Mathematics and Mechanics, Faculty of Applied Mathematics and Mechanics, Perm National Research Polytechnic University, Perm, Russia

3 Department of General Physics, Faculty of Applied Mathematics and Mechanics, Perm National Research Polytechnic University, Perm, Russia

4 State Key Laboratory of Materials Processing and Die and Mould Technology, Huazhong University of Science and Technology, Wuhan, China

5 Department of Mechanical Engineering, Rapid Manufacturing Laboratory, Indian Institute of Technology Bombay, Mumbai, India

6 Mechanical Engineering Faculty, Perm National Research Polytechnic University, Perm, Russia

## References

[1] Sciaky Inc. Electron Beam Additive Manufacturing (EBAM)—Advantages of Wire AM vs. Powder AM. URL: http://additivemanufacturing.com/2015/10/14/electron-beam-additive-manufacturing-ebamadvantages-of-wire-am-vs-powder-am

[2] Sciaky Inc. Electron Beam Additive Manufacturing (EBAM). URL: http://www.sciaky.com/images/pdfs/product-sheets/Sciaky-EBAM-Technology.pdf

[3] Jhavar S, Jain NK, Paul CP. Development of micro-plasma transferred arc (p-PTA) wire deposition process for additive layer manufacturing applications. Journal of Materials Processing Technology. 2014;**214**(5):1102-1110

[4] Louvis E et al. Selective laser melting of aluminium components. Journal of Materials Processing Technology. Department of Engineering, The University of Liverpool, Liverpool L69 3GH, United Kingdom. 2011;**211**:275-284

[5] Campanelli SL et al. Capabilities and Performances of the Selective Laser Melting Process. Polytechnic of Bari, Department of Management and Mechanical Engineering, Viale Japigia, 182 Italy [electronic source]. URL: http://cdn.intechopen.com/pdfs/12285/InTech-

Capabilities_and_performances_of_the_selective_laser_melting_process.pdf Three-dimensional Printing and Additive Manufacturing of High-performance Metals and Alloys

[6] Yu A. Bezobrazov, Zlenko MA, Zotov OG, et al. Analysis of the structure of samples obtained by DMLS and SLM methods of rapid prototyping. In: Innovative Technologies in Metallurgy and Machine Building: Materials of the 6th International Youth Scientific and Practical Conference in Innovative Technologies in Metallurgy and Machine Building. Ural Scientific and Pedagogical School n.a. Professor A.F. Golovin [the city of Ekaterinburg, October 29–November 1, 2012]; Ekaterinburg: Ural University Publishing House; 2012. pp. 154-157

[7] Qiu C, Panwisawas C,Ward M, Basoalto HC, Brooks JW, Attallah MM. On the role of melt flow into the surface structure and porosity development during selective laser melting. Acta Materialia. September 1, 2015;**96**:72-79. DOI: 10.1016/j.actamat.2015.06.004. ISSN 1359-6454 (http://www.sciencedirect.com/science/article/pii/SI359645415003870)

[8] Kapil S, Legesse F, Kulkarni PM, Joshi P, Desai A, Karunakaran KP. Hybrid layered manufacturing using tungsten inert gas cladding. Progress in Additive Manufacturing. 2016;**1**(1):79-91

[9] Zhang Y, Bernard A, Harik R, Karunakaran KP. Build orientation optimization for multipart production in additive manufacturing. Journal of Intelligent Manufacturing. 2017;**28**(6): 1393-1407

[10] Amine T, Newkirk JW, Liou F. Investigation of effect of process parameters on multilayer builds by direct metal deposition. Applied Thermal Engineering. 2014;**73**(1):500-511

[11] Hu YP, Chen CW, Mukherjee K. Measurement of temperature distributions during laser cladding process. Journal of Laser Applications. 2000;**12**(3):126-130

[12] Shishkovsky IV, Scherbakov VI, Morozov YG, Kuznetsov MV, Parkin IP. Surface laser sintering of exothermic powder compositions. Journal of Thermal Analysis and Calorimetry. 2008;**91**(2):427-436

[13] Benda J. Temperature controlled selective laser sintering. In: Proceedings of the Solid Freeform Fabrication Symposium; 1994. pp. 277-284

[14] Doubenskaia M, Pavlov M, Chivel Y. Optical system for on-line monitoring and temperature control in selective laser melting technology. Key Engineering Materials. 2010;**437**: 458-461

[15] Hu DM, Kovacevic R. Sensing, modeling and control for laser-based additive manufacturing. International Journal of Machine Tools & Manufacture. 2003;**43**(l):51-60

[16] Jian X, Jinghua S, Yiqingc G. Novel measurement method for selective laser sintering transient temperature field. In: 3rd International Symposium on Advanced Optical Manufacturing and Testing Technologies: Optical Test and Measurement Technology and Equipment; 2007. pp. 67234N-67234N

[17] Price S, Cooper K, Chou K. Evaluations of temperature measurements by near-infrared thermography in powder-based electron-beam additive manufacturing. In: Proceedings of the Solid Freeform Fabrication Symposium. Austin (TX): University of Texas; 2012. pp. 761-773

[18] Mughal MP, Fawad H, Mufti RA, Siddiquc M. Deformation modelling in layered manufacturing of metallic parts using gas metal arc welding: Effect of process parameters. Modelling and Simulation in Materials Science and Engineering. 2005;**13**(7):1187-1204

[19] Beuth VA, JL GM. Process maps for predicting residual stress and melt pool size in the laser-based fabrication of thin-walled structures. Journal of Manufacturing Science and Engineering. 2007;**129**(1):101-109

[20] Manvatkar V, De A, DebRoy T. Heat transfer and material flow during laser assisted multi-layer additive manufacturing. Journal of Applied Physics. 2014;**116**(12):1-8. Article No. 124905

[21] Svensson LE, Gretoft B, Bhadeshia HKDH. An analysis of cooling curves from the fusion zone of steel weld deposits. Scandinavian Journal of Metallurgy. 1986;**15**(2):97-103

[22] Markl M, Korner C. Multiscale modeling of powder bed-based additive manufacturing. Annual Review of Materials Research. 2016;**46**:93-123

[23] Manvatkar V, De A, DebRoy T. Spatial variation of melt pool geometry, peak temperature and solidification parameters during laser assisted additive manufacturing process. Materials Science and Technology. 2015;**31**(8):924-930

[24] Raghavan A, Wei HL, Palmer TA, DebRoy T. Heat transfer and fluid flow in additive manufacturing. Journal of Laser Applications. 2013;**25**(5):1-8. Article No. 052006

[25] Patankar S. Numerical Heat Transfer and Fluid Flow. Hemisphere, New York: CRC Press; 1980

[26] King W, Anderson A, Ferencz R, Hodge N, Kamath C, Khairallah S. Overview of modelling and simulation of metal powder bed fusion process at Lawrence Livermore National Laboratory. Materials Science and Technology. 2015;**31**(8):957-968

[27] Li C, Wang Y, Zhan H, Han T, Han B, Zhao W. Three-dimensional finite element analysis of temperatures and stresses in wide-band laser surface melting processing. Materials & Design. 2010;**31**(7):3366-3373. DOI: 10.1016/j.matdes.2010.01.054

[28] Ma L, Bin H. Temperature and stress analysis and simulation in fractal scanning-based laser sintering. International Journal of Advanced Manufacturing Technology. 2007;**34**(9): 898-903

[29] Roberts IA et al. Experimental and numerical analysis of residual stresses in additive layer manufacturing by laser melting of metal powders [Электронный документ]. Key Engineering Materials. 2011;**450**:461-465. DOI: 10.4028/www.scientific.net/KEM.450.461 (http:// 32 www.scientific.net/KEM.450.461). Проверено 14.10.2017

[30] Parry L, Ashcroft I, Bracket D, Wildman RD. Investigation of residual stresses in selective laser melting. Key Engineering Materials. 2015;**627**:129-132

[31] Wu A, Brown D, Kumar M, Gallegos G, King W. An experimental investigation into additive manufacturing-induced residual stresses in 316L stainless steel. Metallurgical and Materials Transactions. 2014;**45A**:1-11

[32] Baufeld B, Van der Biest O, Gault R. Additive manufacturing of Ti–6Al–4V components by shaped metal deposition: Microstructure and mechanical properties. Materials & Design. 2010;**31**:106-111

[33] Riedlbauer D, Mergheim J, McBride A, Steinmann P. Macroscopic modelling of the selective beam melting process. Proceedings in Applied Mathematics and Mechanics. 2012;**12**(1): 381-382

[34] Labudovic M, Hu D, Kovacevic R. A three dimensional model for direct laser metal powder deposition and rapid prototyping. Journal of Materials Science. 2003;**38**(1):35-49

[35] Hodge NE, Ferencz RM, Solberg JM. Implementation of a thermomechanical model for the simulation of selective laser melting. Computational Mechanics. 2014;**54**(1):33-51

[36] Denlinger ER, Michaleris P. Effect of stress relaxation on distortion in additive manufacturing process modeling. Additive Manufacturing. 2016;**12**:51-59

[37] Korner C. Additive manufacturing of metallic components by selective electron beam melting—A review. International Materials Review. 2016;**61**(5):361-377

[38] Prabhakar P, Sames W, Dehoff R, Babu S. Computational modeling of residual stress formation during the electron beam melting process for Inconel 718. Additive Manufacturing. 2015;**7**:83-91

[39] Neulybin SD, Permyakov LD, Trushnikov DN, Shchitsyn YD, Belenkiy VY. Development of a dynamic model of thermal processes for plasma surfacing at direct and reverse polarity. International Journal of Applied Engineering Research. 2017;**12**(22):11847-11854

[40] Asai S, Muchi I. Theoretical analysis and model experiments on the formation mechanism of channel-type segregation. Transactions of the Iron and Steel Institute of Japan. 1978;**18** (2):90-98

[41] Kharitonov IA, Martynov VN, Shcherbakov AV, Dragunov VK, Gaponova DA. The Second International Conference on Electron Beam Welding and Related Technologies; November 14–17, 2017; National Research University Moscow Power Engineering Institute: Collection of Materials and Reports. pp. 257-265

[42] Bennon WD, Incropera FP. A continuum model for momentum, heat and species transport in binary solid-liquid phase change systems. I. Model formulation. International Journal of Heat and Mass Transfer. 1987;**30**:2161-2169

[43] Qi H, Mazumder J, Ki H. Numerical simulation of heat transfer and fluid flow in coaxial laser cladding process for direct metal deposition. Journal of Applied Physics. 2006;**100**(2): 024903

[44] Gan Z, Yu G, He X, Li S. Surface-active element transport and its effect on liquid metal flow in laser-assisted additive manufacturing. International Communications in Heat and Mass Transfer. 2017;**86**:206-214

[45] He X, Mazumder J. Transport phenomena during direct metal deposition. Journal of Applied Physics. 2007;**101**:053-113

[46] Shchitsyn VY, Yazovskikh VM. Influence of polarity on heat input into the nozzle of a plasma torch. Welding Production. 2002;**1**:17-19

[47] Sosnin NA, Ermakov SA, Topolyansky PA. Plasma Technologies. Manual for Engineers. SPb: Publishing House of Polytechnic University; 2008. p. 406

[48] Vainerman AE, Zakharov VF, Prilukov VN, Syutev AN. Surfacing with a compressed arc of a reverse polarity of chromium-nickel steel on structural steels. In: Plasma Methods of Metal Processing. Leningrad: Leningrad Publishing House of Scientific and Technical Propaganda; 1977. pp. 27-34

[49] Vainerman AE, Krasulin YL, Shorshorov MK. Plasma surfacing of copper and bronze on steel with a plasma jet. In: Automatic Welding, Leningrad [without publisher]; 1966. p. 35

[50] Neubybin SD. Influence of current polarity of the properties of layered materials obtained by multilayer plasma surfacing [Text]: PhD Thesis in Technical Sciences of February 5, 2010—Welding, Related Processes and Technologies; Perm National Research Polytechnic University—Perm, 2017. p.135

[51] Harvey PD, editor. Engineering Properties of Steels. Metals Park, OH: American Society for Metals; 1982

[52] Peckner D, Bernstein IM. Handbook of Stainless Steels. New York, NY: McGraw-Hill Book Company; 1977

[53] Boyer HE, Gall TL, editors. Metals Handbook. Materials Park, OH: American Society for Metals; 1985

[54] ASM International Handbook Committee. Metals Handbook. 10th ed. Vol. 1. Materials Park, OH: ASM International; 1990

[55] Shchitsyn YD, Kosolapov OA, Strukov NN. Energy distribution of a compressed arc during the operation of a plasma torch of a reverse polarity. Welding and Diagnostics. 2010;**3**:13-16

[56] King W, Anderson A, Ferencz R, Hodge N, Kamath C, Khairallah S. Overview of modelling and simulation of metal powder bed fusion process at Lawrence Livermore National Laboratory. Materials Science and Technology. 2015;**31**(8):957-968

[57] Li C,Wang Y, Zhan H,Han T, Han B, Zhao W. Three-dimensional finite element analysis of temperatures and stresses in wide-band laser surface melting processing. Materials & Design. 2010;**31**(7):3366-3373. DOI: 10.1016/j.matdes.2010.01.054

[58] Roberts IA et al. Experimental and numerical analysis of residual stresses in additive layer manufacturing by laser melting of metal powders [electronic document]. Key Engineering

Materials. 2011;**450**:461-465. DOI: 10.4028/www.scientific.net/KEM.450.461 (http://www.scientific.net/KEM.450.461). Reviewed on October 14, 2017

[59] Martukanitz R, Michaleris P, Palmer T, DebRoy T, Liu Z-K, Otis R, et al. Toward an integrated computational system for describing the additive manufacturing process for metallic materials. Additive Manufacturing. 2014;**1**:52-63

[60] Michaleris P. Modeling metal deposition in heat transfer analyses of additive manufacturing processes. Finite Elements in Analysis and Design. 2014;**86**:51-60

[61] Papadakis L, Loizou A, Risse J, Schrage J. Numerical computation of component shape distortion manufactured by selective laser melting. Procedia CIRP. 2014;**18**:90-95. DOI:03 10.1016/j.procir.2014.06.l 13

[62] Shishkovsky IV, Volyansky I. Experimental and numerical modelling of function-graded porous filter elements, synthesized by the SLS method. In: High Value Manufacturing: Advanced Research in Virtual and Rapid Prototyping: Proceedings of the 6th International Conference on Advanced Research in Virtual and Rapid Prototyping, Leiria, Portugal; October 1–5, 2013. p. 55

[63] Alimardani M, Toyserkani E, Huissoon JP. A 3D dynamic numerical approach for temperature and thermal stress distributions in multilayer laser solid freeform fabrication process. Optics and Lasers in Engineering. 2007;**45**(12):1115-1130

[64] Beuth J, Klingbeil N. The role of process variables in laser-based direct metal solid freeform fabrication. JOM. 2001;**53**(9):36-39

[65] Wang L, Felicelli SD, Pratt P. Residual stresses in LENS-deposited AISI 410 stainless steel plates. Materials Science and Engineering A. 2008;**496**(1-2):234-241

[66] Ghosh S, Choi J. Three-dimensional transient finite element analysis for residual stresses in the laser aided direct metal/material deposition process. Journal of Laser Applications. 2005;**17**(3):144-158

[67] Ghosh S, Choi J. Modeling and experimental verification of transient/residual stresses and microstructure formation in multi-layer laser aided DMD process. Journal of Heat Transfer. 2006;**128**(7):662-679

[68] Farahmand P, Kovacevic R. An experimental-numerical investigation of heat distribution and stress field in single- and multi-track laser cladding by a high-power direct diode laser. Optics and Laser Technology. 2014;**63**:154-168

[69] Ding J, Colegrove P, Mehnen J, Ganguly S, Almeida PMS, Wang F, et al. Thermomechanical analysis of wire and arc additive layer manufacturing process on large multilayer parts. Computational Materials Science. 2011;**50**(12):3315-3322

[70] Zhao XM, Chen J, Lin X, Huang WD. Study on microstructure and mechanical properties of laser rapid forming Inconel 718. Materials Science and Engineering A. 2008;**478**(1-2): 119-124

[71] Mukherjee T, Zuback JS, De A, DebRoy T. Printability of alloys for additive manufacturing. Scientific Reports. 2016;**6**:1-8. Article No. 9717

[72] Martina F, Mehnen J, Williams SW, Colegrove P, Wang F. Investigation of the benefits of plasma deposition for the additive layer manufacture of Ti-6Al-4V. Journal of Materials Processing Technology. 2012;**212**(6):1377-1386

[73] Chiumenti M, Cervera M, Salmi A, de Saracibar CA, Dialami N, Matsui K. Finite element modeling of multi-pass welding and shaped metal deposition processes. Computer Methods in Applied Mechanics and Engineering. 2010;**199**(37-40):2343-2359

[74] Denlinger ER, Irwin J, Michaleris P. Thermomechanical modeling of additive manufacturing large parts. Journal of Manufacturing Science and Engineering. 2014;**136**(6):061007

[75] Mukherjee T, Manvatkar V, De A, DebRoy T. Mitigation of thermal distortion during additive manufacturing. Scripta Materialia. 2017;**127**:79-83

[76] Goldak JA, Akhlaghi M. ComputationalWelding Mechanics. 1st ed. US: Springer; 2006

[77] Ding J, Colegrove P, Mehnen J, Williams S, Wang F, Almeida PS. A computationally efficient finite element model of wire and arc additive manufacture. International Journal of Advanced Manufacturing Technology. 2014;**70**(1-4):227-236

[78] Li C, Fu C, Guo Y, Fang F. A multiscale modeling approach for fast prediction of part distortion in selective laser melting. Journal of Materials Processing Technology. 2016;**229**: 703-712

[79] Yuan MG, Ueda Y. Prediction of residual stresses in welded T- and I-joints using inherent strains. Journal of Engineering Materials and Technology. 1996;**118**(2):229-234

[80] INCONEL® alloy 718 properties. Special Metals. Url: http://www.specialmetals.com/15 assets/smc/documents/alloys/inconel/inconel-alloy-718.pdf

[81] Mohanty S, Hattel JH. Numerical model based reliability estimation of selective laser melting process. Physics Procedia. 2014;**56**:379-389. DOI: 10.1016/j.phpro.2014.08.135

[82] Ilin A, Logvinov R, Kulikov A, Prihodovsky A, Xu H, Ploshikhin V, Gunther B, Bechmann F. Computer aided optimisation of the thermal management during laser beam melting process. Physics Procedia. 2014;**56**:390-399. DOI: 10.1016/j.phpro.2014.08.142

[83] Kaplan AFH, Norman P, Eriksson I. Analysis of the keyhole and weld pool dynamics by imaging evaluation and photodiode monitoring. In: Proceedings of LAMP2009—the 5th International Congress on Laser Advanced Materials Processing; 2009. pp. 1-6

[84] Askaryan GA, Morozov EM. Pressure in the evaporation of a substance in ray-radiation. Journal of Experimental and Theoretical Physics. 1962;**43**(6):2319-2320

[85] Agelet de Saracibar C, Lundbäck A, Chiumenti M, Cervera M. Shaped metal deposition processes. In: Encyclopedia of Thermal Stresses. Dordrecht: Springer; 2014. pp. 4346-4355. DOI: 10.1007/978-94-007-2739-7_808

[86] Overfelt RA, Sahai V, Ko YK, Berry JT. Porosity in cast equiaxed alloy 718 Superalloys 718, 625, 706 and Various Derivatives. In: Proceedings of the International Symposium on Superalloys 718, 625, 706 and Various Derivatives, Pittsburg, Pennsylvania; 1994. pp. 189-200

[87] Nowotnik A, Pędrak P, Sieniawski J, Góral M. Mechanical properties of hot deformed Inconel 718 and X750. Journal of Achievements in Materials and Manufacturing Engineering. 2012;**50**(2):74-80

[88] Smetannikov OY, Trushnikov DN, Maksimov PV, Bartolomey ML, Kovyazin AV. Modeling of the thermomechanical behavior of the product during process of 3D deposition of wire materials in ANSYS. PNRPU Mechanics Bulletin. 2017;**4**:154-172. DOI: 10.15593/04 perm.mech/2017.4.11

Chapter 4

# Theory and Technology of Direct Laser Deposition

Gleb Turichin and Olga Klimova-Korsmik

Additional information is available at the end of the chapter

http://dx.doi.org/10.5772/intechopen.76860

**Abstract**

Presently the additive technologies in manufacturing are widely developed in all industrialized countries. Replacing the traditional technology of casting and machining with additive technologies, one can significantly reduce material consumption and labor costs. They also allow obtaining products with desired properties. The most promising for manufacturing large-sized products is the additive technology of high-speed direct laser deposition. Using this technology allows to create complex parts and construction to one technological operation without using addition equipment and tools. This technology allows decreasing of consumption of raw materials and decrease amount of waste. Equipment for realization of DLD technology is universal and based on module design principle. DLD is based on layer-by-layer deposition and melting of powder by laser beam from using a sliced 3D computer-aided design (CAD) file. The materials used are powders based on Fe, Ni, and Ti. This chapter presents the results of machine design and research HS DLD technology from various materials.

**Keywords:** high-speed direct laser deposition, additive manufacturing, stability of process, equipment, structure, properties

## 1. Introduction

New manufacturing technologies are incorporated into most areas of engineering: aircraft industry, shipbuilding, medicine, engine construction, etc. Existing requirements for its demand are more energy efficient and have environmental compatibility; additive technologies meet both criteria. The intensive development of additive technologies in recent years makes it possible to improve the methods of manufacturing and processing products [1–5]. They allow saving expensive raw materials in comparison with classical production methods, during which up to 90% of the material can be removed. The issue of cost reduction is

especially relevant in knowledge-based industries (gas turbine engine construction, aviation, space exploration, etc.). Selective laser melting (SLM) technology has already been implemented in production in many countries of the world [6, 7]. However, SLM technology is limited by its inability to manufacture large-sized products and low productivity.

The main trend in the development of additive technology is to increase productivity while maintaining the required quality of the product. The most promising technology of product manufacturing is direct laser deposition analogue direct metal deposition (DMD), when the product is formed from a powder, which is supplied by compressed gas-powder jet directly into the laser action zone [8–11]. The jet can be as coaxial and as non-coaxial to focused laser beam, which provides heating and partial melting of the powder and heating the substrate. This technology allows to include a mixture of powders into the gas-powder jet and to change the composition of powders during the process.

The developed technology and equipment have several advantages in comparison with existing analogues. There is a high productivity of DLD process for the manufacture of real parts and products: up to 2.5 kg/h for nickel and iron alloys, up to 1.2 kg/h for titanium alloys. For similar equipment, the productivity is 2–3 times less [12–14]. There are experimental stands with the same high productivity (up to 2 kg/h), preferably [15]. The main feature of the developed equipment is a modular assembly type, which allows to modernize the installation at the customer's request. This is the first Russian technology and equipment for the implementation of additive production.

Complex studies were carried out to understand the relationship between the parameters of the process and the optimization of the technology for obtaining products with specified characteristics. As a result of the research done, the theory and technology of high-speed direct laser deposition are developed. Also a number of machines with various sizes are made for the implementation of this technology. Investigations for powder materials based on iron, nickel, and titanium demonstrated the possibility of obtaining high-quality parts and products. Also, the possibility of working with cermet materials is shown. The research results showed that developed technology of direct laser deposition can replace the currently used technologies, providing multiple increase productivity and material savings, in spite of its technological complexity.

## 2. Theory of high-speed direct laser deposition

The processes that occur during high-speed laser deposition depend on a large number of distributed parameters which effect on the result [8]. An important aspect of the study is the stability of the direct laser deposition process. Previously, the authors studied the root peak formation in welds during the process of laser welding using highly concentrated energy fluxes. According to the present knowledge about the physical nature of these processes, the

reason for instabilities is self-oscillations of the weld pool [12–19]. Different experimental data confirm this idea [16, 19].

The stability of surface formation in the process of direct laser deposition is determined by the complex of physical processes occurring on the surface of the molten pool, which moves with high speed along the deposited product at a constant flow of matter to its surface. Hydrodynamic stability of melt flow in semiliquid bath, formed by substrate melting under laser beam heating and powder income, depends on driving force, which leads to melt motion. The main driving force for melt motion relative solid substrate in DLD process is Marangoni effect. Therefore velocity of liquid relative solid phase is determined by the rate of the thermocapillary flow [20]. To make the analysis more clear, it is convenient to confine to analyze practically interesting case, when the molten pool length "L" is much greater than its width "b" and depth "H," which depend on parameters of deposition mode. Then analysis of the equation of continuity of the melt allows us to conclude that the "longitudinal" velocity component $v_x$ directed along the axis of the laser beam motion relative to the target is much larger than transverse components $v_y$ and $v_z$ so we the boundary layer like flow. So that equation of the motion can be written in our case as

$$\frac{\partial v_x}{\partial t} + v_x \frac{\partial v_x}{\partial x} = -\frac{1}{\rho}\frac{\partial \rho}{\partial x} + v\frac{\partial^2 v_x}{\partial z^2} \tag{1}$$

At the "bottom" of the molten pool, which coincides with the previous layer surface, the "sticking" condition is fulfilled $v_x|_{z=0} = 0;$ on the surface, the continuity condition of the tangential component of the stress tensor is $\eta \frac{\partial v_x}{\partial z}\Big|_{z=H} = \frac{\partial \sigma}{\partial x}$, where σ is the coefficient of surface tension. Assuming that at the front of the melt pool the surface temperature close to the boiling one and the surface tension value close to "0," taking a linear law for the temperature drop to the "tail" of the melt pool, one can write

$$\eta \frac{\partial v_x}{\partial z}\bigg|_{z=H} = \frac{\sigma}{L} \tag{2}$$

It is possible to get after a number of transformations that with the consideration of Marangoni force, Eq. (1) can be written in the next shape:

$$\frac{\partial v_x}{\partial t} + v_x \frac{\partial v_x}{\partial x} = -\frac{1}{\rho}\frac{\partial \rho}{\partial x} - 3v\frac{v_x}{H^2} + \frac{3\sigma}{2\rho LH} \tag{3}$$

One can use the mass conservation condition to connect the melt velocity $v_x$ with position of the melt pool surface. Let ζ be the height of the perturbation on surface. In our case, the mass flux coming to the melt surface with the gas-powder jet must be taken into account. One can denote the incident mass flux density on melt surface as j (x, ζ). Suppose ζ < < H, it is possible to write the continuity condition of the mass flux as

$$\frac{\partial v_x}{\partial x} \approx -\frac{1}{H}\frac{\partial \zeta}{\partial t} + \frac{j(x,0)}{H\rho} + \frac{1}{H\rho}\frac{\partial j(x)}{\partial x}\zeta. \tag{4}$$

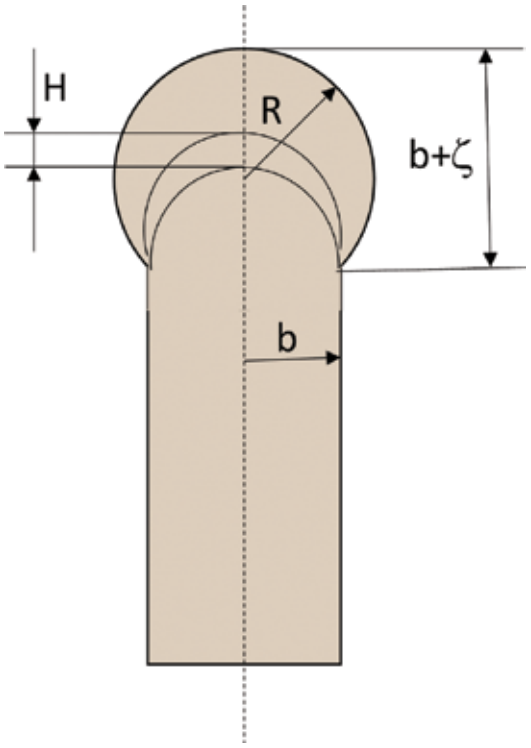


**Figure 1.** Geometry of the melt pool surface motion.

One can determine the Laplace pressure in the liquid "p" and the additional pressure, which is related to the perturbation of the melt pool surface ζ, taking into account that p = σ/R, where R is the radius of surface curvature (**Figure 1**).

The one-dimensional model of thermocapillary flow does not allow introducing the effects of the influence of grown wall thickness on change in the shape of its surface. For that, we need to introduce a "transverse" dimension. Analysis of term scales in the continuity equation show that melt velocity in "transverse" direction is negligible but pressure changes can be significant. Therefore, when ζ << H, one can get $R \approx b + \frac{\zeta^2}{2b}$, and for pressure it is possible to obtain $p \approx \frac{\sigma}{b} - \frac{\sigma\zeta^2}{2b^3}$.

Considering it, one can write Navier-Stokes equation in the two-dimensional case as

$$\frac{\partial v_x}{\partial t} + v_x \frac{\partial v_x}{\partial x} = -\frac{\sigma}{\rho}\frac{\partial^3 \zeta}{\partial x^3} - 3v\frac{v_x}{H^2} + \frac{3\sigma}{2\rho LH} + \frac{\sigma}{\rho b^3}\frac{\zeta \partial \zeta}{\partial x} \tag{5}$$

In the steady-state approximation, with consideration of mass flux conservation, this equation can be simplified as

$$\frac{\partial^3 \zeta}{\partial x^3} - \frac{\rho {v_0}^2}{\sigma H}\frac{\partial \zeta}{\partial x} = \frac{3}{2LH} - 3v\frac{\rho v_0}{\sigma H^2} - \frac{v_0 j(x,0)}{\sigma H} \tag{6}$$

The boundary conditions for this task are given by $\zeta = 0$ at $x = 0$, $\frac{\partial \zeta}{\partial x}\big|_{x=0} = 0$, $\frac{\partial \zeta}{\partial x}\big|_{x=L} = 0$.

Solution of this problem can be written as

$$\zeta = A\frac{H^2}{G}x + A\left(\frac{H^2}{G}\right)^{3/2}\frac{2 - \exp\sqrt{\frac{G}{H^2}}L - \exp\left(-\sqrt{\frac{G}{H^2}}L\right)}{\exp\sqrt{\frac{G}{H^2}}L - \exp\left(-\sqrt{\frac{G}{H^2}}L\right)} - -A\left(\frac{H^2}{G}\right)^{3/2}$$
$$\frac{1 - \exp\left(-\sqrt{\frac{G}{H^2}}L\right)}{\exp\sqrt{\frac{G}{H^2}}L - \exp\left(-\sqrt{\frac{G}{H^2}}L\right)}\exp\sqrt{\frac{G}{H^2}}x - \tag{7}$$
$$-A\left(\frac{H^2}{G}\right)^{3/2}\frac{1 - \exp\left(\sqrt{\frac{G}{H^2}}L\right)}{\exp\sqrt{\frac{G}{H^2}}L - \exp\left(-\sqrt{\frac{G}{H^2}}L\right)}\exp\left(-\sqrt{\frac{G}{H^2}}x\right)$$

where $G = \frac{\rho v_0{}^2 H}{\sigma}$, $A = -\frac{3}{2LH} + 3v\frac{\rho v_0}{\sigma H^2} + \frac{v_0 j(x,0)}{\sigma H}$.

At the rear part of the melt pool at x = L for the value of $\zeta$, we get

$$\zeta|_{x=L} = A\left(\frac{H^2}{G}\right)^{3/2}\left[\sqrt{G}\frac{L}{H} + 2\frac{1 - Ch\left(\sqrt{G}\frac{L}{H}\right)}{Sh\left(\sqrt{G}\frac{L}{H}\right)}\right] \tag{8}$$

Let us analyze this expression. Depending on the sign of "A," which depends on what is more—underestimation of the surface due to thermocapillary acceleration of the melt flow or its overstating caused by the input of a new material with a gas-powder jet; formation of dimple and humps on melt pool surface is possible. The height of the hump, depending on the speed of the process and the length of the melt pool, can significantly exceed the depth of the melt pool H. Such modes are most dangerous from the point of view of unstable surface formation, but it is impossible to analyze this case using the approximations of the "boundary layer" and the smallness of "$\zeta$." This analysis is a theoretical description of the process of forming the profile of the melt pool surface, taking into account the capillary phenomena and the flow of material that the gas-powder jet brings. For the analysis of nonstationary phenomena leading to instability of the growing process, it is necessary to keep the "nonstationary" terms with time derivatives in the equations and to analyze the stability of the "quasi-stationary" behavior.

We derive an equation describing the dynamic behavior of the local excess of the "$\zeta$" melt pool surface above the "quasi-stationary" surface calculated above. We use the nonstationary Navier-Stokes Eq. (5) and the continuity of the flow Eq. (4) for this purpose. Suppose that

$$v_x(x, t) = v_0(x) + v_1(x, t) \tag{9}$$

assuming that $v_1(x, t) \ll v_0(x)$. Then, obviously,

$$\zeta(x,t) = \zeta(x) + \zeta_1(x,t) \tag{10}$$

where ζ(x) is given by expression Eq. (7). Taking this into account, we obtain from Eq. (10)

$$\frac{\partial v_1}{\partial x} \approx \frac{1}{H}\frac{\partial \zeta_1}{\partial t} + \frac{1}{H\rho}\frac{\partial j(x)}{\partial x}\zeta_1 \tag{11}$$

After substitution of Eqs. (8) and (9) to Eq. (4), taking into account Eq. (10) and the fact that for $v_0$ and ζ expression Eq. (4) is identity, one can obtain an equation for nonstationary addition for flow velocity:

$$\frac{\partial v_1}{\partial t} + v_0\frac{\partial v_1}{\partial x} + v_1\frac{\partial v_0}{\partial x} = -\frac{\sigma}{\rho}\frac{\partial^3 \zeta_1}{\partial x^3} + \frac{\sigma}{\rho b^3}\frac{\zeta \partial \zeta_1}{\partial x} + \frac{\sigma}{\rho b^3}\frac{\zeta_1 \partial \zeta}{\partial x} - 3v\frac{v_1}{H^2} \tag{12}$$

By differentiating this equation with respect to (x), taking into account Eq. (11), giving similar and neglecting small terms, we arrive to an equation that describes the dynamic behavior of the excess of the growing surface over a stationary value:

$$\frac{\partial^2 \zeta_1}{\partial t^2} = \frac{\sigma H}{\rho}\frac{\partial^4 \zeta_1}{\partial x^4} - \frac{\sigma H^2}{2\rho b^3}\frac{\partial^2 \zeta_1}{\partial x^2} - \frac{\partial \zeta_1}{\partial x}\left(2\frac{\sigma H^2}{\rho b^3 L} - \frac{v_0}{\rho}\frac{\partial j}{\partial z}\right) + \zeta_1\frac{\partial j}{\partial z}\left(\frac{3v}{H^2\rho} + \frac{1}{\rho}\frac{\partial v_0}{\partial x}\right) \tag{13}$$

where L is the length of the melt pool, which is determined from the solution of the heat task.

We use the linear theory of stability and look for the solution of this equation in the form $\zeta_1 = \zeta_0 \exp(i(\omega t - kx))$, where $\zeta_0$ is the constant amplitude and ω in turn can be represented as $\omega = \Omega + i\gamma$, where Ω is the true frequency and γ is the increment (or decrement) of oscillations. Substituting these projects into Eq. (13), we obtain the characteristic equation, which, by neglecting the short-wave capillary ripple in the first approximation, the effect of the viscosity of the melt and the change in its flow velocity due to the thermocapillary effect, we obtain:

$$\Omega \approx \sqrt{\frac{\sigma}{2\rho}}\frac{\mathrm{Hk}}{\mathrm{b}^{\frac{3}{2}}}, \tag{14}$$

$$\gamma = -\frac{\mathrm{b}^{\frac{3}{2}}}{\sqrt{\frac{\sigma}{2\rho}}\mathrm{H}}\left(2\frac{\sigma \mathrm{H}^2}{\rho \mathrm{b}^3 \mathrm{L}} - \frac{\mathrm{v}_0}{\rho}\frac{\partial j}{\partial z}\right) \tag{14}$$

Thus, we come to the conclusion that, for γ <0, an oscillatory instability with frequency Ω and an increment γ occurs at the surface and for γ > 0 the oscillations will decay with the decrement γ. The condition of stability, obviously, is the fulfillment of the inequality:

$$2\frac{\sigma H^2}{v_0 b^3 L} < \frac{\partial j}{\partial z} \tag{15}$$

Thus, the critical value determining the stability (or instability) of the process of growing is the magnitude of the gradient of the particle flux density in the gas-powder jet along the normal to

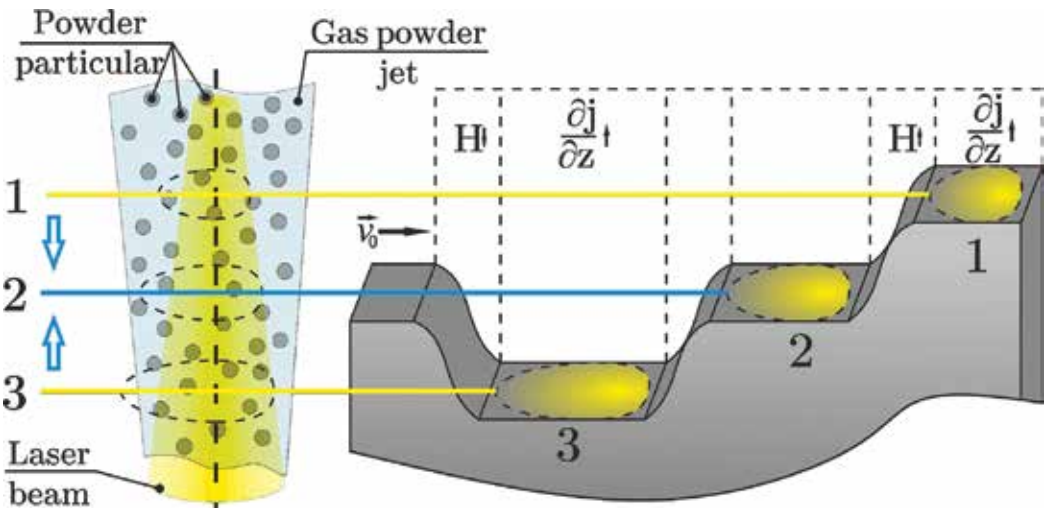


**Figure 2.** Scheme of stabilization process.

the growing surface. This fact is easy to understand—to stabilize the position of the surface, it is necessary that when it moves upward relative to a stationary value, it would fall under a less dense stream of particles, which would reduce the thickness of the deposited layer, and with shifts downward, under a denser flow, which would increase its thickness and, accordingly, would extinguish the perturbations that arise, as shown in **Figure 2**.

Obviously, for the stability of the process, it is also necessary that the length of the zone in which condition Eq. (15) is satisfied should be greater than the thickness of the layer deposited in one pass. In quantitative analysis, it should also be taken into account that not all particles adhere to the growing surface, so it is necessary to have a gradient value somewhat larger than that given by expression Eq. (15). Thus, a linear analysis of the stability of the process of direct laser deposition process allows us to conclude that stable growth is possible only at the position of the grown surface above the waist of the gas-powder jet, and the necessary condition for stability is the fulfillment of inequality Eq. (15).

## 3. Technology and equipment of direct laser deposition process

Direct laser deposition technology makes it possible to create complex parts and structures in a single technological step without the use of additional equipment, rigging, and adjustment of equipment [8, 21]. It is a complex technology, which is characterized by a multitude of process parameters. All the variety of parameters can be divided into managed and unmanaged [22]. Managed factors include process parameters such as laser power, nozzle type, traverse speed, powder feeding, spot diameter, layer height, powder fraction, selectable path, and rowing thick walls; it is also necessary to take into account the value of their overlap. Process could proceed in high purity Ar atmosphere for sensitive materials as titanium alloys. Also it is possible to get product under local protective atmosphere for less sensitive materials like some stainless steels. Uncontrollable factors include environmental pressure and other physical

conditions of the environment and quality of the raw powder materials. Especially it is necessary to take into account the thermophysical and technological properties of powder alloys.

Direct laser deposition is a multiparameter process; therefore the results of the process are affected by a complex of technological parameters [8, 23]. Among these parameters, it is possible to identify the main characteristics, which primary determine the course of the process [24]. The basic part of process parameters is described in **Table 1**, where the first four points are the main parameters.

On the basis of theoretical and experimental studies, equipment (**Figure 3**) was developed, which realizes DLD process. This is the first Russian equipment for realization of direct laser deposition technology.

The technology realized with this equipment solves a number of problems for modern engineering, improves process efficiency by 10 times, and reduces the cost of manufacturing parts by 3–5 times. Benefits of implementing the DLD are:

- Productivity of manufacturing parts with complex shapes from intractable materials increases.
- Full automation and "digitalization" of manufacturing.
- Raw material consumption decreases.
- Cost saving.
- Enhancement of technological and engineering capabilities.

The equipment is universal, and based on the principle of modular construction, without using accessory devices and bed structures, it is possible to obtain details of any designs and complexity at the request of the customer. The developed equipment can be operated in a chamber filled with protective gas, which completely eliminates the oxidation of metallic

| Process parameters | Productivity | Process stability | Usage rate | Roughness | Depth penetration |
|---|---|---|---|---|---|
| Laser power | Minor | Minor | Major | Minor | Major |
| Spot diameter | Major | Minor | Major | Minor | Major |
| Traverse speed | Major | Major | Major | Minor | Major |
| Powder feeding | Major | Major | Minor | Minor | Major |
| Layer height | Minor | Major | Minor | Major | Minor |
| Shielding gas rate | — | — | Major | Minor | — |
| Powder fraction | Minor | — | Major | Major | — |
| Distance between Nozzle and focus of gas-powder jet | Major | Major | Major | Minor | Minor |

**Table 1.** Process parameters of direct laser deposition technology.

**Figure 3.** Developed equipment for realization of DLD technology.

materials. A technological tool that combines a laser optical head and a powder nozzle is mounted on an industrial robotic manipulator [23]. As a result, the maximum size of the manufactured product is unlimited. The positioner table used for moving the product is also engaged to increase the technology's capabilities.

During the development of the equipment, special attention was paid to the design of the nozzle [24, 25]. It forms a gas-powder jet and thus has determining effect on DLD process. In the investigations, two types of nozzles were used (**Figure 4**): axisymmetric (or coaxial) and axially asymmetric (lateral or non-axial).

The main disadvantage of the lateral nozzle is shape constancy of deposited layer only in one direction, for example, straight line with moving laser head or the body of rotation with rotating substrate (**Figure 4a**). Therefore, despite its high productivity, it is almost used in the manufacture of equipment. For the developed equipment, the four-jet and annular gap powder nozzles were used.

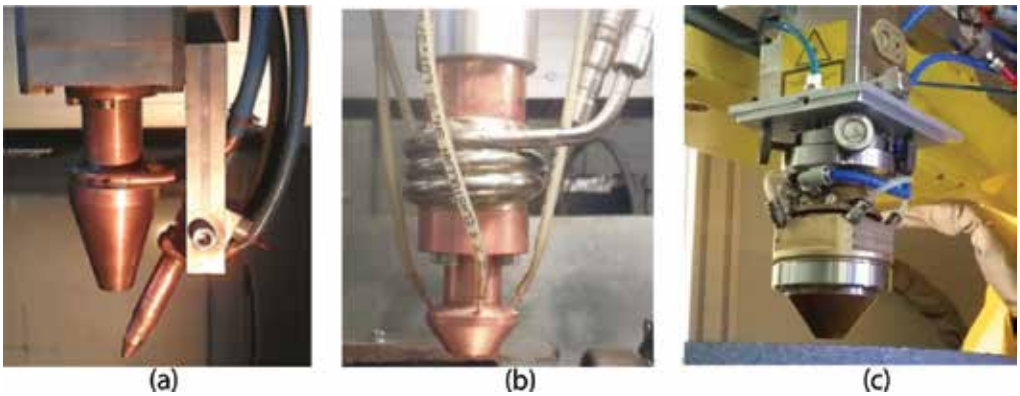


**Figure 4.** Lateral nozzle (a), coaxial four-jet nozzle (b), and coaxial annular gap nozzle (c).

Technological heads equipped with coaxial nozzles are characterized by independence of technological parameters from the direction of tool movement. This allows using complex processing trajectories and obtaining products with complex geometry. Multiple jet nozzles have from three up to six separate channels, which form powder jets. Its design is more complex but allows more flexibility for powder jet control (**Figure 4b**). During processing, the junction area of jets is located near molten pool, which is formed by a laser beam passing through the central hole of the nozzle. Annular gap nozzles are more technologically advanced (**Figure 4c**). Gas-powder jet is supplied through a gap between two conical surfaces that direct and focus it. Due to the uniform distribution of the powder along the circumference of the annular gap, a high degree of symmetry and isotropy with respect to the direction of motion is achieved. The developed nozzles were used to make a number of machines that realize DLD process.

As a result of the theoretical, technological, and design work, a general principle of constructing the equipment was carried out (**Figure 5**).

Below the components of the complex for the implementation of the direct laser deposition process are listed:

1. The two-axis positioner
2. Working chamber
3. Laser head
4. The robotic manipulator
5. Preparation and supplying gas system
6. Gas cleaning and drying device
7. The fiber laser
8. Chiller

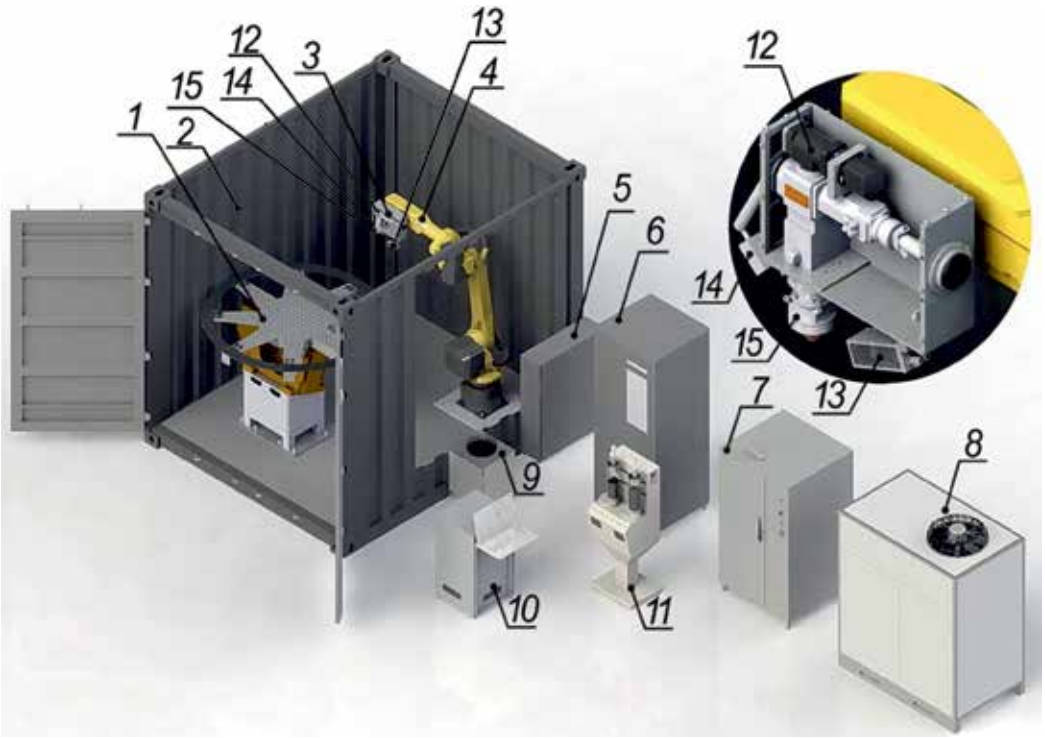


**Figure 5.** The general scheme of equipment for DLD process implementation.

**9.** Cooling system

**10.** Control stand

**11.** The powder feeder

**12.** Control system

**13.** Video surveillance system

**14.** Monitoring system for processing area

**15.** Nozzle

The developed technological complex allowed to manufacture products with a traverse speed of up to 60 mm/s and a productivity of 2.5 kg/h.

## 4. Structure and properties of manufactured products

As a result of the theoretical and experimental studies, the parameters of the process for manufacturing products are carried out, using different metal alloys, which are based on

nickel, iron, and titanium [8, 21, 26, 27]. Using optimal parameters of DLD process allows preparing samples without such macrodefects as cracks and pores (**Figure 6**).

However, in case of violation of the selected modes, porosity, cracks, and lack of fusion may appear. The main reason for the occurrence of large pores (more than 100 μm) is the low quality of the shielding gas or work with local protection. Smaller pores could appear because of low quality of powder [21]. Powders obtained by plasma rotating electrode process (PREP) allow to produce samples of lower porosity as compared with the gas atomization. Powders obtained by gas atomization may contain internal pores. It is also possible for them to form with improperly selected modes, which lead to too high cooling rates. Examples of pores in the samples are shown in **Figure 7**.

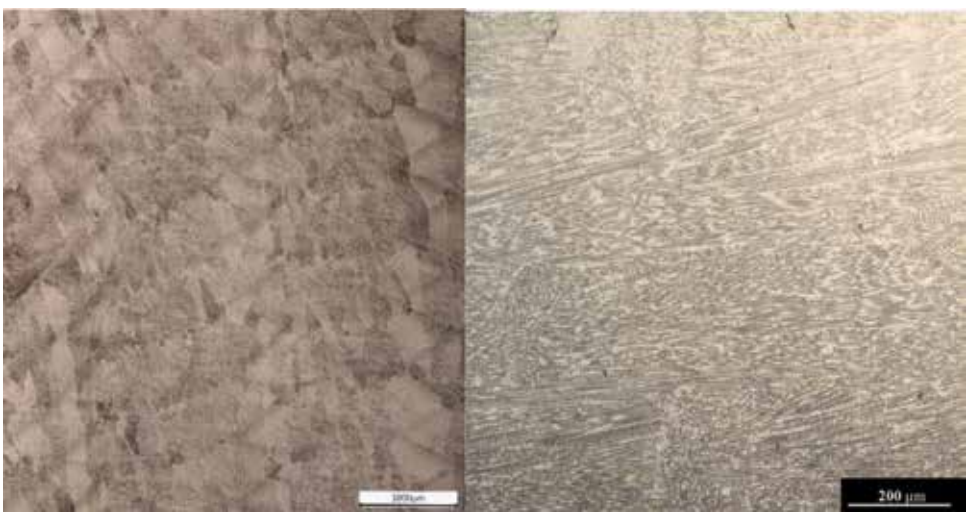


**Figure 6.** Deposited samples without macrodefects: left—Ti-based alloy and right—Ni-based alloy.

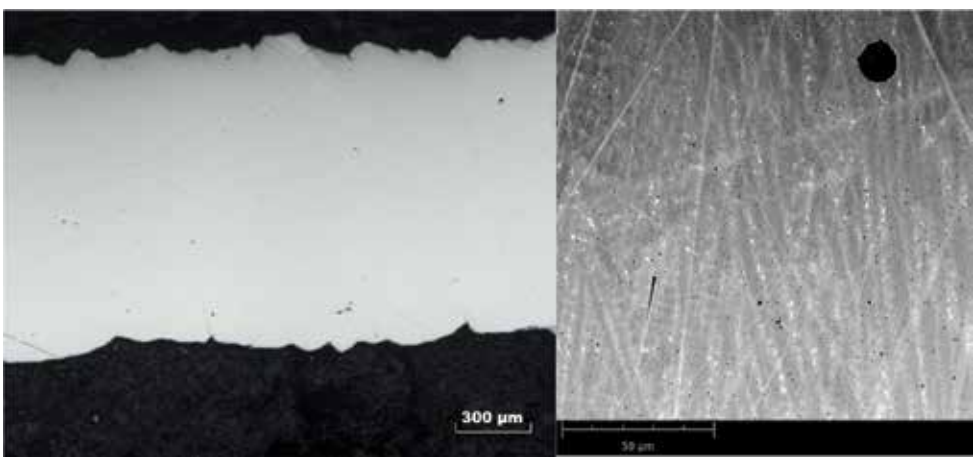


**Figure 7.** Pores in samples, material Ni-based alloy Inconel 625.

Most often defects are lack of fusion, which have a more negative effect on mechanical characteristics than pores. Small lack of fusion results because of using oxidized powder or contaminated powder. Also, their number increases significantly using local protection, rather than full filling the chamber with shielding gas. Examples of lack of fusion are shown in **Figure 8**.

Lack of fusion is also detected at the deposition of thick-walled products. The appearance of such lack of fusion is due to the lack of energy. They are found in the samples grown at low power, a small size of spot diameter. The size of the overlapping layers also affects, but it has less influence and strongly depends on spot diameter. In **Figure 9** lacks of fusion in thick-walled samples are shown.

In the process of deposition, cracks can also appear, especially in those nickel alloys that are prone to their appearance. For all products obtained by direct laser deposition process, the cracks are an impermissible defect; such products are rejected.

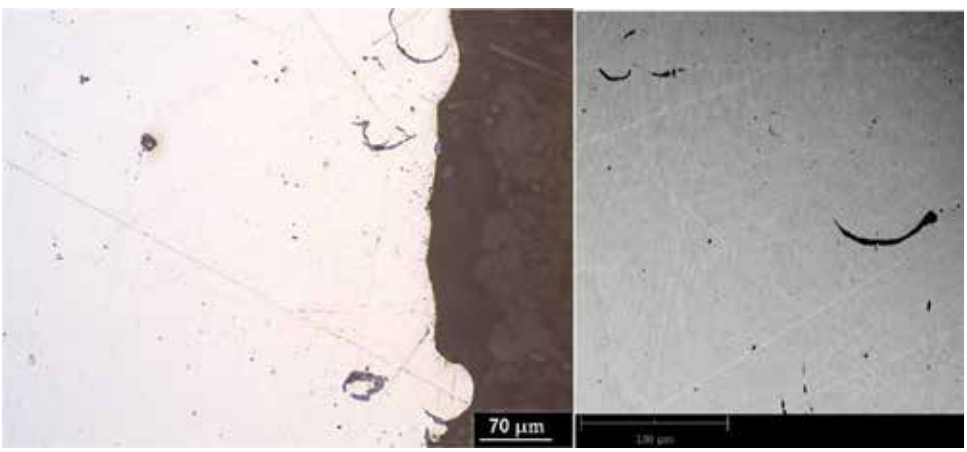


**Figure 8.** Lacks of fusion in samples, material Ni-based alloy Inconel 625.

**Figure 9.** Lacks of fusion in thick-walled sample, material Ti-based alloy Grade 5.

The microstructure of the samples obtained has a finely dispersed, predominantly cast structure. Features of structure formation for the different metal alloys using this technology were studied in detail by the authors. The results of research presented by the

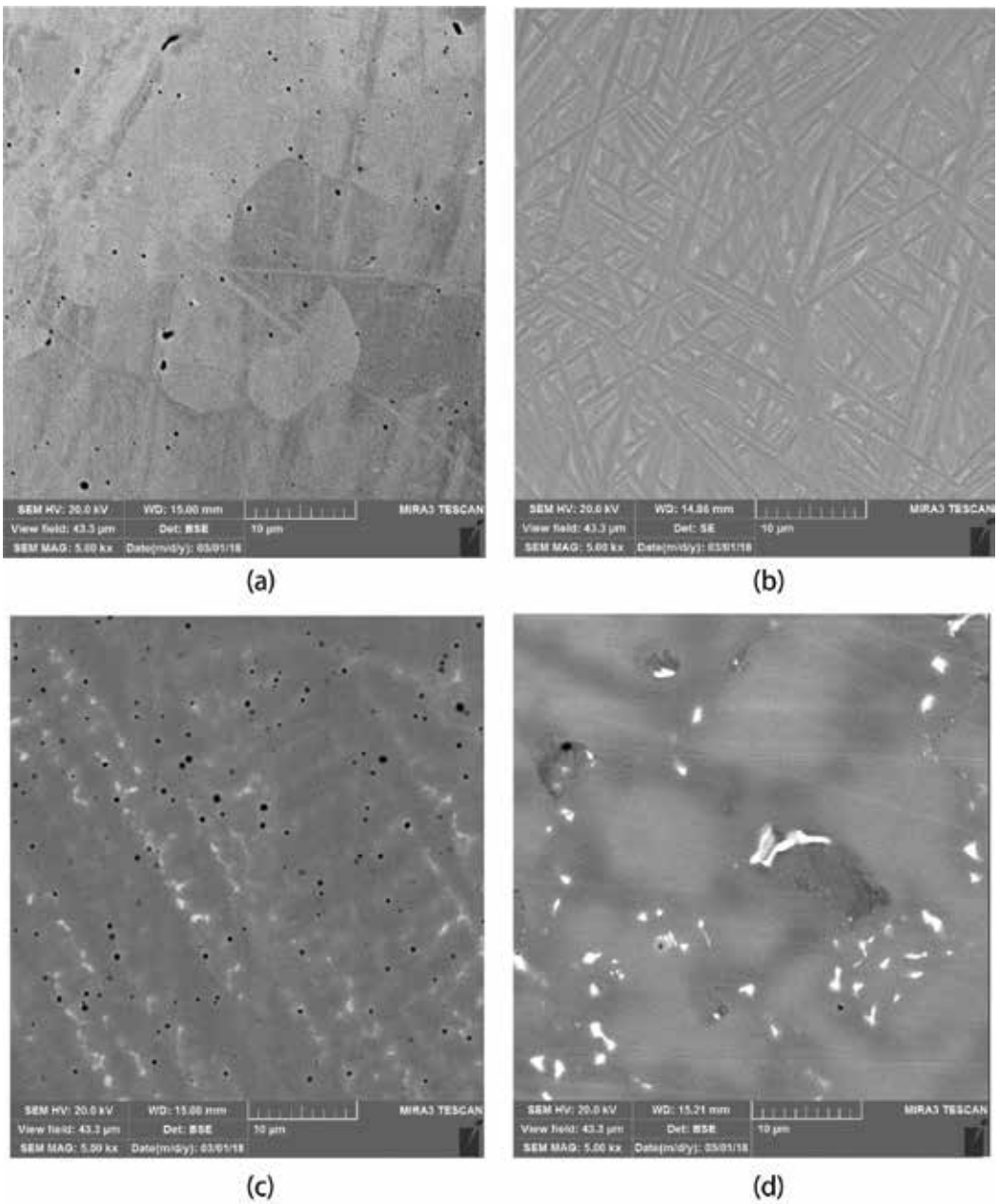


**Figure 10.** Microstructure of deposited samples: (a) 316 L steel, (b) Ti-based alloy analog Grade 35, (c) Inconel 625, and (d) Ni-based alloy analogue Mar-M200.

| Material | Yield strength (0,2% Offset), MPa | Ultimate Tensile strength, MPa | Elongation, % |
|---|---|---|---|
| Inconel 625, DLD | 489 | 865 | 28.5 |
| Inconel 625, cast [31] | 310 | 800 | 25 |
| Analogue Mar-M200 alloy, DLD | 1046 | 1353 | 11.5 |
| Analogue Mar-M200 alloy, cast | 1075 | 1108 | 2.9 |
| Analogue Grade 35 alloy, DLD | 882 | 968 | 6.6 |
| Analogue Grade 35 alloy, cast | 876 | 951 | 6.4 |
| Analogue Grade 5 alloy, DLD | 1040 | 1120 | 8 |
| Analogue Grade 5 alloy, cast | — | 880 | 4 |
| 316 L, DLD | 272.5 | 570 | 41 |
| 316 L, cast [31] | 177 | 441 | 25 |

**Table 2.** Mechanical characteristics of deposited and cast samples.

authors in the articles [26–30]. In **Figure 10** microstructure of different alloys is presented.

Comparing with cast samples, the products that are manufactured by direct laser deposition technology have ultrafine structure. It provides high level of mechanical characteristics (**Table 2**). Mechanical tests were conducted for a greater number of different alloys; the main results are given in **Table 2**. The materials were tested on uniaxial tension; universal testing machine Zwick/Roell Z250 Allround was used.

## 5. Conclusions

The results of researches show that the developed technology of direct laser deposition, in spite of its technological complexity, can replace the currently used technologies, providing multiple increases in productivity and material saving.

- Direct laser deposition is technology for manufacturing of details with complex form from powder materials using 3D model. It has potential use for different materials in a single part and obtaining details with gradient properties. Using equipment, which realizes this technology, it is possible to produce details of any size.
- The process productivity is 10 times higher in comparison with layered synthesis technologies like SLM. Mechanical properties of the obtained products are much higher than the characteristics of the cast metal; there are no pores and cracks and is no lack of fusion.
- This equipment has a maximum capacity in comparison with existing analogues: up to 2.5 kg/h for metallic materials.
- This is the first Russian technology and equipment for the implementation of additive production.

## Author details

Gleb Turichin* and Olga Klimova-Korsmik

*Address all correspondence to: gleb@ltc.ru

State Marine Technical University, Saint-Petersburg, Russian Federation

## References

[1] Gu D. New metallic materials development by laser additive manufacturing. In: Surface Engineering. New-York: Elsevier Ltd; 2015. pp. 163-180

[2] Kianiana B, Tavassoli S, Larsson TC. The role of additive manufacturing technology in job creation: An exploratory case study of suppliers of additive manufacturing in Sweden. In: Procedia CIRP, 12th Global Conference on Sustainable Manufacturing—Emerging Potentials, Vol. 26; 2015. pp. 93-98

[3] Gress DR, Kalafsky RV. Geographies of production in 3D: Theoretical and research implications stemming from additive manufacturing. Geoforum. 2015;**60**:43-52

[4] Siemieniuch CE, Sinclair MA, de Henshaw MJC. Global drivers, sustainable manufacturing and systems ergonomics. Applied Ergonomics. 2015;**51**:104-119

[5] Eyers DR, Potter AT. Industrial additive manufacturing: A manufacturing systems perspective. Computers in Industry. 2017;**92–93**:208-218

[6] Liverani E, Toschi S, Ceschini L, Fortunato A. Effect of selective laser melting (SLM) process parameters on microstructure and mechanical properties of 316L austenitic stainless steel. Journal of Materials Processing Technology. 2017;**249**:255-263

[7] Olakanmi EO, Cochrane RF, Dalgarno KW. A review on selective laser sintering/melting (SLS/SLM) of aluminum alloy powders: Processing, microstructure, and properties. Progress in Materials Science. 2015;**74**:401-477

[8] Turichin GA, Klimova OG, Zemlyakov EV, Babkin KD, Kolodyazhnyy DY, Shamray FA, Travyanov AY, Petrovskiy PV. Technological aspects of high speed direct laser deposition based on heterophase powder metallurgy. Physics Procedia. 2015;**78**:397-406

[9] Wilson MJ, Piya C, Shin YC, Zhao F, Ramani K. Remanufacturing of turbine blades by laser direct deposition with its energy and environmental impact analysis. Journal of Cleaner Production. 2014;**80**:170-178

[10] Thompsona SM, Bianc L, Shamsaeia N, Yadollahi A. An overview of direct laser deposition for additive manufacturing; Part I: Transport phenomena, modeling and diagnostics. Additive Manufacturing. 2015;**8**:36-62

[11] Dutta B, Palaniswamy S, Choi J, Song LJ, Mazumder J. Additive manufacturing by direct metal deposition. Advanced Materials & Processing. 2011;**169**:33-36

[12] Renderos M, Girot F, Lamikiz A, Torregaray A, Saintier N. Ni based powder reconditioning and reuse for LMD process. Physics Procedia. 2016;**83**:769-777

[13] Wang Y, Tang H, Fang Y, Wang H. Microstructure and mechanical properties of hybrid fabricated 1Cr12Ni2WMoVNb steel by laser melting deposition. Chinese Journal of Aeronautics. 2013;**26**(2):481-486

[14] Saboori A, Gallo D, Biamino S, Fino P, Lombardi M. An overview of additive manufacturing of titanium components by directed energy deposition: Microstructure and mechanical properties. Applied Sciences. 2017;**7**:883-906

[15] Zhong C, Gasser A, Kittel J, Wissenbach K, Poprawe R. Improvement of material performance of Inconel 718 formed by high deposition-rate laser metal deposition. Materials and Design. 2016;**98**:128-134

[16] Turichin GA. Hydrodynamic stability aspects of gas-vapour channel at energy beam welding. Physics and Chemistry of Metal Treatment. 1996;**4**:74-81

[17] Reisgen U, Schleser M, Abdurakhmanov A, Turichin GA, Valdaytseva EA, Bach F-W, Hassel T, Beniyash A. Study of factors affecting defect formation of the weld seam at electron-beam welding in outer space. Avtomaticheskaya Svarka. 2012;**2**:13-20

[18] Matsunawa A, Kim J-D, Seto N, Mizutani M, Katayama S. Dynamics of keyhole and molten pool in laser welding. Journal of Laser Applications. 1998;**10**(6):247-254

[19] Raisgen U, Schlezer M, Abdurachmanov A, Turichin G, Valdaytseva E, Bach F-W, Hassel T, Banyash A. Investigation of factors influencing the formation of weld defects in non-vacuum electron beam welding. Paton Welding Journal. 2012;**2**:11-18

[20] Kumar A, Roy S. Effect of three-dimensional melt pool convection on process characteristics during laser cladding. Computational Materials Science. 2009;**46**(2):495-506

[21] Glukhov V, Turichin G, Klimova-Korsmik O, Zemlyakov E, Babkin K. Quality management of metal products prepared by high-speed direct laser deposition technology. Key Engineering Materials. 2016;**684**:461-467

[22] Turichin GA, Somonov VV, Klimova OG. Investigation and modeling of the process of formation of the pad weld and its microstructure during laser cladding by radiation of high power fiber laser. Applied Mechanics and Materials. 2014;**682**:160-165

[23] Turichin GA, Somonov VV, Babkin KD, Zemlyakov EV, Klimova OG. High-speed direct laser deposition: Technology, equipment and material. In: IOP Conference Series: Materials Science and Engineering Current Problems and Solutions, Vol. 125; 2016. p. 012009

[24] Turichin G, Zemlyakov E, Klimova O, Babkin K. Hydrodynamic instability in high-speed direct laser deposition for additive manufacturing. Physics Procedia. 2016;**83**:674-683

[25] Korsmik RS, Turichin GA, Babkin KD. Laser cladding technological machine. Investigation of efficiency of various nozzles design. Journal of Physics: Conference Series. 2017; **857**:4

[26] Sklyar MO, Turichin GA, Klimova OG, Zotov OG, Topalov IK. Microstructure of 316L stainless steel components produced by direct laser deposition. Steel in Translation. 2016; **46**(12):883-887

[27] Sklyar MO, Klimova-Korsmik OG, Cheverikin VV. Formation structure and properties of parts from titanium alloys produced by direct laser deposition. Solid State Phenomena. 2017;**265**:535-541

[28] Klimova-Korsmik OG, Turichin GA, Zemlyakov EV, Babkin KD, Travyanov AY, Petrovskiy PV. Structure formation in Ni superalloys during high-speed direct laser deposition. Physics Procedia. 2016;**83**:716-722

[29] Klimova-Korsmik OG, Turichin GA, Zemlyakov EV, Babkin KD, Petrovskiy PV, Travyanov AY. Structure formation in Ni superalloys during high-speed direct laser deposition. Materials Science Forum. 2017;**879**:978-983

[30] Turichin GA, Travyanov AY, Petrovskiy PV, Zemlyakov EV, Kovac M, Vondracek S, Kondratiev A, Khvan AV, Cheverikin VV, Ivanov DO, Bazhenova IA, Dinsdale AT. Prediction of solidification behaviour and microstructure of Ni based alloys obtained by casting and direct additive laser growth. Materials Science and Technology. 2016;**32**(8): 746-751

[31] DebRoy T, Wei HL, Zuback JS, Mukherjee T, Elmer JW, Milewski JO, Beese AM, Wilson-Heid A, De A, Zhang W. Additive manufacturing of metallic components—Process, structure and properties. Progress in Materials Science. 2018;**92**:112-224

Chapter 5

# Processing Parameters for Selective Laser Sintering or Melting of Oxide Ceramics

Haidong Zhang and Saniya LeBlanc

Additional information is available at the end of the chapter

http://dx.doi.org/10.5772/intechopen.75832

**Abstract**

In this chapter, we present a detailed introduction to the factors which influence laser powder bed fusion (LPBF) on oxide ceramics. These factors can be in general divided in three main categories: laser-related factors (wavelength, power, scanning speed, hatch distance, scan pattern, beam diameter, etc.), powder- and material-related factors (flowability, size distribution, shape, powder deposition, thickness of deposited layers, etc.), and other factors (pre- or post-processing, inert gas atmosphere, etc.). The process parameters directly affect the amount of energy delivered to the surface of the thin layer and the energy density absorbed by the powders; therefore, decide the physical and mechanical properties of the built parts, such as relative density, porosity, surface roughness, dimensional accuracy, strength, etc. The parameter-property relation is hence reviewed for the most studied oxide ceramic materials, including families from alumina, silica, and some ceramic mixtures. Among those parameters, reducing temperature gradient which decreases the thermal stresses is one of the key factors to improve the ceramic quality. Although realizing crack-free ceramics combined with a smooth surface is still a major challenge, through optimizing the parameters, it is possible for LPBF processed ceramic parts to achieve properties close to those of conventionally produced ceramics.

**Keywords:** LPBF, SLM, SLS, ceramic, additive manufacturing, AM, processing parameters

## 1. Introduction

Laser powder bed fusion (LPBF) is an additive manufacturing process that uses a laser beam to fuse powder particles in a layer-by-layer fashion, which allows production of complex three-dimensional (3D) structures. LPBF includes selective laser melting (SLM), where powder is fully melted, and selective laser sintering (SLS) for other cases such as solid state sintering,

liquid state sintering, and partial melting [1]. The main advantages of LPBF are time efficiency and the capability to build geometries that would be unattainable through traditional techniques. LPBF has revolutionized manufacturing by offering great design freedom for 3D structures to be built directly from feedstock powders without additional processing. Introduced in the late 1980–1990s [2–4], the LPBF process was initially applied to metals, and later to polymers, ceramics, and recently, to semiconductors [5, 6].

This chapter focuses on laser powder bed fusion of ceramic materials. Typical ceramics are strongly bonded inorganic and non-metallic solids such as crystalline oxide, nitride and carbide materials. Sometimes non-crystalline or partially crystalline glass is also referred to as glass-ceramic. Ceramics feature excellent strength and hardness, good abrasion resistance, high melting temperature, high chemical stability, low ductility, and low electrical and thermal conductivities.

A classification of processing techniques for ceramic materials is summarized in **Figure 1**. Ceramics cannot be shaped by the conventional forging and machining formation. They are usually formed through multi-step processes [7]. The shaping process begins with powder mixtures that contain binders and stabilizers. The next step is shape forming which includes extrusion, slip casting, pressing, tape casting, and injection molding. The last step is sintering

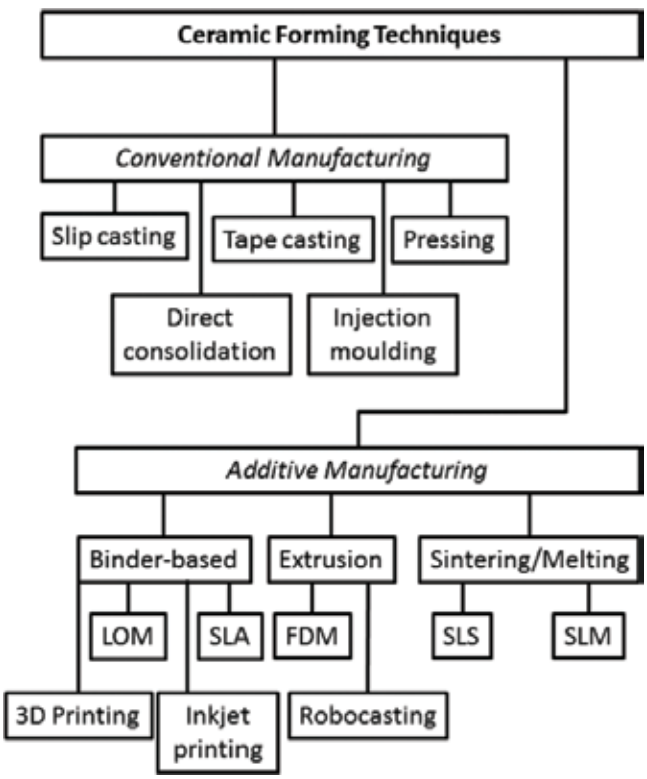


**Figure 1.** Classification of processing techniques for ceramic materials. Reprinted from [14], with permission of Taylor & Francis Group, LLC.

http://dx.doi.org/10.5772/intechopen.75832

at high temperatures. These traditional processes involve molding and tooling, have high cost, and limit the device geometry that can be produced.

Additive manufacturing on ceramics has been developed in order to overcome some of subtractive manufacturing's shortcomings, especially with respect to high tool wear, size shrinkage, and difficulty creating complex structures. Additive manufacturing includes binder-based, extrusion-based, and powder-based (LPBF) techniques. Among these, LPBF offers the opportunity for fast and direct fusion without costly post treatments and toxic binders which are often required by other techniques. LPBF-produced ceramic parts have potential to impact several applications such as medical and dental components [8–10], metal casting molds [11], thin wall structures, turbine blades, nozzles [12], and thermal or electrical insulation [13].

While LPBF enables rapid manufacturing of ceramic parts with complex structures, there are two technical limitations. First, ceramic powders, as compared with metals, often flow poorly, resulting in imperfect spreading on the powder bed surface. Second, and more importantly, highly localized heating combined with ceramics' intrinsic low thermal conductivity often leads to large temperature gradients that result in residual stresses and deformation. Combined with ceramics' brittleness, the two limitations can result in cracking, lack of fusion, rough surfaces, porosity and less than full density. Due to these challenges, current results for LPBF of ceramics are far from satisfactory.

There are several excellent reviews for SLS/SLM of ceramics [7, 10, 14–23]. However, many of the SLS/SLM processing factors such as laser power, layer thickness, or powder bed preheating are still poorly investigated or need to undergo a systematic review. Key insights about process parameters have not been transferred into industry. This chapter provides an introduction to LPBF of common ceramics. The chapter is organized as follows. The first part introduces the main procedure and tools for LBPF. Following that, the second section introduces laser parameters, powder parameters, and other factors for the LPBF process, as well as a few physical properties concerned in ceramic applications. The third part discusses how the processing parameters and other factors influence the physical properties of the manufactured parts as well as the general rules for parameter selections. Then the fourth part illustrates some of the most widely studied ceramic materials processed by LPBF, including the state of art achievements. The final two sections summarize the perspectives and the common LPBF challenges for ceramics.

## 2. Processing parameters and characterization

A basic LPBF system consists of three parts: laser system, powder bed, and spreading system. The laser system includes a laser and a scanner. In order to heat and melt the material, the laser beam has to focus onto the powder surface and be absorbed by the material. The scanner enables the laser to move in a two dimensional plane. The powder bed is a container for the ceramic powders; it usually has adjustable height to allow laser focusing on the newly formed surface. The spreading system often includes a slot feeder to spread fresh powders and a roller or a scraper blade to flatten the surface.

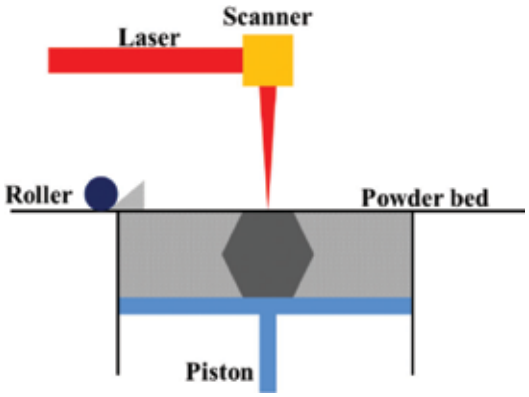


**Figure 2.** Illustration for basic LPBF procedure.

A typical LPBF setup is illustrated in **Figure 2**. Powders are spread onto the building platform and flattened by a roller, a scraper blade or a combination moving over the surface. The new powder surface moves down one layer thickness to maintain the desired laser focus. The 3D part is decomposed to a number of planes to be processed; each plane consists of a series of basic elements of laser scanning, called vectors. The scan pattern, or the orientation and distance between vectors, is pre-designed. The laser then scans the flat surface of loose or slightly compacted powders following such patterns and selectively melts the illuminated powders. Those powders are quickly solidified after the laser moves away. After that, another layer of powder is deposited and welded, and the process is repeated until a 3D structure in the desired shape and thickness is formed. During the process, unprocessed powder from each layer fills the empty space in the fabrication chamber and supports the part which has been built; afterwards, this powder is recycled. The basic process flow chart is shown in **Figure 3**. Depending on the materials to be processed, the fabrication chamber is sometimes heated and maintained at a certain temperature to help the sintering or melting process. The Renishaw-AM125 (Renishaw, Wotton-under-Edge, Gloucestershire, UK), and SLM@250$^{HL}$ (SLM Solutions GmbH) are two examples of commercial additive manufacturing machines used to process ceramic powders.

LPBF can be broadly classified in two types: direct and indirect, depending on whether a binder material is used. An indirect process either mixes binder materials with ceramics or coats the ceramics with a polymer. The mixture can be used as dry powders or as wet slurry from a suspended liquid. The binder materials melt and consolidate the ceramic powders during laser scanning. Then a de-binding process removes the binder, and further sintering of the ceramic part is usually required to increase the final part density. In the direct process, ceramic objects are created by sintering or melting without the aid of any binders. Because of the high melting temperatures of ceramics, indirect processing of ceramics is most common [24].

### 2.1. Laser parameters

During the LPBF process, many factors affect the final part. The main laser parameters include wavelength, power, scanning speed, hatch distance, scan pattern, vector length [12], ratio of length to width [25], scan angle [25], beam spatial distribution [26], beam spot size [27], point

http://dx.doi.org/10.5772/intechopen.75832

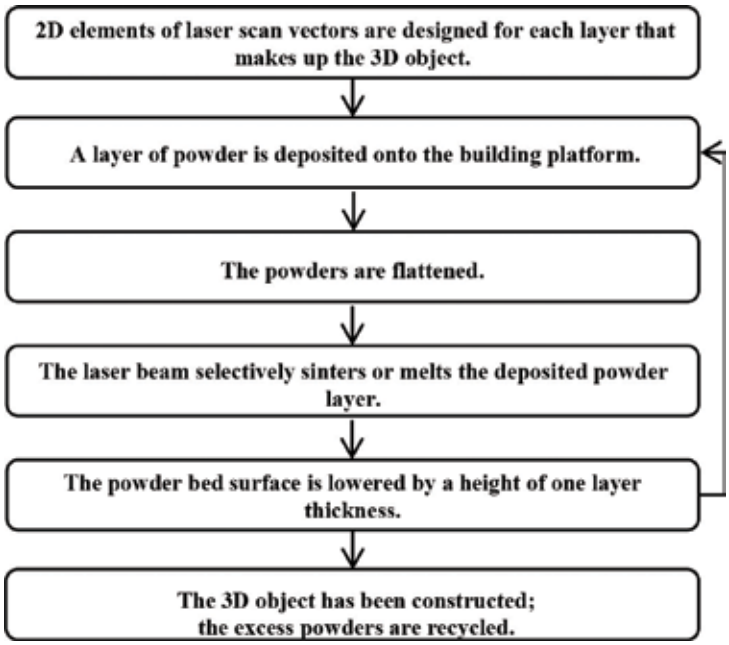


**Figure 3.** Basic process flow chart for LPBF manufacturing.

overlapping [28], and continuous or pulsed laser operation. Although most of the parameters have an effect on some aspects of the final product, currently there are not enough experimental data or calculations to relate all the factors. Some parameters are not always adjustable, for example, the wavelength of a certain laser system. As a result, only some of the most important parameters will be discussed. Key laser parameters are shown in **Figure 4**.

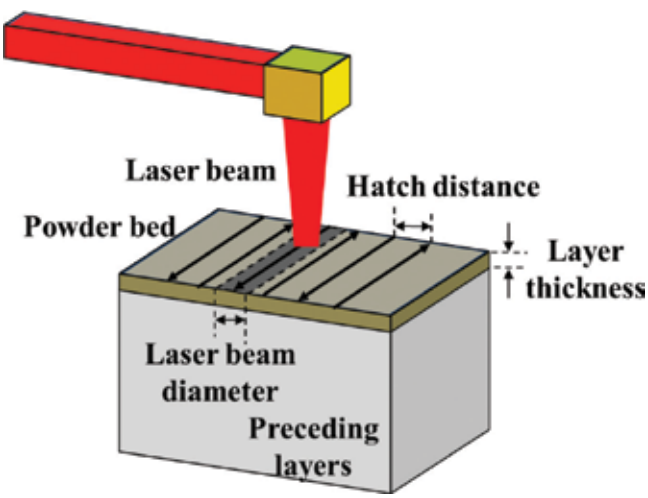


**Figure 4.** SLM process parameters: laser power, scanning speed, hatch spacing, and layer thickness.

| Materials | Absorptance of Nd-YAG laser (λ = 1.06 μm) | Absorptance of $CO_2$ laser (λ = 10.6 μm) |
|---|---|---|
| ZnO | 0.02 | 0.94 |
| $Al_2O_3$ | 0.03 | 0.96 |
| $SiO_2$ | 0.04 | 0.96 |
| BaO | 0.04 | 0.92 |
| SnO | 0.05 | 0.95 |
| CuO | 0.11 | 0.76 |
| SiC | 0.78 | 0.66 |
| $Cr_3C_2$ | 0.81 | 0.7 |
| TiC | 0.82 | 0.46 |
| WC | 0.82 | 0.48 |

**Table 1.** Optical absorptance for materials. The data presented here are from those presented in the original source [39].

*2.1.1. Laser selection, wavelength (λ), operation mode, and beam diameter (σ)*

Laser and powder interactions are fundamental to the LPBF process, and laser selection depends on materials [29–31]. Due to light-matter interactions, materials only absorb light energy for certain wavelengths based on the optical properties. Optical absorption coefficients for some ceramic materials are listed in **Table 1**. Common oxide ceramics only weakly absorb in the near infrared region while carbide ceramics absorb the 1.06 μm wavelength. Therefore, the $CO_2$ laser ($\lambda \approx$ 10.6 μm) is better suited for oxide ceramics due to higher optical absorptivity, while Nd:YAG, Yb:YAG or Nd:YVO4 ($\lambda \approx$ 1.06 μm) lasers that are common in commercial selective laser melting machines are more suitable to metals and carbide ceramics. Nonetheless, the YAG laser is often applied to oxide ceramics due to its smaller spot size for higher dimensional accuracy, higher specific power, and larger parameter window [28, 32, 33]. The application of the 1.06 μm laser on oxide ceramics is possible because of two effects. First, the absorption for the powder format is usually much higher than the corresponding smooth bulk surfaces due to the multiple reflections effect [34–36]. For example, the optical absorption for alumina is increased to ~10% at ~1 μm [35, 37]. Second, impurities often increase the absorption and reduce the melting temperatures. While it is common to apply a continuous wave laser in the LPBF process, a pulsed laser can also be used [38]. Several additional laser parameters can be adjusted such as pulse durations, shapes and frequencies. It has been shown that those parameters affected the surface quality. Finally, the laser beam diameter or spot size (usually tens of micrometers in diameter) sets the theoretical limit of the spatial resolution although usually many other factors would prevent such a resolution.

*2.1.2. Laser power (*p*), scanning speed (*v*), hatch distance (*h*), and laser energy density (*E*)*

Laser power, scan speed, and hatch distance are the major adjustable parameters are for a laser system. Laser power and the movement of the focused laser spot onto the powder surface should be adjusted to provide enough heat to melt the powers. The hatch distance is the

distance between two neighboring melted lines or vectors; it is usually smaller than the laser spot size. The hatching distance and the spot size decide the overlapping percentage coverage. The three parameters often work together to transfer laser energy to the powder bed. For example, if the absorption coefficient is not very high, it may be compensated for by adjusting one or all of the three parameters. It was reported [40] that a combination of high laser power and low scanning speed helps to reduce balling—the formation of spheroidal beads during the LPBF process due to surface tension and insufficient wetting of the preceding layer [41, 42].

A common practice is to use laser energy density $E = \frac{p}{vh}$ (J/mm$^2$) [8, 43] or volumetric energy density $\frac{p}{vhd}$ (J/mm$^3$) [27, 44], or $\frac{p}{v\sigma d}$ (J/mm$^3$) [45], to represent the laser heating effect, where $E$ is the energy density and $d$ is the layer thickness. Sometimes line energy $\phi = \frac{p}{v}$ (J/mm) has been used instead [46].

#### *2.1.3. Scan pattern and point overlapping*

Scan pattern can be single-scan, repeated scan, or cross-scan, with or without contouring. The scan pattern should be chosen based on the material properties and can affect the surface roughness and the mechanical properties of the final product. For example, it was shown that the repeated scan pattern reduced balling [40]. It was reported that contouring helps to generate the same quality for the beginning and ending of scan lines [47]. Also, the contour forms a barrier that keeps the melt pool of the hatch from exceeding the specimen's boundaries [48]. The overlapping of the two parallel, consecutive laser scans is defined as $Ov = 1 - (h/\sigma)$ where h is the hatch distance and σ is the beam spot size [28]. There is an overlap of successive laser spots for $Ov > 0$ and no contact for $Ov < 0$.

### 2.2. Powder factors

Besides laser factors, powders are also critically affect the LPBF process. Powder size affects laser melting efficiency. Large particles generally reduce the pack density of the powder bed and also require more energy to melt. On the other hand, smaller particles tend to agglomerate, which makes it difficult for powder layering or coating. The typical particle size is in the range of a few to several hundred microns. The ability for powder flow is an important factor to decide the particle distribution on the powder bed. Good powder flow is required to form a flat powder surface and a uniform thickness of powder layers, which are necessary to achieve uniform laser energy absorption. Particle morphology and size distribution affect the powder flow, for example, in general powders flow better with the increase of the sphericity and particle size for particles with a narrow size distribution [9, 12, 49]. The "flowability" in turn significantly affects packing efficiency, mechanical properties, and surface roughness. Powder composition, melting point, optical properties, and heat transfer properties also affect the choice of laser parameters and final product properties. Although these powder factors are important, systematic studies on them are lacking. The powder layer thickness is a very important factor, and it needs to be determined according to the laser beam penetration to the powder bed. Layer thickness also affects the energy density to be applied and can affect the surface roughness [50].

### 2.3. Other factors

Other factors also significantly affect the LPBF process, including pre- or post-processing, secondary laser assistant, application of protective gas atmosphere, etc. The preheating decides the temperature of the powder bed and is particularly important in the case where binders are used since it affects the wetting and spreading properties. Oxidation usually happens if the process is not in an oxygen-deficit environment, which affects the materials' structure and properties.

The laser beam characteristics and scanning fashion, together with the optical and thermal properties of the powder layer, govern the balance between heating by the absorption of laser radiation and conductive thermal losses. The thermal absorption and dissipation dictate the temperature of the laser-powder interaction zone [51]. With appropriate combinations of laser parameters and proper powders, the interlayer bonding strength and the mechanical strength of the whole component can be improved [52].

### 2.4. Quality assessment

Depending on the purpose of applications, attributes of the final products are assessed to determine part quality. Critical attributes are porosity, relative density, surface roughness, dimensional accuracy, strength, micro hardness, and other mechanical properties.

Pores often form in the LPBF processed products. Porosity, the percentage of void space in a bulk material, is hence an important parameter for the laser treated materials. The porosity content can be determined by an image analysis method [53]. Relative density is the ratio of the LPBF-processed part density to the theoretical density of the bulk material. Relative density is a basic parameter of the product. Because of the direct relation between relative density and porosity, it is common to measure relative density instead of porosity since relative density is easier to measure.

Surface roughness measures the surface irregularities, often expressed as numeric parameters $R_a$ and $R_z$, where $R_a$ is the arithmetic mean deviation of the roughness profile, and $R_z$ is the maximum roughness, or the maximum height of the profile from peak to valley. LPBF of ceramics often leads to a poor surface finish and high roughness because the melt pool is large, and the molten material has low viscosity and thermal conductivity. It was shown that low viscosity large melt pool wet the powders outside the pool boundary, and led to large grains and rough surfaces [48, 54, 55].

Dimensional accuracy is the measure for the accuracy of the LPBF product to the expected parts. The material's strength is the measure to withstand an applied maximum stress without failure, including compressive, tensile, and shear strengths. Because of cracks and pores, LPBF ceramics have lower strength than their cast counterparts. An important indicator for the mechanical properties for the LPBF product is the bending strength. A positive linear relationship between bending strength and relative density has been reported [56], so relative density can be an indicator for bending strength. Hardness measures the material's ability to resist permanent plastic deformation.

http://dx.doi.org/10.5772/intechopen.75832

Using LPBF as the manufacturing technique, the important difference between ceramics and metals is that ceramic materials are particularly subject to cracks and delamination [21] due to the large thermal gradient resulting from ceramics' intrinsic very low thermal conductivities and very high melting temperatures. Compared to metals, the LPBF-produced ceramics often display lower relative density and rougher surface. While steels made by SLM process are often mechanically stronger than those made by casting [21], currently SLM-manufactured ceramics are almost always mechanically weaker than their counterparts made from conventional methods. Therefore, applying LPBF to ceramics generally presents more challenges than that to metals.

## 3. Principles for optimum SLM/SLS process

Both direct and indirect methods are capable of processing ceramics close to a full density. The advantage of the direct process method is that post-processing is not required for the parts manufactured, and it is possible to directly manufacture near crack-free ceramic parts with high densities [9]. However, because of the very high melting point, it is common to coat the pure ceramic powder with binders, to make use of the existing or mixed absorption impurities, or to form some sort of low-melting point eutectics with several ceramics. In those cases, a post-processing thermal treatment is often necessary to obtain denser parts.

Both a $CO_2$ laser and a YAG laser can be used for processing ceramics. On the one hand, the longer wavelength $CO_2$ laser corresponds to higher optical absorptivity. On the other hand, the YAG laser yields better dimensional accuracy due to its much smaller laser spot size. However, in order to use the near-infrared laser, additive materials are often mixed with the ceramics to improve laser absorption. The additives are chosen to strongly absorb the laser beam but not to react with ceramics at high temperatures. Many materials can be used for such a purpose. For example, they can be low-melting-point polymers that are eventually burnt off or inorganic powders such as graphite, and sometimes the existing impurities can work as the absorption medium to increase the laser-material coupling.

A suitable setting of laser processing parameters can improve microstructures and the mechanical quality of the processed parts. However, optimizing one single parameter or process usually accompanies other disadvantages for the ceramic process. The choice of a process for a particular design requirement often involves a compromise of other properties. No universally good parameters or processes exist for ceramics processing at this time. Even for the same material, the most common adjustable parameters, such as laser power, scanning speed, hatch distance, and laser spot size, can vary wildly depending on the requirement of a better mechanical strength or a better surface finish. The parameters are crucially dependent on the existence and variety of additives. For example, very different parameter sets for processing alumina exist (**Table 2**) [27, 28, 55, 56]. Additionally, the parameters also relied on powder and layer factors as well as preheating conditions. On the other hand, for each individual experiment, there are clear trends regarding the laser parameters. Some of the basic trends are summarized below.

| | Powder size (μm) | Layer thickness (μm) | Laser wavelength (μm) | Laser beam diameter (μm) | Laser power (W) | Scanning speed (mm/s) | Hatch distance (μm) | Energy density (J/mm$^2$) | Relative density (%) | Other conditions |
|---|---|---|---|---|---|---|---|---|---|---|
| $Al_2O_3$ coated by PVA + resin E06 [56] | 80 | — | — | — | 15, 18, 21 | 1600, 1800, 2000 | 100, 120, 140 | 0.088 | 94.6 | Postheat @ 1600°C |
| $Al_2O_3$ + 0.1 vol% graphite, slurry [28] | 106 | 50–100 | 1.064 | 69 | 100–150 | — | 50–400 | 5.1–19.9 | 97.5 | — |
| $Al_2O_3$ slurry [55] | 0.3 | 50–200 | 10.6 | 400 | 2 | 5.2 | 200 | 1.9 | 85 | Preheat @ 800°C; postheat @ 1600°C |
| $Al_2O_3$ suspension [27] | 0.45 | — | 10.6 | 1.5–2.5 | 72 | 4 | — | 9 | — | Preheat @ 2000°C |

**Table 2.** Parameters for LPBF process on $Al_2O_3$.

Laser energy density is a very important factor in the LPBF process. In general, the adjustment of parameters that increase the laser energy density results in greater fusion ability as demonstrated by a deeper laser penetration depth or a larger melting pool. Increase of the energy density may be realized through increasing the laser power, decreasing the scanning speed, increasing the hatch distance, using a better focus of the laser beam or changing the laser beam size, or increasing the point overlapping. On the one hand, it was difficult to construct ceramic parts successfully due to insufficient solidification of powders with too low laser energy. On the other hand, high laser energy density induces layer shrinkage because of powder layer overheat or ablation, and the ceramic part warps [57]. Energy density crucially affects the relative density and porosity of the laser processed part [27], but the laser energy density and the relative density of the product do not always follow a positive relation. Wang et al. reported that at the region of low laser energy density, the relative density of the produced part increased with the laser energy density, but after a certain value, a further increase of the laser energy density reduced the relative density of the part [56]. Energy density also severely influences the surface conditions and grain sizes of the laser produced parts. Shishkovsky et al. reported larger mosaics on the surface by reducing the energy density through increasing the laser scan velocity and the hatch distance [13]. Yap et al. reported sunken cores for the samples obtained at higher energy densities, suggesting that vaporization of silica material occurred during the process as the silica material absorbed enough energy to be vaporized [58].

Although the concept of energy density is very useful, practically it has to be adopted with caution because there is sufficient evidence to show inconsistent or controversial results if process optimization is only based on this factor. Wang et al. showed a huge difference in the relative density by similar laser energy density while varying the laser point overlapping [56]. Liu et al. also reported the same energy density led to different relative densities and mechanical properties [59]. The issue of the laser energy density has also been noted by the latest research. Because the laser energy density is insufficient to capture the complex physics of the melt pool, this parameter is identified as an unreliable indicator or not a good design parameter for materials' synthesis by LPBF methods [38, 60]. Although the energy density remains constant, the variable combination of the laser power, the laser scanning speed, and the laser hatch distance plays a significant role, and the laser power has a dictating influence [38]. Liu et al. noted that the influence for the three adjustable laser parameters are not the same to the manufactured parts, precisely, the laser power has the greatest effect, the laser hatch distance is in the middle, and the laser scanning speed has the least effect [59]. However, the different effects among those parameters are not reflected in the concept of the laser energy density. Therefore, the laser energy density cannot be the only criterion in the optimization of process parameters during the SLS/SLM process. An optimum process has also to involve additional process parameters, such as hatch style, laser spot size and laser offsets, and materials properties, including thermal conductivity and reflectivity [38].

Besides laser parameters, powder factors also play a critical role in reaching a high density part. The size and morphology of the powder particles have strong impacts on the powder bed density and the powder flowability and hence significantly influence the product. In order to uniformly spread powders to a thickness of tens to a few hundred microns at high temperatures, a good flowability is critical, which requires powders of specific size distributions and

spherical shape. In general, small particles lead to a better surface, and the spherical shape of particles leads to better flowability and less porosity. Hagedorn et al. reported the surface roughness may be improved by decreasing the particle size from 50 to 30 μm [48]. Wilkes et al. demonstrated that spherically shaped particles significantly improved the relative density and porosity [9]. The method of preparing the powder bed and the layering step are important factors, and optimal processes may lead to sizable improvement of the product. The powder bed should be homogeneous, have high packing density and have a stable layer thickness. Bertrand et al. suggested increasing the powder bed density by compression from the roller [12]. Juste et al. also suggested increasing the powder bed density to decrease the cracks and heterogeneities through the use of more suitable powders and/or by considering specific devices to pre-compact the powder bed [28]. Wang et al. compared the experimental and simulated relative density under different pressures and revealed a positive relation between them, as shown in **Figure 5** [56]. Compressing the powder bed or each powder layer to a denser format before or during each laser scan cycle should be considered for future development in the LPBF process.

The layering step and the deposition technique are critical parts of direct-layered fabrication technologies. For example, Deckers et al. deposited layers through the electrophoretic deposition (EPD) method to avoid large particle and thermal gradients [55]. They suggested slurry-based processes can produce highly dense ceramic parts more easily. Juste et al. also showed good relative density parts using the slurry process [28]. However, this wet process required additional steps. Finally, in the layer-by-layer method, the thickness of each layer is recommended to satisfy the following requirement for a good fusion. Several researchers noted that particles to be ten times smaller than the layer thickness [12, 61], and Bertrand

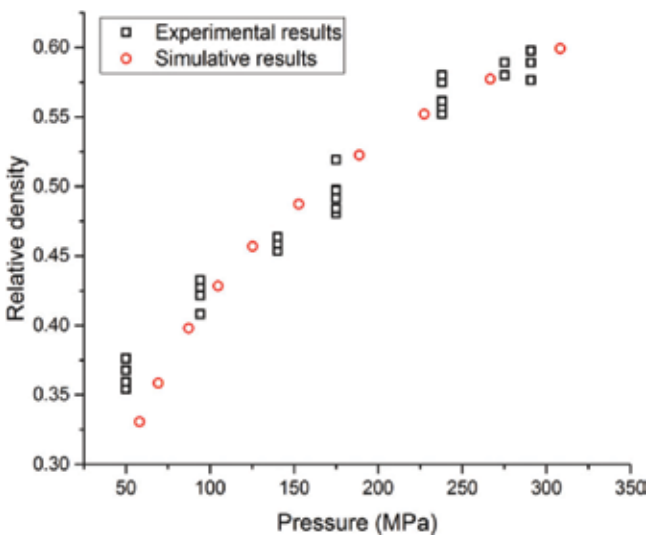


**Figure 5.** Comparison between the experimental and simulated results of the relative density under different pressures. The data presented here are extracted from those presented in the original source [56].

http://dx.doi.org/10.5772/intechopen.75832

et al. suggested that each layer allow the laser to penetrate at least through the last and the previous one [12]. A proper combination of laser and powder parameters may lead to the desired properties; for example, the laser power, the layer thickness, and the scanning speed greatly affect shrinkage, distortion and warping, which in turn affect the quality and dimensional accuracy of the parts [62].

Cracks and less than full density are common difficulties in laser processed ceramics. Preheating of the powder bed helps form a denser part and to reduce cracks that are created due to stress and lack of thermal relaxation. Hagedorn et al. reported reaching nearly 100% relative density using a secondary laser as the preheating source [48, 54]. However, this method suffers from bad surface quality for the produced part. Wilkes et al. reported generally crack-free samples through a preheating process showing that powder bed preheating reduces thermal stresses and the formation of cracks [9], but superficial microcracks still existed for large parts during the process [48, 54, 63]. The fine cracks are presumably formed due to thermal stress from the uneven distribution of heat within the laser spot, which induces different volume contractions during the melting and cooling process [64]. Although preheating and secondary laser assistance may reduce the thermal stress and help to reduce cracks, the preheating may decrease the powder flowability and impair the process repeatability [12]. A new preheating strategy to avoid the rapid cooling and the thermal stress requires further technological developments.

Another factor affecting the process is the oxygen environment, and the impact of this factor is strongly material dependent. A low oxygen environment significantly reduces the occurrence of balling [40, 41, 65]. Shishkovsky et al. compared the alumina–zirconium ceramics synthesis in both air and argon environments and found an oxygen-deficit environment clearly affected the light energy absorption, the porosity, and the mechanical strength [13]. Savchenko et al. recommended sintering zirconium in an inert gas environment or in a vacuum for stabilization of the tetragonal phase $ZrO_2$ [66].

Today normal SLS/SLM techniques are capable of achieving near full relative density for ceramics, but the resulting ceramics are often compromised by high surface roughness, poor dimensional accuracy, micro-crack formation problems, and poor mechanical properties. In recent years, new developments in LPBF have shown some improvement in these aspects. Exner et al. demonstrated a laser micro sintering technique using a q-switched pulse laser system with 532 nm wavelength to process silica-alumina ($SiO_2/Al_2O_3$) powder [67]. The intensity of the laser spot of the q-switched beam is a factor of several orders of magnitude higher than that of continuous wave lasers due to its short intense pulses in a nanosecond regime, and a very high recoil pressure was generated for the sintering process. In order to obtain good accuracy and surface finish, fine powders with particle diameter less than 1 μm were used. The final parts had a high geometric resolution of 40 μm, the best surface quality so far, with an average surface roughness $R_a$ ~ 5 μm, and a maximum relative density of 98%. The produced part still had many small pores and micro cracks inside the sintered body. After thermal treatment, the cracks were annealed, and the number of pores decreased although some bigger pores were left. The heat treatment resulted in nearly no shrinkage (<0.7%) of the specimens. The paper also reported a maximum crushing strength of 1400 MPa, and a low tensile strength of 120 MPa that limited its use in high strength components.

## 4. Exemplars

With the principles being discussed, it is useful to look at actual examples for some of the most common ceramics: alumina, silica, and mixture of oxide ceramics. These examples are selected to cover ceramic fusion through both direct and indirect methods, SLM and SLS, short (1.06 μm) and long (10.6 μm) laser wavelengths. They also show comparisons for various conditions such as different sized powders, different laser energy densities, with and without preheating or postheating, in air and oxygen-deficit environment, etc. However, the following exemplars do not constitute a completed survey; rather, representative examples are selected to show some of the best progress in the field so far. Some of the processing parameters are summarized in **Tables 2–4** which are slightly different as not all parameters were reported or available in most papers.

### 4.1. Exemplar I: Alumina ($Al_2O_3$)

Aluminum oxide, also known as alumina, is often used as an abrasive or a refractory material due to its high hardness, temperature and electrical resistance. Pure $Al_2O_3$ melts at 2072°C. Some research on this material takes the indirect route due to the high melting point, but direct SLS/SLM is also possible although it often requires very fine (sub-micron) powders.

The following discussion illustrates the indirect method, the effect of post-heating, and the choice of laser energy density. Wang et al. reported using the indirect method to process alumina [56]. The sample was $\alpha$-$Al_2O_3$ coated by 1.5 wt.% polyvinyl alcohol (PVA) and then mixed with epoxy resin E06, forming spherical powders with a size of 80 μm. The processing parameters were: laser power between 15 and 21 W, a scanning speed between 1600 and 2000 mm/s, and a scan space between 100 and 140 mm. The paper reported the optimized energy density of 0.088 J/mm$^2$, which resulted in a relative density of 34% with a bending strength of 1.05 MPa. Post-processing sintering was necessary for densification. Post-process sintering helped to increase the migration rate, grain growth and pore exclusion. After 4 h at 1600°C, the relative density reached 94.6%, a 178% improvement. The relative density increased with increasing laser power and decreased with increasing hatch distance.[1] The relation of the relative density to the scanning speed was more complex in that it initially decreased and then increased with increasing scan speed. Considering the three separate processing parameters, there was an optimum laser energy density which achieved the largest relative density, as shown in **Figure 6**.

The following example shows the SLM process, the effect related to laser point overlapping and layer thickness. Juste et al. mixed alumina powders with 0.1 vol.% graphite to increase the absorption of the Nd:$YVO_4$ laser (1.064 μm) [28]. Graphite was used as the absorption additive because experiments for the pure alumina were not successful, even with a laser power up to 200 W. The slurry of alumina and graphite-based colloidal suspension mixture was spray-dried and then processed in an Ar environment. By optimizing the parameters, a relative

[1] 'Scanning space' as used by the original source [56] is interpreted as hatch distance here.

| | Powder size (μm) | Layer thickness (μm) | Laser wavelength (μm) | Laser beam diameter (μm) | Laser power (W) | Scanning speed (mm/s) | Hatch distance (μm) | Energy density ($J/mm^2$) | Surface roughness (μm) | Compress strength (MPa) | Dimensional accuracy (mm) | Porosity (%) | Other conditions |
|---|---|---|---|---|---|---|---|---|---|---|---|---|---|
| $SiO_2$ [58] | — | 100 | 1.06 | 80 | 100 | 100 | 40–60 | 16.7–25 | — | — | — | — | — |
| $SiO_2$ (slurry of 60 wt.% power + 40 wt.% sol) [57] | 10–16 | 100 | 10.6 | — | 6.5 | 120 | 100 | 0.54 | — | — | — | — | — |
| Silica sand [11] | — | 200 | 10.6 | 300 | 160 | 120 | 200 | 6.7 | ~36 | — | 0.4 | — | Post process: infiltration |
| Silica sand ($SiO_2$ + a little $Al_2O_3$) [68] | 50 | 150 | 10.6 | — | 120 | 120 | 200 | 5 | 24.8–28.2 | 11.8–13 | — | — | Preheat @ 400°C |
| 2% PF + silica sand [46] | 98 | 300 | 1.06 | 50 | 5–8 | 300–500 | — | 10–20 J/m (line energy) | — | 0.8 | — | 25.7–36.9 | — |
| 8.3% PF + silica sand [52] | — | — | 10.6 | 3000 | 12 | 10.8 | 2500 | 0.44 | — | — | — | — | — |

**Table 3.** Parameters for LPBF process on $SiO_2$


http://dx.doi.org/10.5772/intechopen.75832

| | Powder size (μm) | Layer thickness (μm) | Laser wavelength (μm) | Laser beam diameter (μm) | Laser power (W) | Scanning speed (mm/s) | Hatch distance (μm) | Energy density ($J/mm^2$) | Relative density (%) | Bending Strength $\sigma_{fM}$ (MPa) | Surface roughness (μm) | Dimensional accuracy (μm) | Other conditions |
|---|---|---|---|---|---|---|---|---|---|---|---|---|---|
| $SiO_2$-$P_2O_5$-CaO [8] | 5–10 | 50–150 | 10.6 | 300 | 5–25 | 50–300 | — | 1.5 | 72 | 4.7 | 25 | — | Post-heat @ 1200°C |
| $K_2O$-$Al_2O_3$-$SiO_2$ [59] | 5–25 | 80 | 10.6 | 200 | 21 | 1800 | 100 | 0.1167 | 36.45 | 2.08 | — | — | Preheat@ 30–35°C |
| $ZrO_2$-$Y_2O_3$ [12] | 1–40 | 30 | 1.064 | — | — | 1250–2000 | 20–40 | — | 56 | — | — | — | — |
| YSZ-$Al_2O_3$ [48, 54] | — | 50 | 1.06 | 200 | 60 | 200 | — | — | ~100 | 500 | 100 | 150 | 2nd laser, preheat@ 1600–1730°C |
| YSZ-$Al_2O_3$ [9] | 20–70 | 50 | 1.06 | 200 | 60 | 200 | — | — | ~100 | 538.1 | — | — | 2nd laser, preheat@ 1570–1800°C |
| YSZ + Al/$Al_2O_3$ [13] | — | — | 1.06 | 80 | 50 | 1500–2000 | 20–40 | 0.625–1.67 | — | — | — | — | In air/Ar environment; laser defocalization ~ 6 μm |

**Table 4.** Parameters for LPBF process on ceramic mixtures.

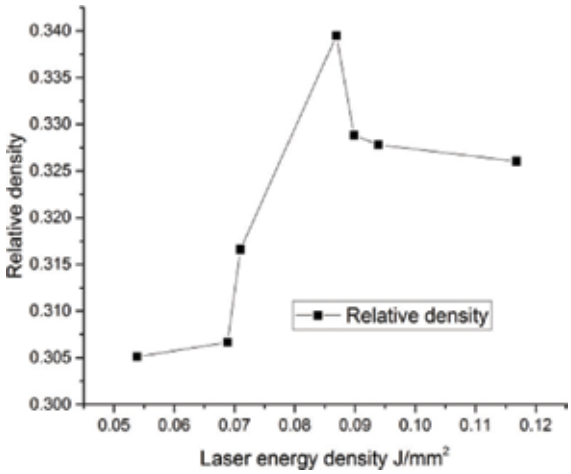


**Figure 6.** The laser processed $Al_2O_3$-resin E06 composite reached the peak relative density value of 0.34 when the laser energy density was approximately 0.088 J/mm$^2$. The data presented here are extracted from those presented in the original source [56].

**Figure 7.** Pure alumina parts processed by SLM. Reprinted from [28], with permission of Cambridge University Press.

density greater than 90% was achieved. An example of the SLM processed parts is shown in **Figure 7**. The correlation between the product's relative density to the laser energy density and point overlapping is shown in **Table 5** and **Figure 8**. Energy density directly affects the relative density; however, it cannot be used as the single laser parameter for SLM/SLS processes. For example, laser point overlapping had a significant influence on the geometrical features and microstructures of the product [69]. Juste et al. [28] further explored the effects of layer thickness and found a relative density increase from 76.9 to 85.1% by decreasing the layer thickness from 100 to 50 μm. The SEM micrograph showed a microstructure with smaller pore size, suggesting a better welding between two consecutive layers from a more homogeneous and efficient melting. Hence, a decrease in layer thickness improved the microstructures and the relative density of parts.

| Experiment | Relative density (%) | Energy density, $j$ (J/mm$^2$) | Point overlapping, $Ov$ (%) |
|---|---|---|---|
| E2 | 57.2 | 5.1 | −44 |
| E5 | 67.3 | 6.3 | −44 |
| E8 | 76.9 | 7.6 | −44 |
| E3 | 0.0 | 5.3 | −477 |
| E6 | 0.0 | 6.6 | −477 |
| E9 | 0.0 | 7.9 | −477 |
| E1 | 92.9 | 13.3 | 28 |
| E4 | 97.5 | 16.6 | 28 |
| E7 | 97.3 | 19.9 | 28 |

**Table 5.** Relative densities vs. laser energy density and point overlapping. The data presented here are from those presented in the original source [28].

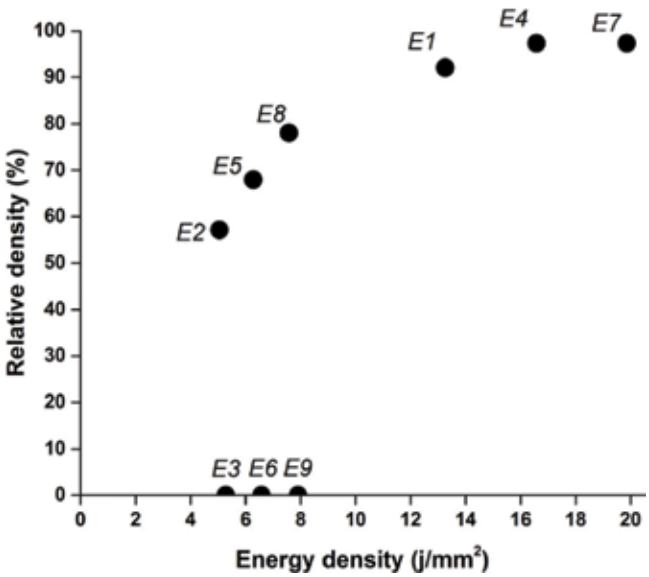


**Figure 8.** Relative density of laser produced part vs. laser energy density The data presented here are extracted from those presented in the original source [28].

The following two examples demonstrate the direct method without any binders, and they also show how layer deposition is critical for LPBF technique and the effect of varying laser energy density. Deckers et al. used a $CO_2$ laser for direct SLS/SLM on alumina slurry mixed with very fine (0.3 μm) powders of alumina, denatured ethanol, and $HNO_3$ [55]. The layers were then deposited through electrophoretic deposition (EPD). The combination of small powders, EPD deposition, and high preheating temperatures (800°C) reduced the need for large energy density to process the alumina slurry without binders. This treatment helped to

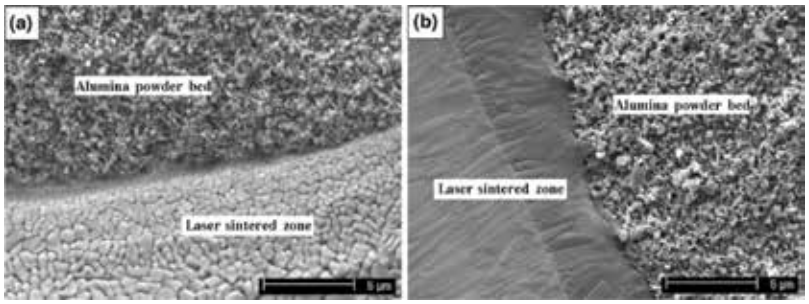


**Figure 9.** SEM micrographs of powder beds densified using laser scanning speeds of (a) 4 mm/s and (b) 2 mm/s. Reprinted from [27], with permission of Elsevier.

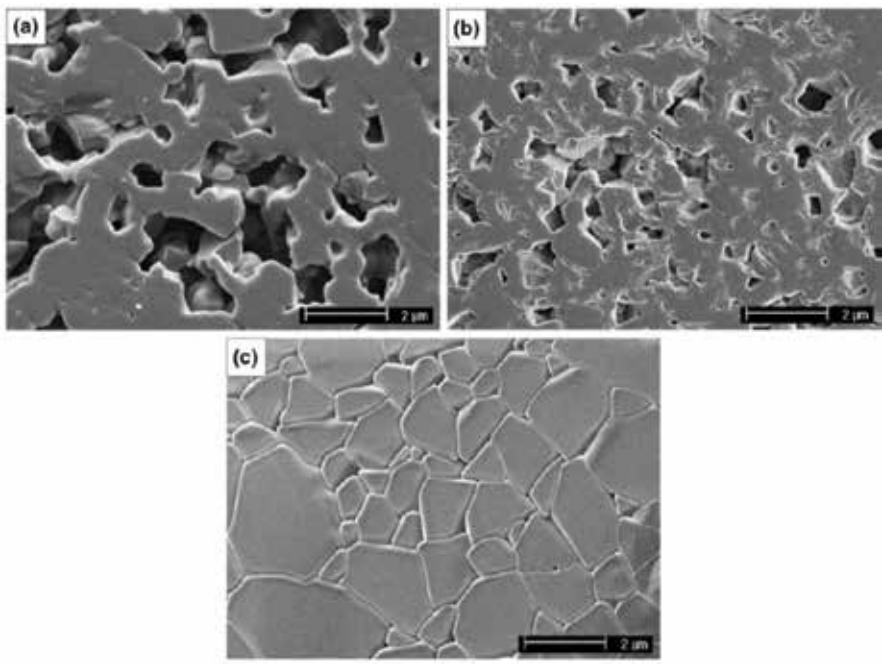


**Figure 10.** Cross-section SEM micrographs of alumina powder beds densified using laser energy densities of (a) 4.0 J $mm^{-2}$ (b) 7.0 J $mm^{-2}$ and (c) 8.5 J $mm^{-2}$. Reprinted from [27], with permission of Elsevier.

avoid large grain size and high thermal gradients. A relatively high density of 85% was obtained after the post-process heating.

Wu et al. also applied a $CO_2$ laser to process 99.8 wt.% pure alumina [27]. The special treatment here is that the fine particles (0.45 μm) of the alumina powder beds were generated through aerosol assisted spray deposition. The study clearly demonstrated the effect of scanning speed (**Figure 9**) and laser energy density (**Figure 10**) on the microstructure of the laser-sintered alumina powder beds. A higher laser power, a lower laser scanning speed or a smaller

laser beam size resulted in a higher laser energy density, and the resulting higher temperature promoted the densification of the powder bed. By increasing the energy density, the microstructure of the powder beds varied from open pores to full densification.

### 4.2. Exemplar II: Silica ($SiO_2$)

Silicon dioxide, also known as silica, is one of the most common ceramic materials. As the major constituent of sand, it is very abundant. Silica is widely used as structural materials, in microelectronics, and in food and pharmaceutical industries due to varies properties such as high melting temperature and very low thermal and electrical conductivity. Most silica is produced by mining such as sand mining and purification of quartz. Silica parts can be laser processed by direct or indirect method.

Yap et al. demonstrated the SLM process using a short wavelength laser. They reported complete melting and forming a 100 μm thick layer of 99.7% pure silica powder in Ar through a good combination of parameters even at very low optical absorption (0.04 for $SiO_2$ @ 1.06 μm) [58]. The laser energy density was between 16.7 and 25 J/mm$^{2***}$. They also showed that sunken cores formed from high laser energy density, suggesting vaporization of silica material during the process.

Lee et al. showed the indirect SLS process on a slurry-deposited layer. They reported successful sintering slurry of silica powder (60 wt.%) and silica sol (40 wt.%) with a small energy density using a $CO_2$ laser [57]. They also demonstrated a better surface finish and a good edge profile with a proper laser energy density feedback control process.

The following two examples show the direct SLS process, and the relation between laser processing parameters and the surface roughness and dimensional accuracy of the sintered parts. Wang et al. made use of a $CO_2$ laser to directly sinter silica sand, which is a mixture of $SiO_2$ (97.51 wt.%), with small amount of a variety of impurity of elements such as Zr, Ti, Ca, Al, Ba, Fe, Cs, Mg [11]. Pure silica softens at 1500°C and melts at 1600°C [11], but the impurities form a low-melting point eutectic that partially melts at 500–700°C. The existence of impurities

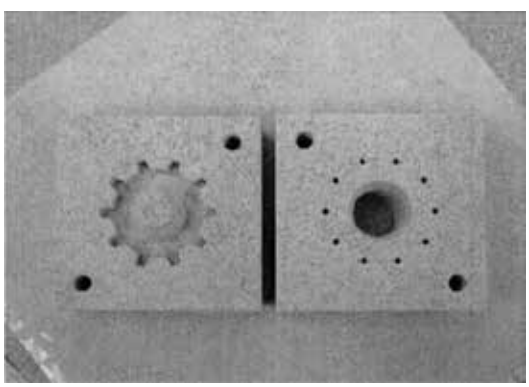

**Figure 11.** Sand mold built from silica sand powders, using LPBF. Reprinted from [11], with permission of Springer.

therefore facilitates the direct laser sintering of the silica sand. Wang et al. studied the influence of the laser process parameters and concluded that larger power and a smaller scanning speed led to greater strength and thickness, but the process also produced a rough surface finish. To improve the surface conditions, instead of a common polishing process, a simple infiltration post-process improved the roughness of the horizontal surface from $R_a$ = 35.6–25.4 μm. One example of the directly sintered parts in silica sand is shown in **Figure 11**.

Tang et al. also directly sintered silica sand with a $CO_2$ laser [68] and preheated the powder bed up to 400°C. The silica sand consisted mainly of $SiO_2$ with a very low percentage of $Al_2O_3$, and the small amount of $Al_2O_3$ acted with $SiO_2$ to form a low-melting-point eutectic. This eutectic facilitated the melting of the surface of the sand particles under laser heating, although the core of the particle remained at the high melting point. The sand particles bound together through the liquid surfaces when the laser beam struck and then quickly solidified after the laser beam moved away. Tang et al. further studied how the process parameters affected the properties of the laser sintered parts and concluded the compression strength of the products increased when the laser power increased and decreased when the scanning speed increased. The largest compression strength they produced was 15.5 MPa with a laser power of 120 W and a scanning speed of 60 mm/s. They also found the surface roughness of sintered products increased when the laser power increased and decreased when the scanning speed increased. The smallest surface roughness they achieved was $R_a$ = 19 μm at the laser power of 120 W and the scanning speed of 180 mm/s. Finally, the absolute errors (the differences from the actual sizes of sintered parts to the design sizes) ranged from 0.1 to 0.5 mm, depending on the laser process parameters. The best result (0.137 mm in the $x$ direction and 0.117 mm in the $y$ direction) was achieved when both the laser power (160 W) and the scanning speed (180 mm/s) were the largest among the parameters they tested. However, the researchers also found the dimensional accuracy of the sintered parts was relatively stable and insensitive to a certain range of processing parameters.

Liu et al. exhibited the indirect SLS process with a short wavelength laser, and it also showed the relation between laser line energy and porosity, mechanical strength, and shrinkage depth of the manufactured parts. They reported the indirect laser sintering on polymer coated silica sand composite powders using a 1.064 μm laser [46]. The silica sand they used mainly consisted of $SiO_2$ 99%, $Al_2O_3$ 0.22% and micro-content of $TiO_2$ with a melting point of 1750°C [46]. The silica sand was coated with 1.9-2.1 wt.% of phenol-formaldehyderesin (PF). Liu et al. studied the relation between line energy (power/scanning speed) and properties of the sintered parts. The best line energy was located between 10 and 20 J/m, which resulted in a porosity of 29–32% for the laser sintered parts. Both the porosity and shrinkage depth of the powder bed generally increased with the increase of the line energy in that range, while the shrinkage depth gradually fell after 20 J/m. With a set of optimized parameters (laser power of 7 W, scanning speed of 400 mm/s, and laser beam spot of 50 μm), a compressive strength of 0.8 MPa was obtained. This strength was equivalent to that of sand patterns made by the common method and exhibiting strengths in the range 0.5–2.5 MPa [46].

Song et al. demonstrated the indirect SLS process with a long wavelength laser, and they showed the relation between laser process parameter and the dimensional accuracy of the

fabricated parts. They indirectly sintered PF/silica sand compounds using a $CO_2$ laser [52]. They found laser process parameters had important effects on the property and accuracy of the sintered parts. For example, the scanning speed affected the size of the sintered parts: with an increase of the scanning speed from 5 mm/s to 13.3 mm/s, the dimensions of the sintered sample shrank for about 1.5 mm in both length and height, and 1 mm in width.

### 4.3. Exemplar III: Mixture of oxide ceramics

The following example shows the effect of laser energy density and layer thickness to the mechanical properties of the produced part. Silica can be used as bio-ceramics for tissue scaffolds or dental implants when it is mixed with other ceramics or minerals, such as hydroxyapatite (HA), feldspar, kaolin and alumina [58]. F.-H. Liu performed selective laser sintering on hydroxyapatite-silicate slurry with a $CO_2$ laser [8]. The mixture was comprised of $SiO_2$-$P_2O_5$-CaO, materials which had the potential to produce bone scaffolds for tissue engineering applications. An optimized laser energy density was critical to the process. An energy density that was too small would result in an overlap between layers less than 15%, which led to insufficient bonding strength. An excessive energy density would result in warping layers if the overlap exceeds 30%. With an optimized slurry (28 wt.% $SiO_2$, 30 wt.% HA, and 42 wt.% $H_2O$), a laser energy density of less than 1 J/mm$^2$ enabled formation of the bio-ceramic parts. The paper further revealed the significant effect of laser energy density on bending strength, as shown in **Figure 12**. The maximum strength achieved was 4.7 MPa at 1.6 J/mm$^2$.

The following example exhibited the indirect SLS process and the effect of the laser process parameters. The mixture $K_2O$-$Al_2O_3$-$SiO_2$ shows excellent mechanical properties and biocompatibility which come up to the ISO standards as a dental restoration material [70, 71]. Liu et al.

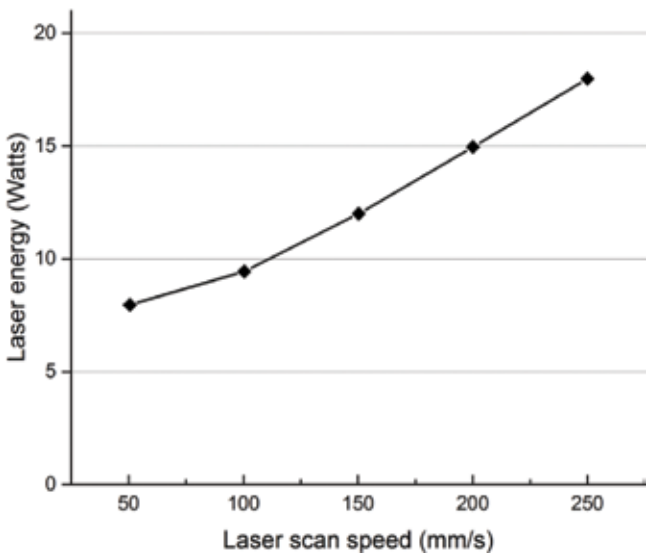


**Figure 12.** Relationship between laser scanning speed and laser energy. The data presented here are extracted from those presented in the original source [8].

studied the composite powder of an epoxy resin binder E-12 and $K_2O$-$Al_2O_3$-$SiO_2$ series of dental glass-ceramics through indirect selective laser sintering [59]. The paper described the effect of the laser processing parameters on the relative density of the sintered parts and concluded that laser power, scan spacing, and scanning speed had different effects to the produced part. Specifically, the factor of laser power had the greatest ability to influence the relative density and the bending strength, the factor of scanning speed had the least effects, and the factor of scan spacing was in between. In order to obtain high density parts, they suggested increasing the laser power and decreasing the scan spacing and the scanning speed. However, the authors suggest other factors such as SLS forming efficiency and forming precision should also be considered for optimizing the processing parameters [59]. An example of the processing parameters and the parts' properties is illustrated in **Table 6**. The bending strength was basically proportional to the relative density of the sintered parts. Although in general the relative density followed the laser energy density, this relationship was only approximate. For example, sample numbers 1, 4, and 7 had the same energy density but different relative density and mechanical properties. The paper also noted that the preheating temperature was an important processing parameter that affected the viscous binder's wetting and spreading characteristics, so it had a considerable influence on the relative density of the sintered parts. The optimized processing parameters, the preheating temperature, the laser power, the scanning speed, the scan spacing and the layer thickness were 30–35°C, 21 W, 1800 mm/s, 100 and 80 μm, respectively. Under such conditions, the relative density and bending strength reached 37.40% and 2.08 MPa, respectively. An example of the indirectly sintered glass-ceramic part is shown in **Figure 13**.

For component mixed ceramic materials, it is common to use additive elements to bind them before the LPBF process. However, a pure mixture without a binder is possible to be processed. For example, Bertrand et al. showed a direct process on pure yttria-zirconia ($Y_2O_3$-$ZrO_2$) powders through selective laser sintering/melting using a 1.064 μm fiber laser [12]. The authors studied the influence from the powder and the powder bed and found the properties

| No. | Laser power (W) | Scan speed (mm/s) | Scan spacing (mm) | Energy density (J/mm$^2$) | Relative density (%) | Bending strength $\sigma_{fM}$ (MPa) |
|---|---|---|---|---|---|---|
| 1 | 15 | 1600 | 0.10 | 0.0938 | 34.59 | 1.63 |
| 2 | 15 | 1800 | 0.12 | 0.0694 | 33.79 | 1.59 |
| 3 | 15 | 2000 | 0.14 | 0.0536 | 33.70 | 1.54 |
| 4 | 18 | 1600 | 0.12 | 0.0938 | 34.83 | 1.66 |
| 5 | 18 | 1800 | 0.14 | 0.0714 | 33.98 | 1.62 |
| 6 | 18 | 2000 | 0.10 | 0.0900 | 35.05 | 1.98 |
| 7 | 21 | 1600 | 0.14 | 0.0938 | 36.59 | 2.01 |
| 8 | 21 | 1800 | 0.10 | 0.1167 | 37.40 | 2.08 |
| 9 | 21 | 2000 | 0.12 | 0.0875 | 36.38 | 2.02 |

**Table 6.** SLS results for dental glass-ceramic powder. The data presented here are from those presented in the original source [59].

**Figure 13.** Teeth made by SLS under the optimized technical parameters Reprinted from [59], with permission of Emerald Publishing Limited.

of particles and powder layers significantly affected the product. For example, they found the best powder for the fiber laser to process was a powder in which all particles have a diameter less than 1 μm. Atomized powders helped to avoid electrostatic charges that led to powder agglomeration. Furthermore, the particle morphology directly affected the powder spreading and the powder bed density in that the more spherical particles improved the results although the authors of the work did not specify the aspects which were improved. The layer thickness is a crucial parameter for a good sintering/melting process. To decide this parameter, the paper suggested that the laser had to penetrate at least through the last powder layer and the previous one. Earlier, Wilkes and Wissenbach suggested that the layer thickness needs to be 10 times greater than the particle size for achieving efficient roller powder layering [61]. To satisfy these requirements, Bertrand et al. reported a 30 μm thick layer in their study. The paper also reported the preheating effect and concluded that, on one hand, the preheating reduced the micro cracks; on the other hand, preheating decreased powder flowability and impaired process repeatability. An example from such a direct laser process is shown in **Figure 14**.

The following discussion shows the effect of preheating and the secondary laser assistance. Oxide ceramics such as zirconia and alumina are widely used in industry and in medical applications such as bearing sleeves and valves, high density grinding media, cutting blades, crowns and bridges in dental restorations. Hagedorn et al. reported direct selective laser melting on an eutectic $Al_2O_3$-$ZrO_2$-$Y_2O_3$ mixture without any binder materials [48, 54]. The mixture was composed of 58.5 wt.% of $Al_2O_3$ (melting point 2072°C) and 41.5 wt.% $ZrO_2$ (melting point 2710°C) where $ZrO_2$ contains 6 wt.% yttria ($Y_2O_3$) to form a eutectic powder. It demonstrated a complete melting to the ceramic powders using a low optical absorptive Nd: YAG laser with a wavelength of 1.06 μm. The unique feature here is the work applied a $CO_2$ laser assistant that preheated the powder bed surface above 1600°C, very close to the eutectic mixture melting point of 1860°C. The secondary laser helped to reach the melting temperature of the ceramics and led to a large melting pool. Such a process improved the density of the obtained part. For example, with the optimized process parameters, the laser processed part

http://dx.doi.org/10.5772/intechopen.75832

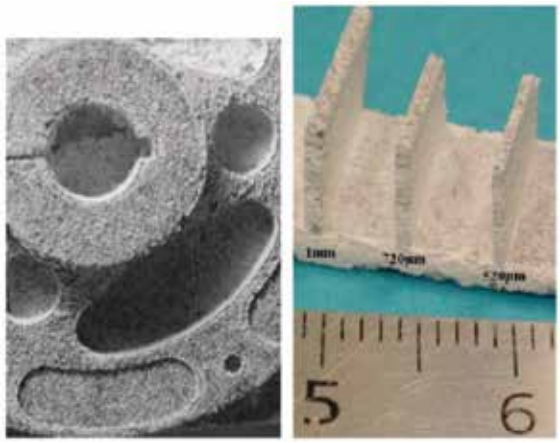


**Figure 14.** Pure zirconia 3D objects manufactured by SLS/M technology Reprinted from [12], with permission of Elsevier.

yielded a relative density of approximately 100% without any post-processing. Such a part showed a fine-grained nano-sized microstructure and flexural strengths of above 500 MPa, sufficient for dental restorations. This value is in the same range but at the lower end compared with conventionally manufactured parts which have flexural strengths of 800–1200 MPa for zirconia [72], 400 MPa for alumina [73] and 480–2400 MPa for mixtures of zirconia and alumina [9, 74]. On the other hand, the second laser assistance negatively affected the surface quality and dimensional accuracy because the low viscosity melt pool flowed outside the boundaries of the scanned part and wet the surrounding powders. The surface roughness was $R_z$ ~ 100 μm, one of the best in SLM-processed high-strength oxide ceramics. The dimensional accuracy reached ~150 μm, which was far below that of the conventionally milled parts of ~50 μm. An example of a direct SLM produced full ceramic framework for a dental restoration is shown in **Figure 15**. A rough surface may induce stress peaks on mechanical loading, which leads to premature failure and thus affects the mechanical strength. The preheating


**Figure 15.** Direct SLM produced full ceramic framework for a dental restoration Reprinted from [54], with permission of Elsevier.

method may also induce thermal shocks during the deposition of the cold ceramic powder, which can result in fine cracks on the surface of the produced part and hence reduce the mechanical strength, as shown in **Figure 16**.

The following example showed the effect of particle shapes. Wilkes et al. [9] used the same setups from Refs. [48, 54]. The authors studied how the particle shape (spherical vs. irregular) affected the manufactured parts, and found it had a strong influence on the relative density of the SLM produced parts. There was a significant improvement of the porosity and relative density which was most likely due to the better flowability of spherically shaped particles compared to irregularly shaped particles. A parallel comparison of two cross-sections using different shaped powders is shown in **Figure 17**. The paper described the effect of preheating and concluded temperature differences and gradients during SLM were reduced through the preheating process. Therefore, mechanical stresses were significantly reduced, and large crack formation could be avoided. As reported in Refs. [48, 54], fine cracks can still be found for building up large parts because of the local rapid cooling from the deposition of the cold powder layers on top of the preheated ceramic. The preheated zone in the SLM machine is shown in **Figure 18**. A comparison of the product surface without preheating and with preheating at 1715°C is shown in **Figure 19**.

Shishkovsky et al. showed the effect of an oxygen-deficit environment. They performed alumina-zirconium ceramics synthesis through selective laser sintering/melting [13]. The ceramic mixture was composed of yttria-stabilized zirconia, called YSZ ($ZrO_2$ 90 wt.%, $Y_2O_3$ 10 wt.%), and aluminum or alumina $Al_2O_3$ in the ratio 4:1. They investigated the influence of SLS/SLM processing in air or in a protective gas environment. Laser sintering in argon required scan velocities nearly one order of magnitude smaller than velocities when sintering in air, and the surface temperature of the powder bed was much lower in argon, as well. The thickness of one layer that was sintered in one cycle increased by 1.5–2 times, so the energy needed for sintering in argon gas was much smaller than that in air. When operating in air, they also observed strong sparkling and scattering of the powder material from the interaction

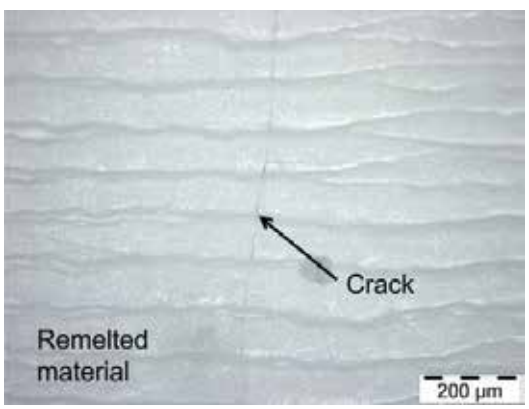


**Figure 16.** Crack formation on the surface of the SLM part due to cold powder deposition onto the preheated area Reprinted from [54], with permission of Elsevier.

http://dx.doi.org/10.5772/intechopen.75832

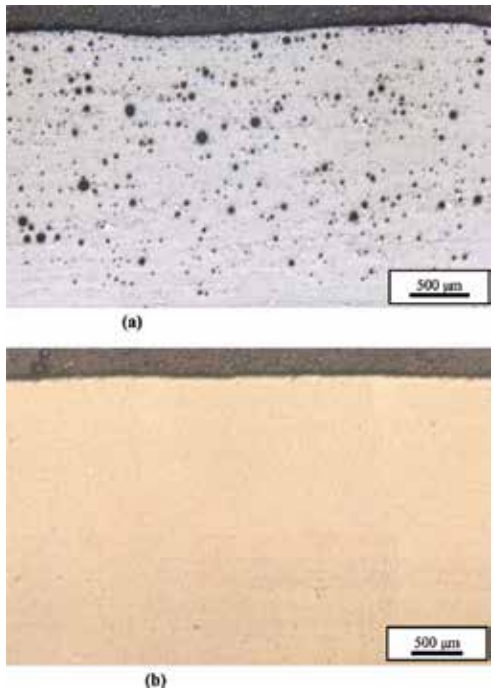


**Figure 17.** Cross-sections of two specimens made using different types of powder (a) irregular shaped powder particles (b) spherical powder particles. Reprinted from [9], with permission of Emerald Publishing Limited.

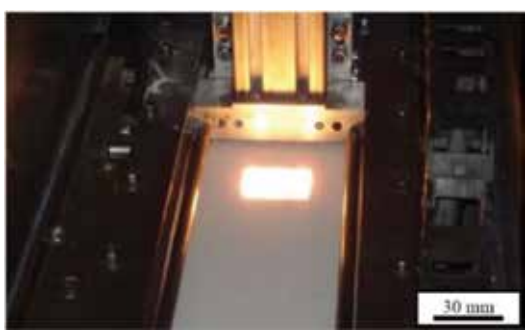


**Figure 18.** Photo of the preheated zone in the SLM machine. Reprinted from [9], with permission of Emerald Publishing Limited.

zone beyond a certain energy density. SLS in air yields ceramics with a dense structure and a uniform distribution of the stabilizing phases although cracks could happen at high laser powers during high-speed cooling. While sintering in argon, a porous part was developed with pore size >100 μm, and the pore shape was elongated in the laser scan direction. Such a high porosity greatly reduced the relative density and the mechanical strength of the sintered ceramics. The surface comparison of the ceramics sintered in air and in argon is shown in **Figure 20**. The research also compared the SLS and SLM processes and demonstrated that

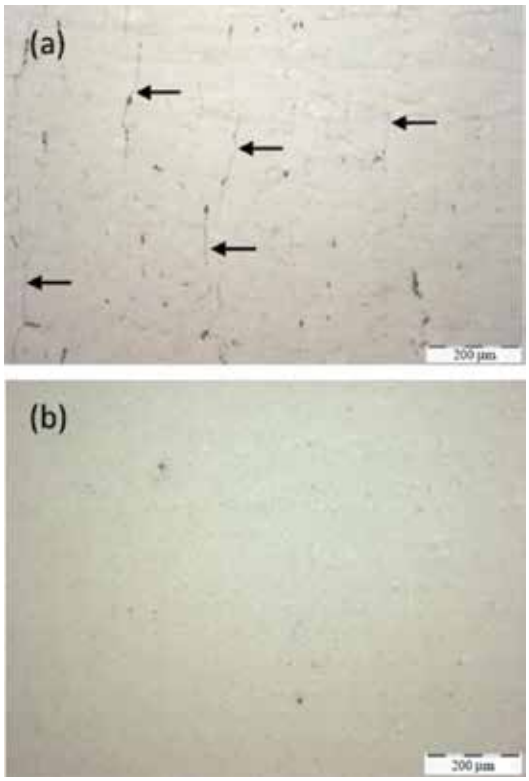


**Figure 19.** Cross-sections of specimens manufactured by SLM (a) cracks formation without preheating and (b) crack-free with preheating at 1715°C. Reprinted from [9], with permission of Emerald Publishing Limited.

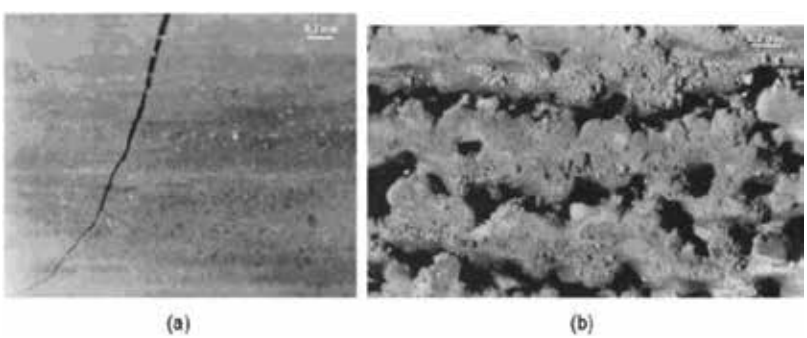


**Figure 20.** Surface comparison of the sintered YSZ-Al/$Al_2O_3$ at P = 24.1 W, V = 3.1 cm/s. Magnification: (a) 50× (in air) and (b) 20× (in argon). Reprinted from [13], with permission of Elsevier.

SLM allows for manufacturing objects with a relatively low porosity and a high geometrical accuracy. Examples of the ceramics manufactured from SLS and SLM techniques are shown in **Figure 21**. The surface porosity appeared to increase by increasing the laser scan velocity and the hatch distance.

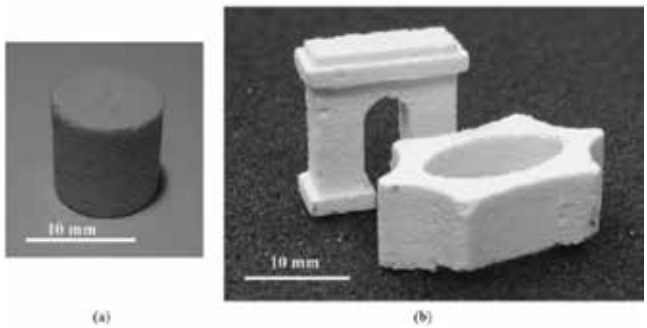


**Figure 21.** Manufactured ceramic objects: (a) porous filter element from corundum–zirconium ceramics produced by SLS process; (b) samples produced by SLM process from $ZrO_2$ powder. Reprinted from [13], with permission of Elsevier.

## 5. Perspectives

Comparing to metals, laser powder bed fusion of ceramics is relatively new, less studied, and less mature [21, 75–77]. Ceramics are a large materials family which includes oxides ($Al_2O_3$, MgO, $ZrO_2$, FeO, NiO, $SiO_2$, CuO, $Ca_3(PO_4)_2$, etc.), carbides (BC, SiC, WC, etc.), nitrides ($Si_3N_4$, $Al_6N_6O_2Si$, AlN, etc.), sulfides ($Yb_3S_4$, CeS, $CaLa_2S_4$, $MgYb_2S_4$, $MnEr_2S_4$, $ZnGa_2S_4$, etc.), fluorides ($CaF_2$, $BaF_2$, $SrF_2$, etc.), and ceramic component mixtures ($Al_2O_3$-$ZrO_2$, $Al_2O_3$-$SiO_2$, $ZrO_2$-$Y_2O_3$, $Li_2O$-$Al_2O_3$-$SiO_2$, $K_2O$-$Al_2O_3$-$SiO_2$, etc.). However, so far the laser powder bed fusion on ceramics has been studied on only a small fraction of this materials family. Not all of them may be suitable for the current layer-by-layer construction technique due to factors such as high melting temperature, different optical/thermal properties, or availability of suitable powders. Further development may lead to construction of multi-material, multifunctional objects.

To obtain desired structural and physical properties of a fabricated part, an optimized process is required for the laser powder bed fusion technique. However, since the process parameters are completely material-dependent and can be varied largely for different ceramics, it is necessary to optimize the process parameters for each material through series of experiments, theoretical modeling, or a combination of both. The optimization includes powder, laser, and environmental factors, as well as possible pre- and post-processes.

In recent years, new development has been focused on using the laser powder bed fusion technique for different ceramic materials and application of the manufactured parts in various industrial and medical fields. However, detailed process-structure studies are still missing. It is critical to investigate the material' microstructure and the physical properties of the ceramic parts made from laser powder bed fusion. It is therefore necessary to explore the relation among the process parameters, the size, shape, and boundary conditions of the laser-fused micro-grains, and the macro-properties of the fabricated part. Such study will increase the understanding of the laser powder bed fusion technique from the micro- to the meso-scale.

## 6. Conclusion

Laser powder bed fusion enables the production of ceramic parts with very high temperatures and excellent precision in a short time. The process is suitable for processing hard materials with complex geometries. However, due to several intrinsic properties, the LPBF technique for ceramics is far from mature and is still in the research and development phase. Limiting factors include susceptibility to thermal stresses, low fracture toughness, and low optical absorptivity in the near-infrared region for oxide ceramics. As these factors are further investigated, the difficulties related to them may be solved. For example, proper choice of lasers and powders, combined with an optimum process, can compensate for or overcome some of the limitations and produce near 100% relative density. Such near pore-free parts have only micro-cracks or no cracks, and their mechanical properties are close to those manufactured from conventional methods. The LPBF technique therefore shows potential for ceramic fabrication and will continue to attract research and industrial interests in the future.

## Author details

Haidong Zhang* and Saniya LeBlanc*

*Address all correspondence to: haidongzhang@gmail.com and sleblanc@gwu.edu

Department of Mechanical and Aerospace Engineering, The George Washington University, Washington, DC, USA

## References

[1] Kruth J, Mercelis P, Van Vaerenbergh J, Froyen L, Rombouts M. Binding mechanisms in selective laser sintering and selective laser melting. Rapid Prototyping Journal. 2005;**11**(1): 26-36. DOI: 10.1108/13552540510573365

[2] Deckard CR. Method and apparatus for producing parts by selective sintering [Internet]. US; US4863538 A. 1986. Available from: https://www.google.com/patents/US4863538

[3] Deckard CR, Beaman JJ, Darrah JF. Method for selective laser sintering with layerwise cross-scanning [Internet]. US; US5155324 A. 1992. Available from: https://www.google.com/patents/US5155324

[4] Meiners W, Wissenbach K, Gasser A. Selective laser sintering at melting temperature [Internet]. US6215093 B1. 1996. Available from: https://www.google.com/patents/US6215093

[5] El-Desouky A, Carter, Andre MA, Bardet PM, LeBlanc S. Rapid processing and assembly of semiconductor thermoelectric materials for energy conversion devices. Materials Letters. 2016;**185**:598-602. DOI: 10.1016/J.MATLET.2016.07.152

[6] El-Desouky A, Carter M, Mahmoudi M, Elwany A, LeBlanc S. Influences of energy density on microstructure and consolidation of selective laser melted bismuth telluride thermoelectric powder. Journal of Manufacturing Processes. 2017;**25**:411-7. DOI: 10.1016/J.JMAPRO.2016.12.008

[7] Deckers J, Vleugels J, Kruth J-P. Additive manufacturing of ceramics: A review. Journal of Ceramic Science and Technology. 2014;**5**(4):245-260. DOI: 10.4416/JCST2014-00032

[8] Liu F-H. Synthesis of bioceramic scaffolds for bone tissue engineering by rapid prototyping technique. Journal of Sol-Gel Science and Technology. 2012;**64**(3):704-710. DOI: 10.1007/s10971-012-2905-5

[9] Wilkes J, Hagedorn Y, Meiners W, Wissenbach K. Additive manufacturing of $ZrO_2$-$Al_2O_3$ ceramic components by selective laser melting. Rapid Prototyping Journal. 2013;**19**(1):51-57. DOI: 10.1108/13552541311292736

[10] Ferrage L, Bertrand G, Lenormand P, Grossin D, Ben-Nissan B. A review of the additive manufacturing (3DP) of bioceramics: Alumina, zirconia (PSZ) and hydroxyapatite. Journal of the Australian Ceramic Society. 2017;**53**(1):11-20. DOI: 10.1007/s41779-016-0003-9

[11] Wang XH, Fuh JYH, Wong YS, Tang YX. Laser sintering of silica sand—Mechanism and application to sand casting mould. International Journal of Advanced Manufacturing Technology. 2003;**21**(12):1015-1020. DOI: 10.1007/s00170-002-1424-x

[12] Bertrand P, Bayle F, Combe C, Goeuriot P, Smurov I, Titov VI. Ceramic components manufacturing by selective laser sintering. Applied Surface Science. 2007;**254**(4):989-992. DOI: 10.1016/j.apsusc.2007.08.085

[13] Shishkovsky I, Yadroitsev I, Bertrand P, Smurov I. Alumina–zirconium ceramics synthesis by selective laser sintering/melting. Applied Surface Science. 2007;**254**(4):966-970. DOI: 10.1016/j.apsusc.2007.09.001

[14] Yeong W, Yap C, Mapar M, Chua C. State-of-the-art review on selective laser melting of ceramics. In: Bártolo P, Lemos A, Pereira A, Mateus A, Ramos C, Santos C, et al., editors. High Value Manufacturing: Advanced Research in Virtual and Rapid Prototyping [Internet]. Boca Raton, FL: CRC Press; 2013. pp. 65-70. DOI: 10.1201/b15961-14

[15] Dalgarno KW, Wright CS. Approaches to processing metals and ceramics through the laser scanning of powder beds—A review. Powder Metallurgy Progress. 2001;**1**(1):70-79. Available from: http://www.imr.saske.sk/pmp/issue/1-2001/PMP_Vol01_No1_p070-079.pdf

[16] Sigmund WM, Bell NS, Bergström L. Novel powder-processing methods for advanced ceramics. Journal of the American Ceramic Society. 2004;**83**(7):1557-1574. DOI: 10.1111/j.1151-2916.2000.tb01432.x

[17] Samant AN, Dahotre NB. Laser machining of structural ceramics—A review. Journal of the European Ceramic Society. 2009;**29**(6):969-993. DOI: 10.1016/J.JEURCERAMSOC.2008.11.010

[18] Wong KV, Hernandez A. A review of additive manufacturing. ISRN Mechanical Engineering. 2012;**2012**:1-10. DOI: 10.5402/2012/208760

[19] Qian B, Shen Z. Laser sintering of ceramics. Journal of Asian Ceramic Societies. 2013;**1**(4):315-321. DOI: 10.1016/J.JASCER.2013.08.004

[20] Shirazi SFS, Gharehkhani S, Mehrali M, Yarmand H, Metselaar HSC, Adib Kadri N, et al. A review on powder-based additive manufacturing for tissue engineering: Selective laser sintering and inkjet 3D printing. Science and Technology of Advanced Materials. 2015; **16**(3):33502. DOI: 10.1088/1468-6996/16/3/033502

[21] Yap CY, Chua CK, Dong ZL, Liu ZH, Zhang DQ, Loh LE, et al. Review of selective laser melting: Materials and applications. Applied Physics Reviews. 2015;**2**(4):41101. DOI: 10.1063/1.4935926

[22] Hegab HA. Design for additive manufacturing of composite materials and potential alloys: A review. Manufacturing Review. 2016;**3**:11. DOI: 10.1051/mfreview/2016010

[23] Sing SL, Yeong WY, Wiria FE, Tay BY, Zhao Z, Zhao L, et al. Direct selective laser sintering and melting of ceramics: A review. Rapid Prototyping Journal. 2017;**23**(3):611-623. DOI: 10.1108/RPJ-11-2015-0178

[24] Kruth JP, Wang X, Laoui T, Froyen L. Lasers and materials in selective laser sintering. Assembly Automation. 2003;**23**(4):357-371. DOI: 10.1108/01445150310698652

[25] Tian X, Sun B, Heinrich JG, Li D. Scan pattern, stress and mechanical strength of laser directly sintered ceramics. International Journal of Advanced Manufacturing Technology. 2013;**64**(1–4):239-246. DOI: 10.1007/s00170-012-3994-6

[26] Triantafyllidis D, Li L, Stott FH. Investigation of the effects of nonconventional beam geometries in laser surface treatment of ceramics: Experimental analysis. Journal of Laser Applications. 2006;**18**(3):267-274. DOI: 10.2351/1.2193522

[27] Wu Y, Du J, Choy K-L, Hench LL. Laser densification of alumina powder beds generated using aerosol assisted spray deposition. Journal of the European Ceramic Society. 2007;**27**(16):4727-4735. DOI: 10.1016/J.JEURCERAMSOC.2007.02.219

[28] Juste E, Petit F, Lardot V, Cambier F. Shaping of ceramic parts by selective laser melting of powder bed. Journal of Materials Research. 2014;**29**(17):2086-2094. DOI: 10.1557/jmr.2014.127

[29] Murali K, Chatterjee AN, Saha P, Palai R, Kumar S, Roy SK, et al. Direct selective laser sintering of iron–graphite powder mixture. Journal of Materials Processing Technology. 2003;**136**(1–3):179-185. DOI: 10.1016/S0924-0136(03)00150-X

[30] Simchi A. Direct laser sintering of metal powders: Mechanism, kinetics and microstructural features. Materials Science and Engineering A. 2006;**428**(1–2):148-158. DOI: 10.1016/J.MSEA.2006.04.117

[31] Kruth J-P, Levy G, Klocke F, Childs THC. Consolidation phenomena in laser and powder-bed based layered manufacturing. CIRP Annals. 2007;**56**(2):730-759. DOI: 10.1016/J.CIRP.2007.10.004

[32] Levy GN, Schindel R, Kruth JP. Rapid manufacturing and rapid tooling with layer manufacturing (lm) technologies, state of the art and future perspectives. CIRP Annals. 2003;**52**(2):589-609 DOI: 10.1016/S0007-8506(07)60206-6

[33] Glardon R, Karapatis N, Romano V, Levy GN. Influence of Nd:YAG parameters on the selective laser sintering of metallic powders. CIRP Annals. 2001;**50**(1):133-136. DOI: 10.1016/S0007-8506(07)62088-5

[34] Shao TM, Lin XC, Zhou M. bsorption of some powder materials to YAG laser. Science in China (Series A). 2001;**44(**Suppl.):489-94. Available from: http://www.scichina.com:8081/sciAe/fileup/PDF/01ya0489.pdf

[35] Pham DT, Dimov SS, Petkov PV. Laser milling of ceramic components. International Journal of Machine Tools and Manufacture. 2007;**47**(3–4):618-626. DOI: 10.1016/j.ijmachtools.2006.05.002

[36] Deckers J, Shahzad K, Vleugels J, Kruth JP. Isostatic pressing assisted indirect selective laser sintering of alumina components. Rapid Prototyping Journal. 2012;**18**(5):409-419. DOI: 10.1108/13552541211250409

[37] Hellrung D, Yeh L-Y, Depiereux F, Gillner A, Poprawe R. High-accuracy micromachining of ceramics by frequency-tripled Nd:YAG lasers. Proc SPIE 1999;**3618**:348–356. DOI: 10.1117/12.352697

[38] Prashanth KG, Scudino S, Maity T, Das J, Eckert J. Is the energy density a reliable parameter for materials synthesis by selective laser melting? Materials Research Letters. 2017;**5**(6):386-390. DOI: 10.1080/21663831.2017.1299808

[39] Tolochko NK, Khlopkov YV, Mozzharov SE, Ignatiev MB, Laoui T, Titov VI. Absorptance of powder materials suitable for laser sintering. Rapid Prototyping Journal. 2000;**6**(3):155-161. DOI: 10.1108/13552540010337029

[40] Li R, Liu J, Shi Y, Wang L, Jiang W. Balling behavior of stainless steel and nickel powder during selective laser melting process. International Journal of Advanced Manufacturing Technology. 2012;**59**(9–12):1025-1035. DOI: 10.1007/s00170-011-3566-1

[41] Das S. Physical aspects of process control in selective laser sintering of metals. Advanced Engineering Materials. 2003;**5**(10):701-711. DOI: 10.1002/adem.200310099

[42] Tolochko NK, Mozzharov SE, Yadroitsev IA, Laoui T, Froyen L, Titov VI, et al. Balling processes during selective laser treatment of powders. Rapid Prototyping Journal. 2004;**10**(2): 78-87. DOI: 10.1108/13552540410526953

[43] Ho HCH, Gilbson I, Cheung WL. Effects of energy density on morphology and properties of selective laser sintered polycarbonate. Journal of Materials Processing Technology. 1999;**89–90**:204-210. DOI: 10.1016/S0924-0136(99)00007-2

[44] Beaman JJ, Barlow JW, Bourell DL, Crawford RH, Marcus HL, McAlea KP. Solid Freeform Fabrication: A New Direction in Manufacturing [Internet]. Springer US: Boston, MA; 1997. Available from: http://link.springer.com/10.1007/978-1-4615-6327-3

[45] Ciurana J, Hernandez L, Delgado J. Energy density analysis on single tracks formed by selective laser melting with CoCrMo powder material. International Journal of Advanced Manufacturing Technology. 2013;**68**(5–8):1103-1110. DOI: 10.1007/s00170-013-4902-4

[46] Liu FR, Zhao JJ, Zhang Q, He C, Chen JM. Processing and characterizations of 2%PF/silica sand core–shell composite powders by selective laser sintering with a higher transmittance fiber laser. International Journal of Machine Tools and Manufacture. 2012;**60**:52-58. DOI: 10.1016/J.IJMACHTOOLS.2012.05.003

[47] Syrjälä S, Tuomi J. Rapid prototyping: Mallien, prototyyppien ja työkalujen pikavalmistus [Internet]. Tekes; 1997. (Teknologiakatsaus/Teknologian kehittämiskeskus TEKES). Available from: https://hamk.finna.fi/Record/vanaicat.41156

[48] Hagedorn Y-C, Balachandran N, Meiners W, Wissenbach K, Poprawet R. SLM of net-shaped high strength ceramics: New opportunities for producing dental restorations. In: SFF Symposium [Internet]. Austin, TX, USA: University of Texas at Austin; 2011. Available from: https://sffsymposium.engr.utexas.edu/Manuscripts/2011/2011-42-Hagedorn.pdf

[49] Liu LX, Marziano I, Bentham AC, Litster JD, White ET, Howes T. Effect of particle properties on the flowability of ibuprofen powders. International Journal of Pharmaceutics. 2008; **362**(1–2):109-117. DOI: 10.1016/j.ijpharm.2008.06.023

[50] Gibson I, Shi D. Material properties and fabrication parameters in selective laser sintering process. Rapid Prototyping Journal. 1997;**3**(4):129-136. DOI: 10.1108/13552549710191836

[51] Gusarov AV, Yadroitsev I, Bertrand P, Smurov I. Heat transfer modelling and stability analysis of selective laser melting. Applied Surface Science. 2007;**254**(4):975-979. DOI: 10.1016/J.APSUSC.2007.08.074

[52] Song JL, Li YT, Deng QL, Hu DJ. Rapid prototyping manufacturing of silica sand patterns based on selective laser sintering. Journal of Materials Processing Technology. 2007;**187–188**: 614-618. DOI: 10.1016/J.JMATPROTEC.2006.11.108

[53] Joguet D, Costil S, Liao H, Danlos Y. Porosity content control of CoCrMo and titanium parts by Taguchi method applied to selective laser melting process parameter. Rapid Prototyping Journal. 2016;**22**(1):20-30. DOI: 10.1108/RPJ-09-2013-0092

[54] Hagedorn Y-C, Wilkes J, Meiners W, Wissenbach K, Poprawe R. Net shaped high performance oxide ceramic parts by selective laser melting. Physics Procedia. 2010;**5**:587-594. DOI: 10.1016/j.phpro.2010.08.086

[55] Deckers J, Meyers S, Kruth JP, Vleugels J. Direct selective laser sintering/melting of high density alumina powder layers at elevated temperatures. Physics Procedia. 2014;**56**:117-124. DOI: 10.1016/J.PHPRO.2014.08.154

[56] Wang Z, Shi Y, He W, Liu K, Zhang Y. Compound process of selective laser processed alumina parts densified by cold isostatic pressing and solid state sintering: Experiments, full process simulation and parameter optimization. Ceramics International. 2015;**41**(2): 3245-3253. DOI: 10.1016/j.ceramint.2014.11.014

[57] Lee RT, Liu FH, Ting KE, Yeh SL, Lin WH. Laser compensation for ceramics accuracy improvement of selective laser sintering. Advances in Materials Research. 2014;**902**:12-17. DOI: 10.4028/WWW.SCIENTIFIC.NET/AMR.902.12

[58] Yap C, Chua C, Dong Z, Liu Z, Zhang D. Single track and single layer melting of silica by Selective Laser Melting. In: Bártolo P, Lemos A, Pereira A, Mateus A, Ramos C, Santos C, et al., editors. High Value Manufacturing: Advanced Research in Virtual and Rapid Prototyping [Internet]. Boca Raton, FL: CRC Press; 2013. pp. 261-5. DOI: 10.1201/b15961-49

[59] Liu J, Zhang B, Yan C, Shi Y. The effect of processing parameters on characteristics of selective laser sintering dental glass-ceramic powder. Rapid Prototyping Journal. 2010;**16**(2):138-145. DOI: 10.1108/13552541011025861

[60] Bertoli US, Wolfer AJ, Matthews MJ, Delplanque J-PR, Schoenung JM. On the limitations of volumetric energy density as a design parameter for selective laser melting. Materials and Design. 2017;**113**:331-340. DOI: 10.1016/j.matdes.2016.10.037

[61] Wilkes J, Wissenbach K. Rapid manufacturing of ceramic components for medical and technical applications via selective laser melting. Conf Euro-uRapid 2006:A4

[62] Zaragoza-Siqueiros J, Medellín-Castillo HI. Design for rapid prototyping, manufacturing and tooling: Guidelines. In: ASME International Mechanical Engineering Congress and Exposition Volume 2A: Advanced Manufacturing. ASME; 2014. p. V02AT02A013. DOI: 10.1115/IMECE2014-39310

[63] Liu Q, Danlos Y, Song B, Zhang B, Yin S, Liao H. Effect of high-temperature preheating on the selective laser melting of yttria-stabilized zirconia ceramic. Journal of Materials Processing Technology. 2015;**222**:61-74. DOI: 10.1016/J.JMATPROTEC.2015.02.036

[64] Liu Q, Song B, Liao H. Microstructure study on selective laser melting yttria stabilized zirconia ceramic with near IR fiber laser. Rapid Prototyping Journal. 2014;**20**(5):346-354. DOI: 10.1108/RPJ-12-2012-0113

[65] Kruth JP, Froyen L, Van Vaerenbergh J, Mercelis P, Rombouts M, Lauwers B. Selective laser melting of iron-based powder. Journal of Materials Processing Technology. 2004;**149**(1–3): 616-622. DOI: 10.1016/j.jmatprotec.2003.11.051

[66] Savchenko NL, Sablina TY, Kul'kov SN. Influence of annealing on the phase composition of vacuum-sintered material $ZrO_2$-3 (mole)% $Y_2O_3$. Powder Metallurgy and Metal Ceramics. 1996;**34**(3–4):167-171. DOI: 10.1007/BF00559562

[67] Exner H, Horn M, Streek A, Ullmann F, Hartwig L, Regenfuß P, et al. Laser micro sintering: A new method to generate metal and ceramic parts of high resolution with sub-micrometer powder. Virtual and Physical Prototyping. 2008;**3**(1):3-11. DOI: 10.1080/17452750801907970

[68] Tang Y, Fuh JYH, Loh HT, Wong YS, Lu L. Direct laser sintering of a silica sand. Materials and Design. 2003;**24**(8):623-629. DOI: 10.1016/S0261-3069(03)00126-2

[69] Su X, Yang Y. Research on track overlapping during selective laser melting of powders. Journal of Materials Processing Technology. 2012;**212**(10):2074-2079. DOI: 10.1016/J.JMATPROTEC.2012.05.012

[70] Wang J, Qian F, Cheng X. Preliminary study on heat-pressed glass ceramic material II. Biological safety evaluation of material. Journal of Comprehensive Stomatology. 2001;**3**:173-175. Available from: http://en.cnki.com.cn/Article_en/CJFDTOTAL-KQYZ200103004.htm

[71] Zhang B, Qian F, Duan X, Wu B. Study on some mechanism of leucite microcrystallization to reinforce dental glass ceramics. Zhonghua Kou Qiang Yi Xue Za Zhi. 2002;**37**(4):260-264. Available from: http://www.ncbi.nlm.nih.gov/pubmed/12411171

[72] Schweiger M. Zirconiumdioxid – Hochfeste und bruchzähe Strukturkeramik. Ästhetische Zahnmedizin. 2004;**5**:248-257

[73] Lammert T. Aluminiumoxid/$Al_2O_3$. In: DKG–Technische Keramische Werkstoffe. Fachverlag Deutscher Wirtschaftsdienst, Köln.; 1992

[74] Burger W. Umwandlungs- und plateletverstärkte Aluminiumoxidmatrixwerkstoffe. (Teil 1). Keramische Zeitschrift. 1997;**49**(12):1067-1070

[75] Frazier WE. Metal additive manufacturing: A review. Journal of Materials Engineering and Performance. 2014;**23**(6):1917-1928. DOI: 10.1007/s11665-014-0958-z

[76] Murr LE, Gaytan SM, Ramirez DA, Martinez E, Hernandez J, Amato KN, et al. Metal fabrication by additive manufacturing using laser and electron beam melting technologies. Journal of Materials Science and Technology. 2012;**28**(1):1-14. DOI: 10.1016/S1005-0302(12)60016-4

[77] Song B, Zhao X, Li S, Han C, Wei Q, Wen S, et al. Differences in microstructure and properties between selective laser melting and traditional manufacturing for fabrication of metal parts: A review. Frontiers of Mechanical Engineering. 2015;**10**(2):111-125. DOI: 10.1007/s11465-015-0341-2

Chapter 6

# Structure and Properties of the Bulk Standard Samples and Cellular Energy Absorbers

Pavel Kuznetcov, Anton Zhukov, Artem Deev,
Vitaliy Bobyr and Mikhail Staritcyn

Additional information is available at the end of the chapter

http://dx.doi.org/10.5772/intechopen.72973

**Abstract**

The development of additive technology revealed a real prospect of their use for the manufacture of complex shapes. Now, it is possible to produce parts that previously were either very difficult to produce using the subtracting technology and joining technology, or it was not at all feasible. In the manufacture of parts of complex shape, it is necessary to use a supporting structure, which is necessary to place such a way that they can be easily removed. Additionally, they must necessarily be absent in certain places. In this regard, the preparation model can take significant time to satisfy all of these, often conflicting, requirements. In this paper, we show optimization examples of the model preparation with support structures for parts manufactured at the facility EOSINT M270 and used in medicine and engineering. Additional emphasis is on the fact that, during the manufacture of parts, solidification's modes of massive parts differ from those of the thin-walled portions of parts. The results of the complex studies on the different stainless steels (including martensitic) are described with an emphasis on their structure and mechanical properties. The results of a honeycomb energy absorbers, which are quite seldom produced by the additive technologies, are presented in this chapter.

**Keywords:** additive technologies, selective laser melting, stainless steel, honeycomb structures, anisotropy, mechanical properties

## 1. Introduction

Since the late 1980s, generative manufacturing methods have been established as manufacturing systems for the product development in various sectors of industries. After only be used for the production of demonstration models (Rapid Prototyping, RP), the rapid tooling and

manufacturing now able to service a steady increasing range of applications. In order to achieve this status, the range of usable materials has been extended. Today, it is possible to process next to the RP area with omnipresent plastics, metallic standard materials, and ceramics. For the processing of metallic materials with the selective laser melting method, no binders or additives are necessary.

Additive manufacturing is a process in which an item is formed layer-by-layer, and taking into account the building principles, the presence of supporting structures is the necessary requirement for the complex shape and geometry items production, which are hard to obtain by classical (traditional) technologies [1, 2]. However, utilizing the supports, in some cases, it increases the time consumption and cost of the final product and it also has an effect on the finish surface treatment [3, 4]. Despite these disadvantages, the main advantage of the supports usage is the fact that it allows some heat output and therefore provides overall integrity especially of the complex elements [5]. Along with the selective laser melting process parameters, an item placement is very important, which itself provides a crucial input in the quality of the final product, as well as its correspondence to the given geometry and sizes [6].

The selective laser melting (SLM) is an additive manufacturing process. Complex components can be generated directly out of powdered metal on the base of CAD-Files. This manufacturing method is used for the manufacturing of tools for the plastic injection molding and the die casting. It is also possible to produce very filigree structures for dental and human implants. Today, diverse applications in the area of rapid prototyping, rapid tooling and rapid manufacturing are found. Currently, there are 10 materials qualified for this manufacturing method. These are high quality steels, titanium-, aluminum- and nickel-based alloys with powder grain sizes between 10 and 60 μm. The producible layer thickness is between 20 and 50 μm. It is possible to achieve a component accuracy of ±50 μm. The processing speed is 5–20 $cm^3$/h depending on the space utilization. The generated parts have a homogeneous structure and a density of almost 100%. Not only the physical but also the mechanical properties of the produced components comply with cast structures.

The manufacturing process of the SLM can be subdivided into three phases, which recur periodically. During the first phase, the substrate plate is lowered by one layer thickness. In the second phase, a new layer is applied on the substrate plate with the help of a coater. In the last step, the powder is scanned by the laser. Due to the absorbed energy, the powder fused at the scanned areas. This procedure will be repeated until the component is completed.

As a result of the layered build-up, the selective laser melting allows the manufacturing of components with hollows and undercuts. The developer gets a huge degree of freedom concerning the part geometry without being limited by restrictions of conventional manufacturing methods. In addition to that, it is possible to integrate multiple functions in the component. Thanks to this great freedom in design, it is also possible to individualize the products and to enlarge the number of variations arbitrary.

In comparison to the indirect laser sintering processes, several process steps can be omitted like in infiltration of the part with other materials. Since the introduction of the SLM process, time-consuming and cost-intensive thermally after-treatments can also be substituted. The whole process chain and thereby the manufacturing time of the product can be reduced thanks to this change. In branches with very short product life cycles, the generated saving of time is a big competitive advantage. Especially in areas in which small lots of little components are required, the SLM process already became a competitive alternative to the conventional manufacturing methods. The metallic substructure of dental crowns can be manufactured with the help of the SLM process within 48 hours. In the SLM, the complexity of a component has only a low effect on the unit costs, because the costs of this process are more volume- than geometrical-based. The parts with a high degree of complexity are particularly suitable for the SLM, because its manufacturing with conventional processes is either very cost intensive or not possible.

Currently, SLM is used to manufacture functional prototypes and to build up final parts directly. In this case, the field of commercial applications is limited to single parts or parts in small batches. The tool- and mold-making industry is a typical example of a branch producing final parts in small batches of approximately one to eight. Because of the almost infinite geometrical freedom, SLM is applied to manufacture tooling inserts containing conformal cooling channels. Thanks to SLM, an improved tool cooling can be attained, resulting in reduced cycle times and improved part quality. As a result, the rapid manufacturing method SLM offers massive cost savings in combination with better functionalities despite the higher manufacturing costs for small batch production. Medical technology is another area applying the infinite geometrical freedom and variability of SLM. According to the current state of the art, individual implants in a batch size of one are manufactured with SLM. Typical examples of application are hip implants or surgical instruments out of titanium alloys as well as dental restorations out of cobalt chromium. Compared with conventional manufacturing methods like for example casting, SLM can significantly decrease the processing time and the production costs. Furthermore, the given geometric freedom can be used to manufacture implants with new functionalities such as hollow structures, graded porosity, adapted rigidity or surface structure.

Laser melting from metallic powders is a free form fabrication method causing great interest in the past decade. It has been reported recently that selective laser melting (SLM) using different alloys and steel powders is suited to create geometrically complex commercial components [7, 8]. Several reviews on SLM fabrication of 316L stainless steel were published [9, 10]. The influences of power, scanning speed, hutching, building direction on the microstructure and mechanical properties of fabricated 316L specimens have been studied; many researchers report on the effect of the material characteristics such as chemical composition, particle shape, size, and its distribution on laser melting of 316L stainless steel powder [10–12]. At present time, it is evident that SLM is a parameter sensitive process, and therefore for better understanding of these technology possibilities, it is necessary to get more information about mechanical and structural properties of standard specimens.

In the last years, additive technologies achieved a rapid boost, due to the requirements of the modern industry, including the increased productivity, achieving better properties and also lowering the technical and economic costs[13, 14]. Additive technology methods, specifically the SLM,

are widely used for the complex shape items and structures functional elements production [15]. Along the wide diversity of the metal powder materials, based on the stainless steels, which are commonly used in the SLM process, the martensite grade steels should be identified separately, because they are characterized by the non-equilibrium martensite structure and the inner stresses presence. A special interest is evoked, in case the SLM method utilization, by the 410L stainless steel, which represented by the quite simple chemical composition, that allows avoiding high segregation heterogeneity, although, the presence of a double $\alpha$-$\gamma$ transformation, requires special approaches for the 410L-based items production. Therefore, one of the main scientific objective, which is need to be solved, regarding the usage of martensite grade steels is an appraisal effect of the main technological parameters of the SLM process on the structure and mechanical properties of the producing items, because an overall integrity can only be achieved by utilizing an optimal methods and process parameters [16]. In addition, there is a necessity to implement an additional heat treatment, because of inner stresses and overall structure heterogeneity of the samples at the origin state after the laser melting process. In this connection, it seems important to try to find out whether it is possible to change the dispersion of the powder, the thickness of the melted layer, as well as the heat-input modes of its fusion to achieve a lower anisotropy.

Manufacturing of the cellular or thin-walled structures by the SLM is of a great scientific and practical interest [19]. It belongs to the fact that this approach allows to produce structures practically of any configuration and thickness, that is unobtainable or hard to achieve by the traditional methods [5]. Due to the possibility to obtain high values of specific mechanical and deformational properties in cellular or thin-walled structures, this kind of material is perspective to use in different areas: medicine, transport, machinery, aviation industries, etc.

Thin-walled cellular energy absorbing materials are widely used in different industry areas for the efficient energy damping in cases when it is necessary to immediately stop high speed transport vehicle. Based on the cellular structure of the energy absorber material, it is possible to manage the stop distance and maximum load [20–22].

We will start with a complex overview of methodological principles of the proper item placement (Section 2) during the building process. It will determine the future structure and mechanical properties of the produced items. In Section 3, we will determine the optimal SLM parameters to obtain the necessary properties of the common stainless steels like 316L, 321 and 410L. Also, it will be shown that there is a necessity to implement a heat treatment for the martensitic steels, allowing to increase overall mechanical features. And a short, Section 4 will highlight the possibility of obtaining the complex-shaped items like hexagonal energy absorbers and discuss structure and absorbing properties, implementing a quite amount of scientific investigations.

## 2. Methodology of choosing the proper item placement during the SLM process

One of the most complex areas during the item production is the inner hollows, access to which for the mechanical treatment is impossible. In this case, it is obligatory to place the item in such a way that there will be a possibility for the future treatment if it is necessary.

At first, let us describe the variants of supports placement and building on the example of two items: curved tube and micromotor, traditionally used in medicine area.

For the first example, let us take a look on the tube sample production approaches. It is well known that the time consumption of item manufacturing increases in proportion to its height. Therefore, the first and most obvious solution will be a horizontal item placement (**Figure 1a**). However, while producing an item, it is necessary that the inner surface of the curved tube will provide minimum defects quantity, and in case in their presence, there should be a possibility for their access and removal. Taking it into account, other placement variants will also occur unsuitable (**Figure 1b**, **c**) because of the defects formation on the curved area of the item (indicated by the black colored marker).

Therefore, it is stated that the only one suitable placement variant, providing the compromise, is the one presented in **Figure 1d**.

It should be mentioned that during the item preparation (designing), it was constantly advised to place supports inside the horizontal part of the tube and also on the outer side of the inclined part of the tube. While they are removed or shortened, the program has given the error notification. An image of the ready-to-use item is presented in **Figure 2**.

Another common problem during the item production is the support minimization. Also, it is preferable that the supports are absent in the places where after the production cycle it is practically impossible to perform the mechanical treatment because of the possibility to damage the items surface. As the second example, let us take a look at the micromotor sample. During

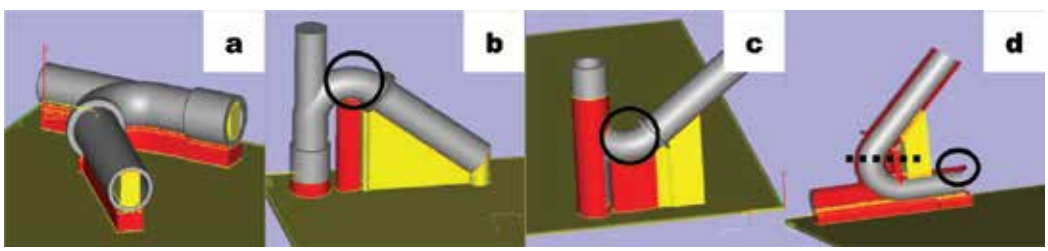


**Figure 1.** Examples of the supports disposal and "problem areas" indicating for the curved tube sample (a – supports inside the tube; b and c – circled areas, which are hard to complete using SLM; d – optimal item disposal).


**Figure 2.** An image of mechanically treated curved tube sample after the SLM process.

the production of such kind of items, it is necessary to provide the support absence on the micromotor blade surface.

Estimating the provided 3D model, it should me mentioned that the blades in their joints with the lower part have the limiting angle less than 45° (**Figure 3**), and at the same time, the necessary requirement is that the support is produced along the blade, until the angle will be 40° or more at its best, for better item production. Taking into account that the blades have enough thickness related to their height, therefore enough toughness, it is necessary to strengthen them and protect from the mechanical effect from the ceramic blade, performing the powder layer by designing the circuit support, beginning from the top part of the item and ending on the platform and the most important—that the circuit support should be adjoined with the blade edge (**Figure 3**). Under such requirements of the blade and the vertical support, an overall rigidity of the structure is increasing, providing the better chances for the item production (**Figure 3**).

Therefore, a proper item placement for the building process and supports placement optimization are the guarantee of a complex shape item qualitative production. At the present time, it is practically impossible to carry out such optimization using software options. The final decision is up to designer.

### 2.1. Structure features of the complex shape items produced by the SLM method

After the item building has finished, the first and major step is to investigate its quality and structure.

For the curved region, the micro sections were obtained in two planes: parallel and normally to the building plane of the sample. The structure images of the pipe sections are presented in **Figure 4**.

The structure analysis showed that in this case there are not many differences between the sample transverse and longitudinal cuts. All the pictures in **Figure 4** represent a quite uniform structure, despite the presence on a small amount of pores. In general, an important thing lies in the areas near the sample edges (especially the bottom part). In all the cases, the structure distortion is observed and the porous contamination is drastically increased. The maximum

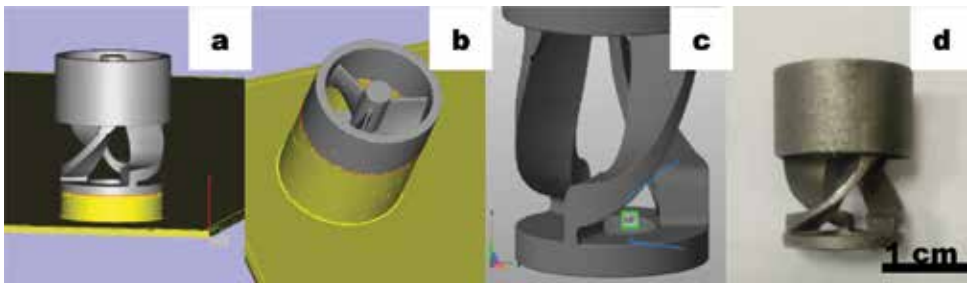


**Figure 3.** Different supports disposals and the limiting angle for the micromotor sample with the mechanically treated item (a – supports placement on the bottom part; b – optimal supports disposal; c –item after supports removal (the angle value on picture is 25°); d – mechanically treated item.

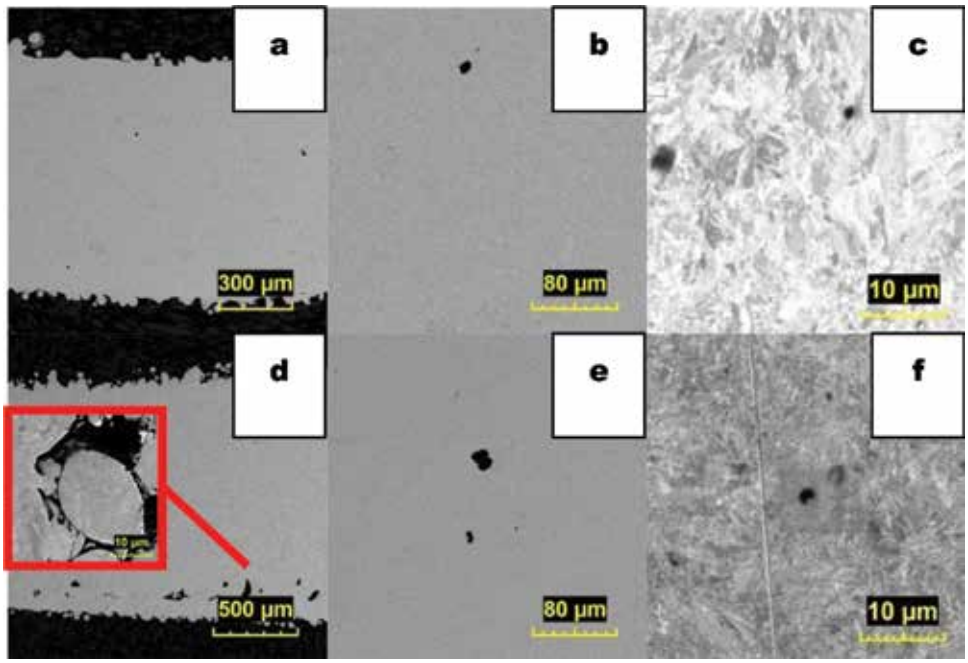


**Figure 4.** SEM structures obtained on the curved part of the tube: a, b, c—transverse cut; d, e, f—longitudinal cut (the scale in the red incut is 10 μm).

pore size is about 30–40 μm. It should be mentioned that the most part of the pores accumulates in the beside-contour layer.

As in **Figure 4**, the structure in its transverse direction practically does not differ from what we can see in **Figure 4a–c**. Separate crystallites are observed; an overall continuity is not violated; however, a small amount of pores is presented. Another pattern is observed on the longitudinal cut where porosity seems to be increased, and the pores in some cases consist from the unmelted components of the raw material (incut in **Figure 4d**).

Taking into account recommendations regarding the tube sample placement, according to the given variant in **Figure 1d**, the necessity occurred to perform investigations on the "problem area," marked with black circle. The main feature of this area is that during the selective laser melting process, the top part of the tube basis is closing up and there is a possibility to obtain some structure changes (**Figure 5**) because of the increased heat input.

The investigated area (around 1 cm width) is characterized by the irregular structure presence and a quite big amount of pores, up to 20 μm, which increases in case of longitudinal cut with some areas of "crumbly" structure, where along with the pores the unmelted particles of the raw powder materials are presented. During the SEM analysis, we also calculated the porous contamination in both cases. The lower amount we achieved is 0.8% on the transverse cut and the highest is 6.4% on longitudinal cut (**Figure 5b**, **d**; yellow color markers).

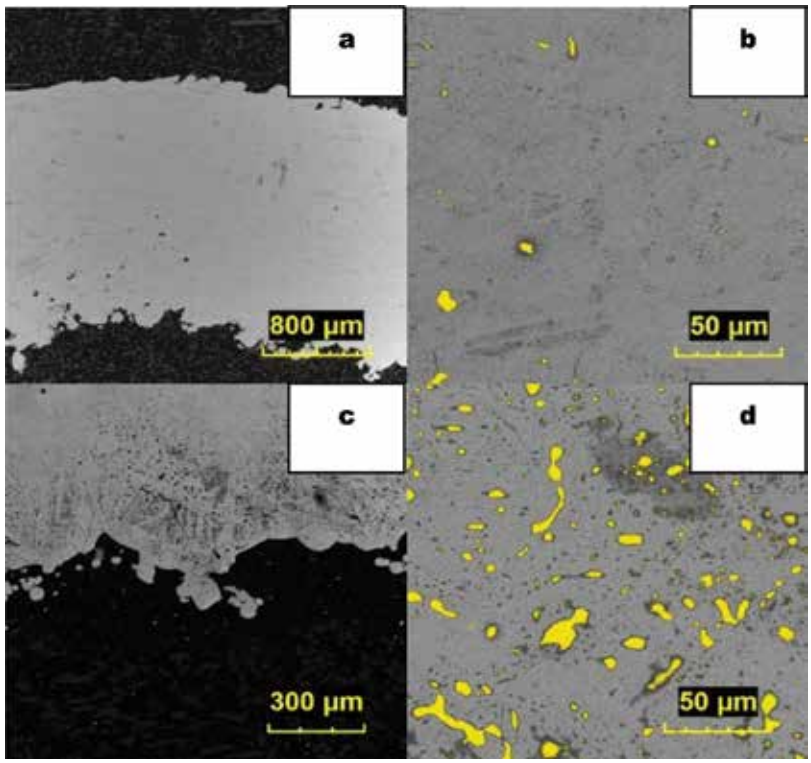


**Figure 5.** SEM structures obtained on the "problem area" of the tube: a, b—transverse cut; c, d—longitudinal cut.

As per the chosen items of curved tube and micromotor, an analysis of their proper placement and supports was carried out. It is stated that in case of the curved tube there is only one suitable disposal, since there will be no defects on the inner surface and the future mechanical treatment of these areas is drastically simplified. For the micromotor sample, we have found that there is a solution for building and elements under the 250 angle by the proper optimization of the supports placement. The porous content is changing in the range between 6.4 and 0.8%.

## 3. Structure and mechanical properties of austenitic and martensitic steel samples after SLM process

For estimating the mechanical properties, models for the uniaxial tension (ASTM E8) and impact strength (ASTM D6110) tests were designed and simultaneously to each other were manufactured on a single platform under nitrogen shielding atmosphere. Samples for the uniaxial tension had the working body diameter of 5–6 mm. Impact strength samples were produced with the square section of $10 \times 10$ mm$^2$. Horizontally built samples were already manufactured with the U-shaped notch in two ways (**Figure 6**). The notch on the vertically built samples was made during the finishing mechanical treatment. Three samples were made for each type of mechanical testing.

To investigate the building parameters effect, we have chosen three stainless steel-based powders: two austenitic (316L and 321) and one martensitic (410L). SEM images of the powder and their granular distribution are presented in **Figure 7**.

It is seen that for the 410L and 316L powders the distribution is thinner that for the 321 steel, which can affect on porosity and other properties during the items production. In **Figure 8**, the

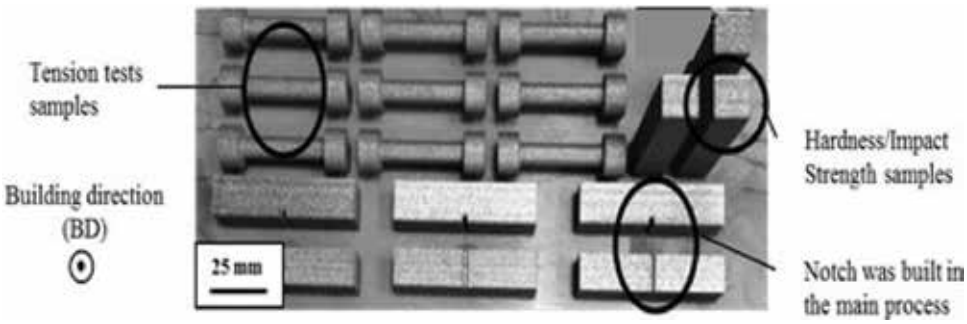


**Figure 6.** Platform fragment showing the samples placement.

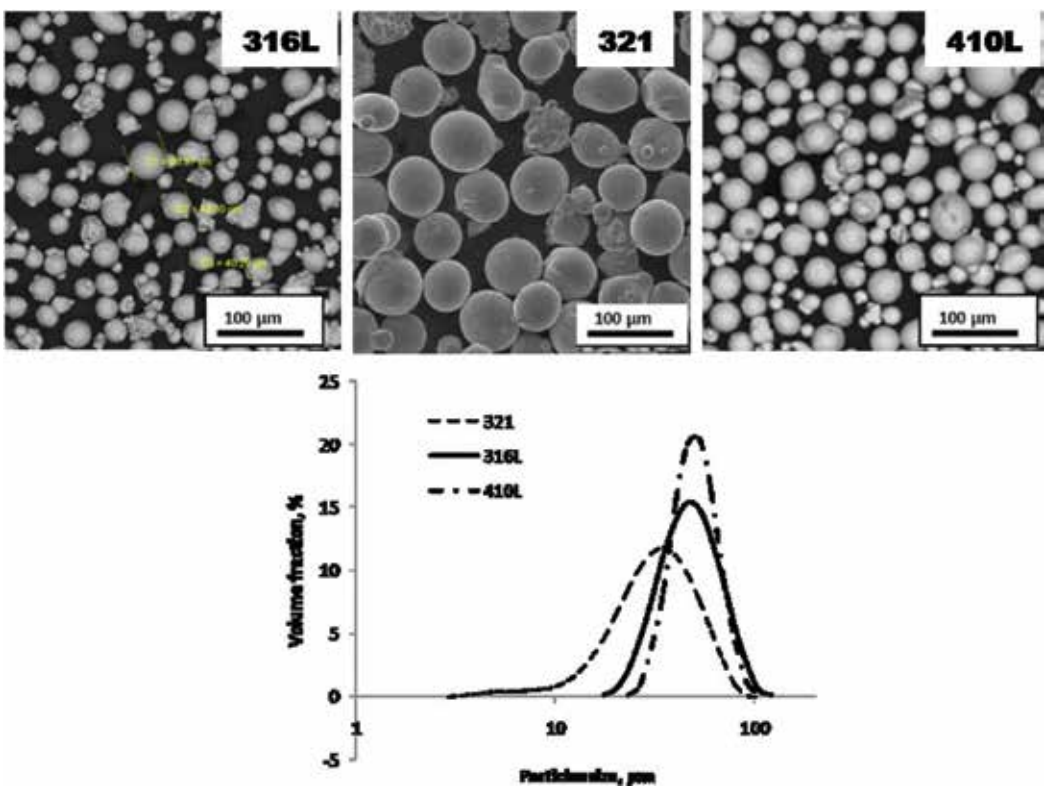


**Figure 7.** SEM images of the stainless steel powders and their granular distribution.

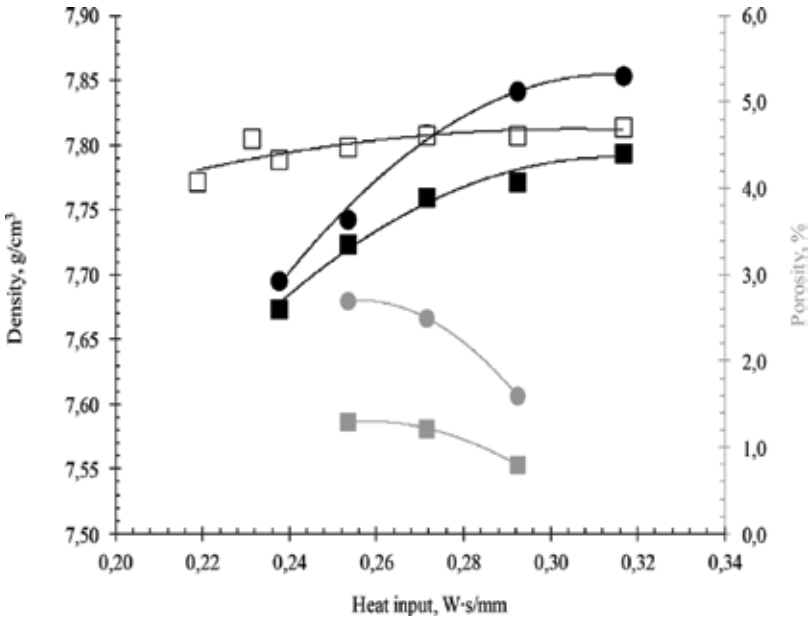


**Figure 8.** Dependences of the density (black lines) and porosity (gray lines) of steel samples vs. heat input; colored square symbols—Steel 321, layer thickness 40 μm; open square symbols—steel 321, layer thickness 20 μm; colored round symbols—316L steel, layer thickness 40 μm.

effect of layer thickness and level of energy input (calculated as a relation between laser beam power and scanning speed) for the 316L and 321 steels are presented.

The density and porosity of the samples are shown in **Figure 8**, from which it can be seen that the thickness of the melted layer significantly affects both characteristics. The smaller values of the density of samples, built at a 40-μm thick layer, can be explained by the presence of a larger number of pores and other inclusions. For samples from a larger 316L steel powder, the density increases more slowly with increasing heat input than in samples of a smaller 321 steel powder. It can also be concluded that the density values at 20 μm are closer to those for materials obtained by traditional metallurgical methods.

The results of the KCU tests for samples of 20 and 40 μm are shown in **Figure 9**, and a number of conclusions can be drawn from them. First of all, the KCU increases almost linearly with increasing energy input. In the range of values from 0.22 to 0.3 W s/mm, the anisotropy of KCU is maintained between horizontal and vertical samples. Secondly, samples from a larger powder of 316L steel obtained with a 40-μm thick layer, with increasing energy deposition, do not reach the same impact characteristics as the same obtained with a layer thickness of 20 μm. Samples of fine steel powder 321, formed with a layer thickness of 40 μm, possess the same impact properties as the samples formed with a 20 μm thick layer, with an increase in energy deposition by 1.5. Consequently, when using a larger powder, the growth of any parts with a layer thickness of more than 20 μm is not feasible.

It should also be noted that the KCU of the samples is 2–3 times lower than that of the samples from the same steels obtained by thermomechanical treatment. On the one hand, this may be

http://dx.doi.org/10.5772/intechopen.72973

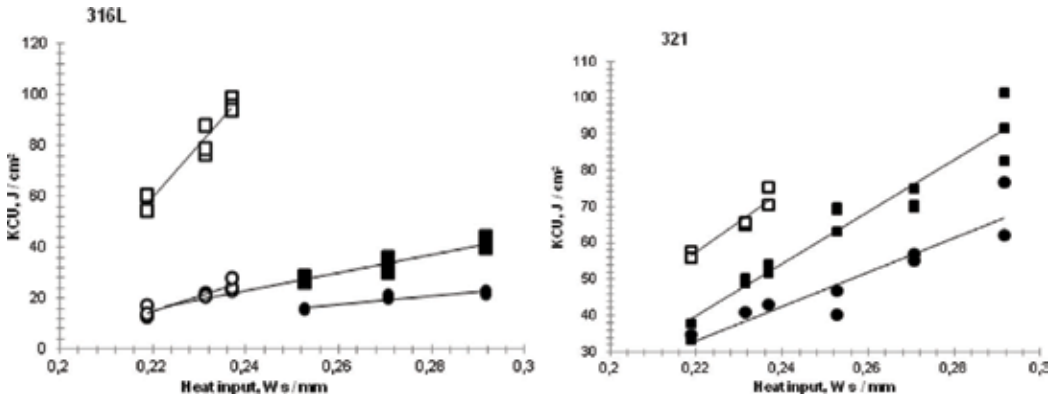


**Figure 9.** Dependences of the KCU of steel samples vs. heat input; square symbols—horizontal samples; round symbols—vertical samples, colored symbols—layer thickness 40 μm; open symbols—layer thickness 20 μm.

due to the fact that the notch of horizontal samples was applied in the model and formed during the building process. Taking into account the fact that in the building process the contour of the future layer is firstly melted by the laser, and then the layer itself is hatched, the microstructure of the contour layer will differ from the microstructure of the hatching layers. Thus, the KCU of a specimen with a mechanically made notch will be higher than that of a specimen with a grown notch [17]. However, even under such unequal conditions of testing, a rather large anisotropy is observed. On the other hand, this may be due to the presence of the pores in the samples of such dimensions that can affect the initiation of the crack during impact tests.

The results of mechanical tensile tests are shown in **Figure 10**. It can be seen that the anisotropy of mechanical properties is also preserved in all cases. To achieve the same mechanical properties at a thickness of the melted layer of 20 and 40 μm, it is necessary to increase the energy input by a factor of 1.5–2. It is noteworthy that the elongation of samples from steel 321 with increasing energy input to 0.27 and higher is no longer dependent on the building direction and comprise about 30–35%. This confirms that the presence of particles in the powder less than 20 μm positively affects the formation of mechanical properties.

A martensitic-based steel (410L) is standing beside the aforesaid ones due to the presence of a couple phase transformations, which can lead to some unacceptable results.

For the 410L steel, the hardness values measured on the sides of the standard samples showed that this property is independent from the samples disposal on the platform and it is linearly increasing with evaluation of the laser emitting power. The maximum hardness value was achieved at 190 W laser power and composed around 230 HB, which is more than the standard values for this type of steel around 195 HB. These hardness values (exceeding the standard ones) indicate the presence of residual stresses inside the structure.

It should be mentioned that the impact strength values of the as-build samples are practically independent of the U-shape notch disposal and laser power, composing meanly 5–6 J/cm$^2$. Herewith, after the heat treatment, these values are increasing linearly with the laser power growth from 17 to 32 J/cm$^2$, i.e. 3–6 times rise (**Figure 11**).

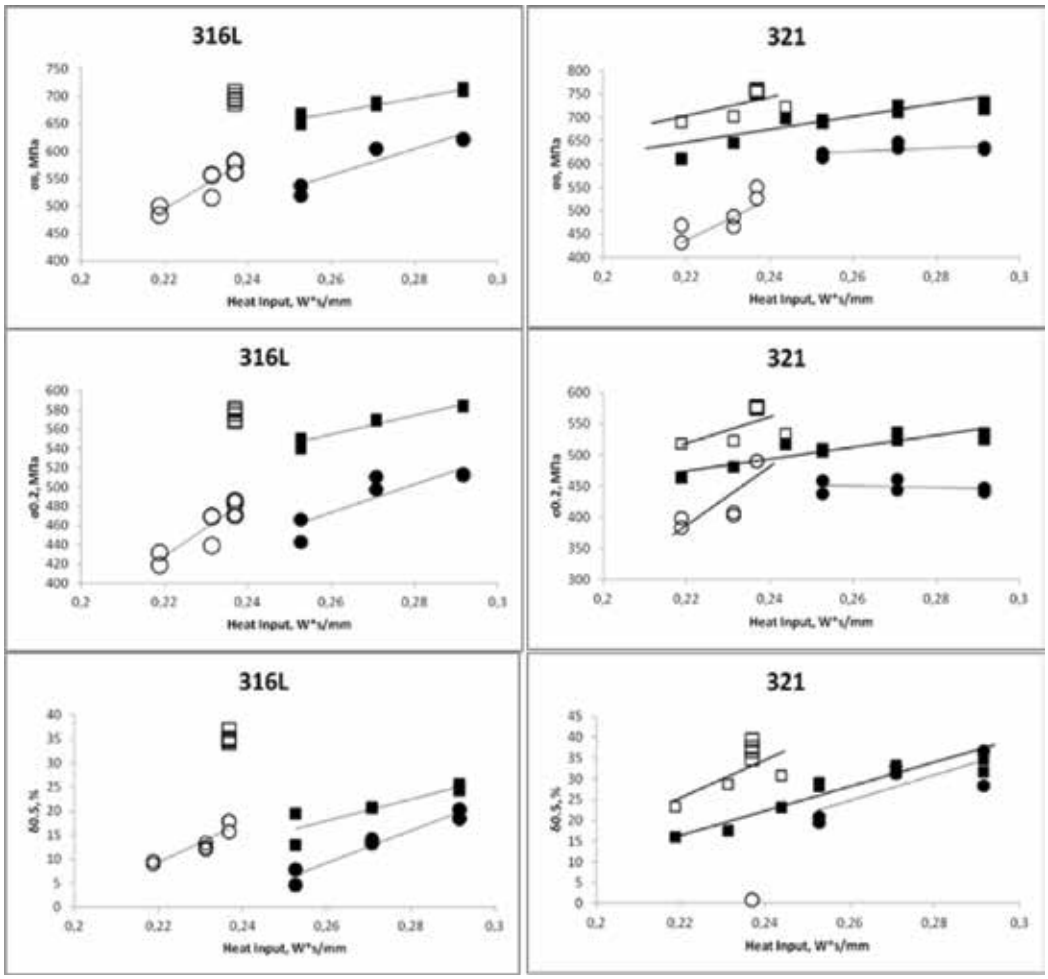


**Figure 10.** Dependences of the yield strength, tensile strength and elongation of samples from 316L and 321 steel from energy deposition made at a layer thickness of 20 and 40 μm; square symbols—horizontal samples; round symbols—vertical samples; open symbols—layer thickness 20 μm; colored symbols—40 μm.

The uniaxial tension tests of the as-build samples disposed horizontally and normally showed that in the last case, destruction is performed not by the samples body but in the attachment point. Drastically low values of relative elongation and diameter reduction are achieved, comprising 1.5 and 3.2%, respectively (**Figure 12c**). A completely different case was observed on the horizontally built samples, in which the tension occurred in the center of the sample body. It can be assumed that this is due to the structure as well as properties anisotropy of the additive material, depending on the samples disposal during the SLM process [17]. Presumably, such unsatisfactory values can be the result of the structural heterogeneity after SLM process.

For the horizontally built samples, the chart of the ultimate tensile strength (UTS), yield strength (YS) and relative elongation dependences from the laser emitting power is presented

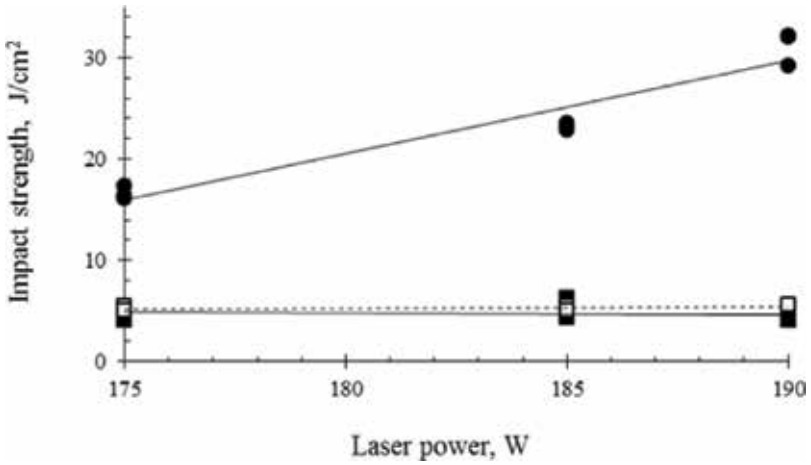


**Figure 11.** Impact strength dependency (prior and after heat treatment) from the laser power: square symbols—prior heat treatment (colored markers—notch in the building plane; open markers—notch normally to the building plane); round symbols—after heat treatment, notch in the building plane.

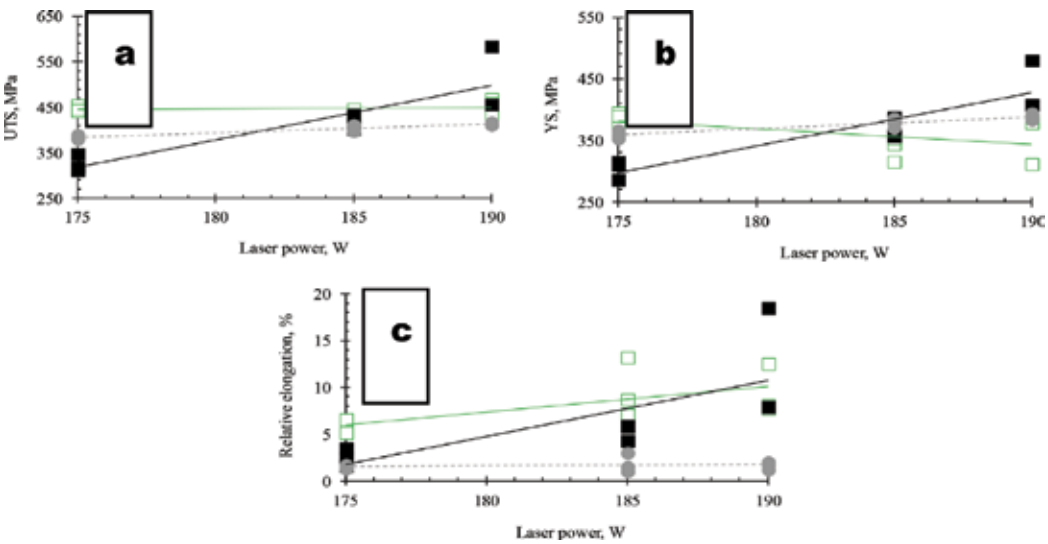


**Figure 12.** Strength properties dependency from the laser emitting power. Colored symbols—without heat treatment; opened—heat treated. Square symbols—horizontally built samples; round—vertically built samples (a – ultimate tensile strength dependency; b – yield strength dependency; c – relative elongation dependency).

in **Figure 12**. As it seen, the dependency is approximately linear and the values are increasing simultaneously with the laser emitting power.

The measured values of mechanical properties in the as-build state also correspond to the residual stresses, which drastically lower these numbers The possible way out of this problem is to implement a heat treatment. In this review, we have chosen to perform 2 cycle oil quenching-tempering treatment for trying to avoid the inner stresses content.

The carried out heat treatment (quenching and oil tempering), in general, allows increasing the UTS values, which are stay constant at the level of 450 MPa, independently from the laser emitting power (**Figure 12a**). The YS in contrary with the UTS is increased only at 175 W power. After further power growth, the investigated property value lowers, providing a linear tendency (**Figure 12b**). Also, a growth in the relative elongation values is observed in comparison with the nonheat-treated samples, which indicates on the deformational ability improvement of the material.

The similar increase of the KCU values occurred also after heat treatment (**Figure 11**). The maximum value is 30 J/cm$^2$ that corresponds to the requirements on this type of steels.

The performed mechanical tests and the achieved results showed that after the SLM process the structure state could be characterized by the inner stresses presence, which has an effect on properties, specifically on the impact strength. Providing the heat treatment allows removing the crystalline lattice distortions by the quenched martensite decay and lattice tetragonality rate lowering.

### 3.1. Samples structure

Structure investigation of the 316L and 410L steel was performed on the micro sections taken from the cross-cut of the specimens after testing.

**Figure 13** shows layer-expressed austenitic structure, thickness and width of which are about 100 μm, which is 2.5 times more than the thickness of the powder layer and initial particle size. Also "big" grain's creeping is seen over the layer boundary, where non-metal (silicon and its oxides) inclusions are presented. One can say that the heredity of the orientations comes from layer to layer during the crystallization on the boundary.

A sample, obtained by the SLM process is characterized by the quasi-regular lamellar structure, that is specified by the fluctuations of chemical composition in the melt and crystallization areas. On the micro-sections in the EBSD analysis, an cambered with 20 ± 10 μm period crystallization fronts are observed, caused by the temperature pulsations and concentration heterogeneities (**Figure 14a**).

During the crystalline orientations, the transition zone, consisting of epitaxial layer and primary crystals, is not observed (**Figure 14a**). The orientation lines indicate only the contours of

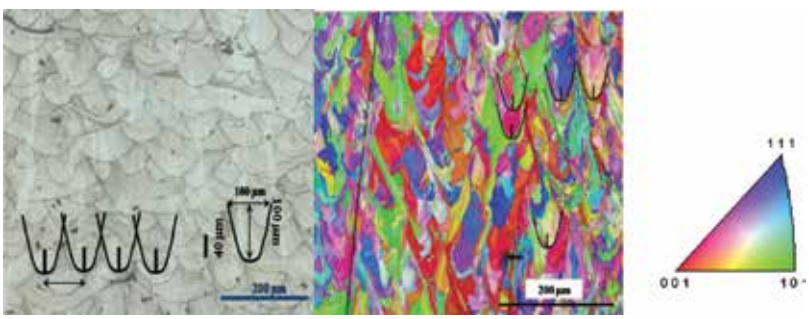


**Figure 13.** SEM and EBSD structures of the 316L-based sample after the SLM process.

http://dx.doi.org/10.5772/intechopen.72973

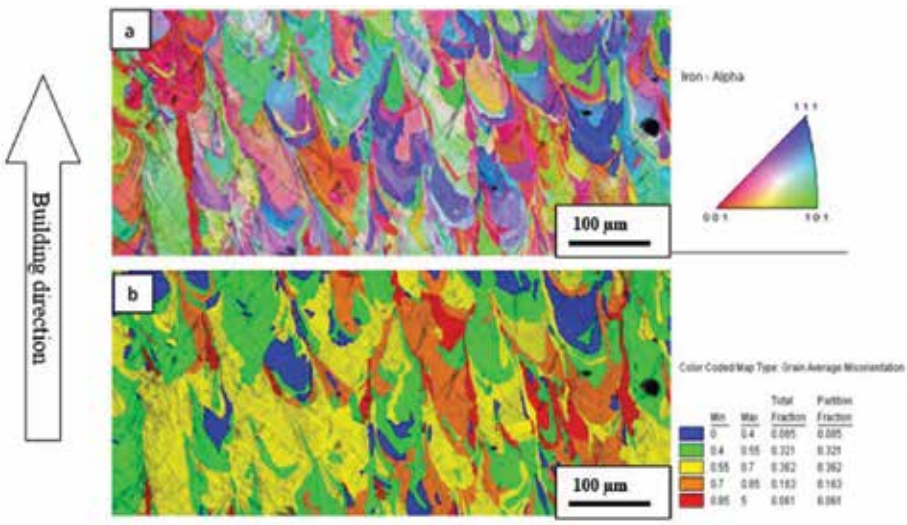


**Figure 14.** EBSD structures of the 410L-based sample after the SLM process (a – crystalline misorientations map; b – residual deformations map).

the powder melting zones. Because of the epitaxial growth of the crystals, formed during the solidification from the melt zone, it is occurred that the size of the primal crystals is moving towards the size of the origin powder particles. The crystalline size along the building direction is multiple times overcoming the depth of the melted layer. The misorientation character of the 410L steel grain boundaries is similar to the disorientations for the martensite steels, produced by the traditional technologies. The mean Ferre diameter and elongation of a single crystal are 68.17 and 0.289 μm, respectively. The bigger crystalline chords are orientated predominantly by ±20° with respect to the samples building direction. Within the crystallites, the disorientations of marked crystallographic directions are not exceed 5°.

**Figure 14b** represents the map of the residual deformations of the 410L-based sample in its as-build state (after SLM process), which confirms the inner stresses presence (red colored areas—quenched martensite) [18]. It should be mentioned that the blue colored areas, where the hardening is practically absent (tempered martensite area), are not common for the martensite steels; therefore, the problem of their presence in the structure is still unsolved. Phase analysis by the EBSD method shows that steel saves its one-phase austenitic structure, as no ferrite (alpha-phase) contents were detected.

In general, the EBSD analysis of the samples, produced by the SLM method, showed the obtaining the structure that is uncommon compares to the traditional methods of production. The "distinctive" feature of the structure such as grain epitaxial growth and their creeping over the layer boundary determines the final properties and overall quality of the product.

The carried out complex investigation of varying mechanical properties in dependence with laser power and mutual disposition with respect to the BD occurred to be quite important in case of determining the properties anisotropy. This fact on its turn will determine further utilization of these technologies in case of designing and producing more complex details and components of different machinery.

## 4. Cellular energy absorbing structures, produced by the SLM method

Traditionally, the cellular energy absorbers are produced from the thin corrugated sheets, joined to each other by different methods of gluing or welding [8, 20–22]. While using the additive technology, the main difference from the traditional one is that the cellular elements can be produced practically of any shape and the method itself is 100% waste-free, because no additional support structures are needed.

Samples with different wall thickness were modeled using CAD software. The 3D model of the honeycomb samples consists of 85 regular hexagons with the side length of 2.5 mm, stacked one to another and inscribed into the circle of 44 mm diameter (**Figure 15**). The height of the samples is 44 mm.

Prior the start of the compression tests, the structure of the samples was investigated. The common view of the hexagonal element with the wall structure of the samples from the side of electro-erosion cut and the EBSD structure analysis are presented in **Figures 16** and **17**, respectively. It is seen that the thin-walled element is produced quite well. The walls are connected under angle 118–1220. The wall thickness is uniform, and no deviations or "waviness" are observed. With the higher magnification, it is assured that the heavy expressed pores are absent. Also on the wall surface, it is clearly observed that a big cluster of small powder particles (less than 10 μm) always join the wall during the scanning process of the powder surface by the laser beam. Notably, particles of size more than 20 μm are absent on the surface.

Analyzing the EBSD maps, provided in **Figure 17**, we can make an assumption that the crystalline structure features are in relation with the building conditions. On the right picture, the changing of the structural state from the item surface to the center of the honeycomb element is noticed. As an example, a fine-crystalline structure in the contact zone between the melted item and powder raw material can be explained by the smaller powder particles gluing to the surface during building process. With the increasing distance from the item boundary deeply to the honeycomb joint, the temperature gradient lowers; therefore, the amount of grains per area unit

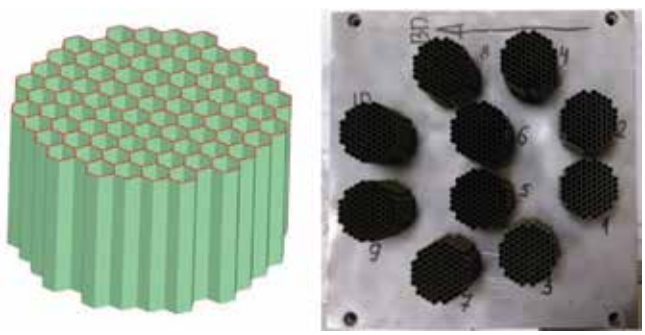

**Figure 15.** 3D-CAD model (on the left) and the produced samples on a single platform (on the right).

http://dx.doi.org/10.5772/intechopen.72973

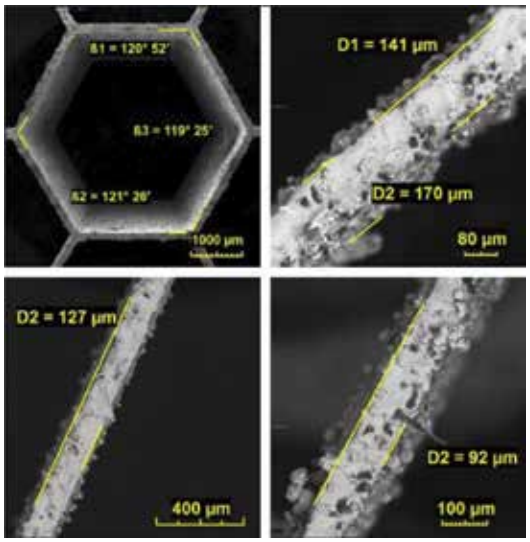


**Figure 16.** A typical view of the hexagonal element (on the left) and walls with different thickness (170, 127 and 92 μm).

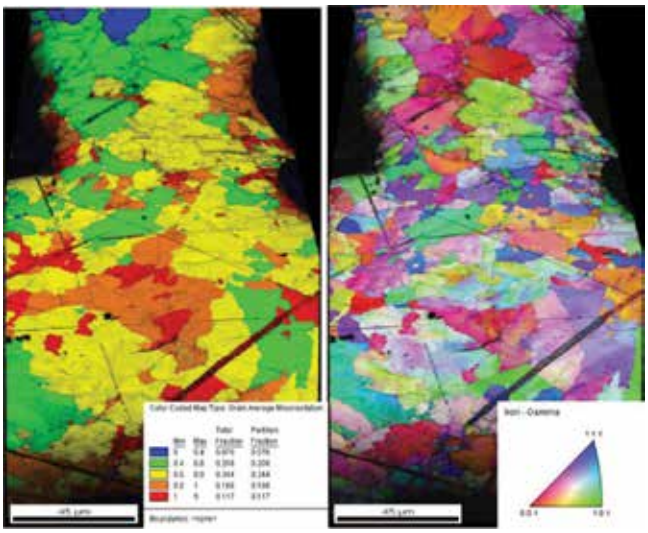

**Figure 17.** EBSD analysis of the central part of the honeycomb element.

also lowers. Moreover, in the results of EBSD maps analysis, we noticed an area in the centre of hexagonal structure joint (left picture) where the bending (misorientational) effect is prevailing. Such intergrain misorientation effect can be due to the elastic-plastic deformation and irregularity of the heat fields, affected by the laser beam scanning strategy during the melting.

An exterior of the samples after the compression tests and compression dependencies are presented in **Figure 18**.

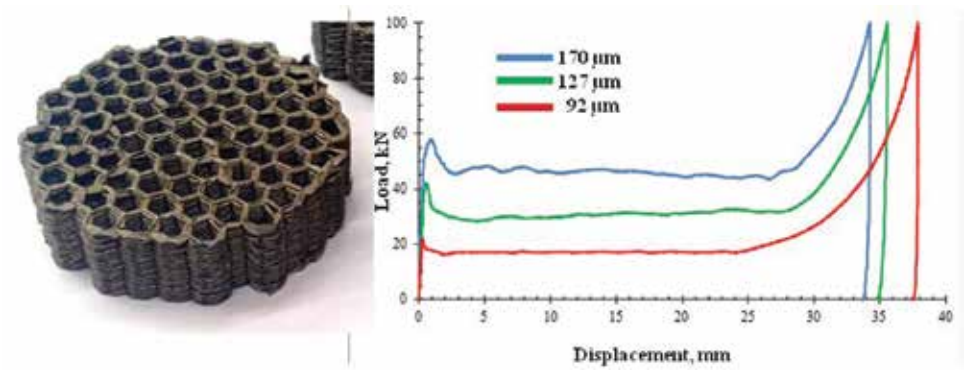


**Figure 18.** A typical view of the samples after compression tests (on the left) and load vs. displacement dependencies (on the right).

It can be seen that the samples were destructed uniformly without the size expansion. The reason can be the fact that during the samples compression process the uniform localized folding took place. The compression dependencies are looking familiar for these types of objects—a peak, corresponding to the activation load and a pace area, corresponding to the uniform destruction mode.

Crush force efficiency (CFE) is an important parameter to evaluate the performance of the structure during the crushing process, which is calculated as the ratio of activation load to compression load [23, 24]. Calculation CFE gives almost constant value from 0.7 to 0.8 that allows considering these structures as a good quality material produced by the selective laser melting [20–22].

Based on the example of the cellular structures, it was shown that utilization of additive technologies allows obtaining a material with high performance mechanical properties comparable to the traditional corrugation technologies. The minimum wall thickness is 92 μm.

## 5. Summary

This chapter has illustrated several complex challenges, facing which is common fact when utilizing additive technologies, more specifically—selective laser melting of metallic powders. It has been shown that there is only one suitable positioning of the item and its supports, which increases an overall quality and properties of the final product. Also, we have discussed a possibility to obtain samples from the different steel grades and pointed out the difficulties, occurred on the martensitic steel. Complex analysis of the mechanical testing results showed that the SLM-built samples provide increased mechanical properties compared to the traditionally manufactured (e.g. casting) ones. The structure obtained through the SLM process is uncommon to the standard structures of austenitic and martensitic grade steels. Production of the thin-walled honeycomb elements with the energy absorbing feature seems quite perspective, providing a waste-free technology with a results comparable to other manufacturing methods.

## Acknowledgements

This work was supported by the grant of Russian Scientific Fund 15-19-00210.

## Author details

Pavel Kuznetcov*, Anton Zhukov, Artem Deev, Vitaliy Bobyr and Mikhail Staritcyn

*Address all correspondence to: kspavel@mail.ru

National Research Center "Kurchatov Institute" – Central Research Institute of Structural Materials "Prometey", Saint-Petersburg, Russian Federation

## References

[1] Vaidya R et al. Optimum support structure generation for additive manufacturing using unit cell structures and support removal constraint. Procedia Manufacturing. 2016;**5**:1043-1059

[2] Gardan N et al. Topological optimization of internal patterns and support in additive manufacturing. Journal of Manufacturing Systems. 2015;**37**(1):417-425

[3] Gan MX et al. Practical support structures for selective laser melting. Journal of Materials Processing Technology. 2016;**238**:474-484

[4] Jarvinen J-P et al. Characterization effect of support structures in laser additive manufacturing of stainless steel. Physics Procedia. 2014;**56**:72-81

[5] Das P et al. Optimum part build orientation in additive manufacturing for minimizing part errors and support structures. Procedia Manufacturing. 2015;**1**:343-354

[6] Manzhikov AV. Advances in theory of surface growth with applications to additive manufacturing technologies. Procedia Engineering. 2017;**173**:11-16

[7] Saeidi K et al. Hardened austenite steel with columnar sub-grain structure formed by laser melting. Materials Science & Engineering. 2015;**A625**:221-229

[8] Hanzl P et al. The influence of processing parameters on the mechanical properties of SLM parts. Procedia Engineering. 2015;**100**:1405-1413

[9] Gu D et al. Processing conditions and microstructural features of porous 316L stainless steel components by DMLS. Applied Surface Science. 2008;**255**:1880-1887

[10] Yandroitsev I et al. Hierarchical design principles of selective laser melting for high quality metallic objects. Additive Manufacturing. 2015;**7**:45-56

[11] Riemer A et al. On the fatigue crack growth behavior in 316L stainless steel manufactured by selective laser melting. Engineering Fracture Mechanics. 2014;**120**:15-25

[12] Zhong Y et al. Intragranular cellular segregation network structure strengthening 316L stainless steel prepared by selective laser melting. Journal of Nuclear Materials. 2016;**470**: 170-178

[13] Saedi K et al. Transformation of austenite to duplex austenite-ferrite assembly in annealed stainless steel 316L consolidated by laser melting. Journal of Alloys and Compounds. 2015; **633**:463-469

[14] Liu Y et al. Investigation into spatter behavior during selective laser melting of AISI 316L stainless steel powder. Materials and Design. 2015;**87**:797-806

[15] Sadlaka J et al. Study of materials produced by powder metallurgy using classical and modern additive laser technology. Procedia Engineering. 2015;**100**:1232-1241

[16] Krakhmalev P et al. In situ heat treatment in selective laser melted martensitic AISI 420 stainless steels. Materials and Design. 2010;**87**:380-385

[17] Deev A et al. Anisotropy of mechanical properties and its correlation with the structure of the stainless steel 316L produced by the SLM method. Physics Procedia. 2016;**83**:789-796

[18] Zisman A et al. Quantity attestation of bainite-martensite structures of the high strength alloyed steels by the scanning electron microscopy methods. Metallurgist. 2014;**11**:91-95

[19] Hadayati R et al. Mechanical properties of additively manufactured octagonal honeycombs. Materials Science and Engineering. 2016;**89**:1307-1317

[20] Partovi A. Numerical and experimental study of crashworthiness parameters of honeycomb structures. Thin-Walled Structures. 2014;**78**:87-94

[21] Pirmohammad S et al. Crushing behavior of new designed multi-cell members subjected to axial and oblique quasi-static loads. Thin-Walled Structures. 2016;**108**:291-304

[22] Xiea S. Crashworthiness analysis of multi-cell square tubes under axial loads. International Journal of Mechanical Sciences. 2017;**121**:106-118

[23] Wirzbicki T. Crushing analysis of metal honeycombs. International Journal of Inpact Engineering. 1983;**1**(Part 2):157-174

[24] Niendorf T. Lattice structures manufactured by SLM: On the effect of geometrical dimensions on microstructure evolution during processing. Metallurgical and Materials Transactions B. 2014;**45**:1181-1185

*Edited by Igor V. Shishkovsky*

Freedoms in material choice based on combinatorial design, different directions of process optimization, and computational tools are a significant advantage of additive manufacturing technology. The combination of additive and information technologies enables rapid prototyping and rapid manufacturing models on the design stage, thereby significantly accelerating the design cycle in mechanical engineering. Modern and high-demand powder bed fusion and directed energy deposition methods allow obtaining functional complex shapes and functionally graded structures.

Until now, the experimental parametric analysis remains as the main method during AM optimization. Therefore, an additional goal of this book is to introduce readers to new modeling and material's optimization approaches in the rapidly changing world of additive manufacturing of high-performance metals and alloys.

Published in London, UK


IntechOpen

ISBN 978-1-83881-390-1